Nitrogen Doping of Sputtered Cuprous Oxide Thin Films by Ion Implantation

Martin Nyborg

Thesis submitted for the degree of
Master of Science in Materials Science and Nanotechnology
60 credits

Department of Physics
Faculty of mathematics and natural sciences

UNIVERSITY OF OSLO

Spring 2017

Nitrogen Doping of Sputtered Cuprous Oxide Thin Films by Ion Implantation

Martin Nyborg

Nitrogen Doping of Sputtered Cuprous Oxide Thin Films by Ion Implantation

http://www.duo.uio.no/

Printed: Reprosentralen

Abstract

Cu_2O is an intrinsic *p*-type metal oxide semiconductor with a direct band gap of $\sim$2.1 eV and a high absorption coefficient. Together with low cost, nontoxicity, natural abundance of copper and a theoretical conversion efficiency around 20% in a single junction structure, Cu_2O is a good candidate for next generation solar cells. Creating highly conductive *p*-type Cu_2O thin films is essential to realize its potential as a viable solar cell material. In this thesis, sputter deposition of Cu_2O thin films and the effect of nitrogen implantation is studied. The structural, optical and electrical properties of DC magnetron sputtered Cu_2O thin films, both undoped and doped with nitrogen, have been investigated. A nitrogen concentration of $\sim 10^{20}\, cm^{-3}$ was introduced by ion implantation at room temperature. Both the effect of post-deposition rapid thermal annealing (RTA)($900\,^{\circ}\mathrm{C}$ for 3 minutes) prior to implantation and a broad range of post-implantation annealing conditions ($200 - 600\,^{\circ}\mathrm{C}$ for 0.5h and $400\,^{\circ}\mathrm{C}$ for 0.5, 1, 2, and 4 hours) are reported. In all cases, the implanted films were compared to non-implanted ones with the same treatments to elucidate the effect of the implantation. The post-deposition RTA treatment increases the grain size and mobility in the samples, with an increase in mobility from $10 - 30 cm^2V^{-1}s^{-1}$ in the untreated samples to $\sim 50 cm^2V^{-1}s^{-1}$ after annealing. A reduced resistivity is achieved in the implanted samples compared to the undoped samples. In the samples which were RTA-treated prior to implantation and annealed at $400\,^{\circ}\mathrm{C}$ after, a carrier (hole) concentration of $10^{16} cm^{-3}$, resistivity of $29 \pm 1 \Omega cm$ and a mobility of $28 \pm 3 cm^2V^{-1}s^{-1}$ was achieved at room temperature, compared to the undoped ones; 3×10^{14}, $315 \pm 3 \Omega cm$ and $53 \pm 6 cm^2V^{-1}s^{-1}$, respectively. Further, in the implanted samples an acceptor level is introduced $\sim 170 meV$ above the valence band maximum which is not found in the undoped samples. This demonstrating that nitrogen is likely to be incorporated as a shallow acceptor dopant in Cu_2O thin films after implantation and successive annealing.

Acknowledgements

I would like to thank my day-to-day supervisor Kristin Bergum, for endless questions, proof reading, training and always keeping the door open for discussions. Secondly, my main supervisor Prof. Bengt Gunnar Svensson, thank you for introducing me to semiconductor physics and the LENS group during my bachelor. Your enthusiasm and dedication to the field and people around you is inspiring. Despite a busy schedule you were always available with good advice and open for discussion. Thank you Prof. Edouard Monakhov for co-supervision and many discussion throughout the year.

Thanks to the Ion Technology Centre (ICT), Royal Institute of Thechnology (KTH) and Uppsala University. Without the forthcomingness in the aid of ion implantation the realization of this thesis wouldn't be possible. I would also like to thank Dr. Alexander Azarov for SIMS measurements, Andreas Løken for SEM images and Heine Nygard Riise for help and training regarding Hall effect measurements.

A special thanks also to Viktor Bobal for always being available and coming to the rescue with anything related to the experimental work done at MiNaLab. To all my fellow students and employees at LENS, thank you all for making this year such an enjoyable and rich experience.

To my friends and family, I am very grateful for your continuous love and encouragement throughout this thesis. Finally, thank you Pernille T. Nyborg for your unending love, support and encouragement through all my years of studies.

Contents

1 | Introduction

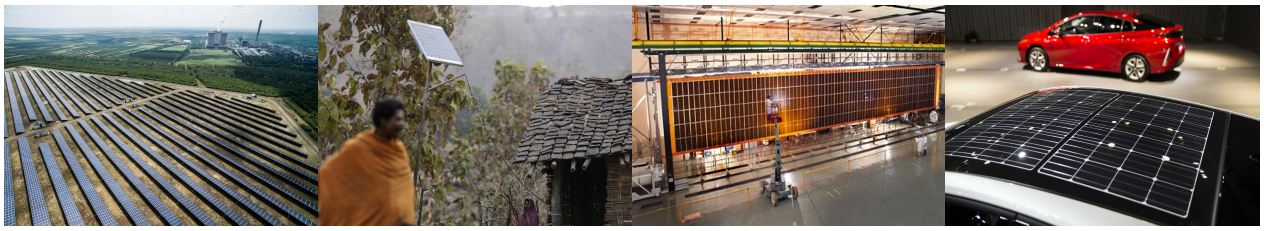

(a) **(b)** **(c)** **(d)**

Figure 1.1: a) Photovoltaic solar panels sit in an array at the 16-megawatt Visonta solar power station in Visonta, Hungary [1]. **b)** A village gets its power thorugh small-scale renewable sources in Maharashtra, India. [2]. **c)** A solar array blanket for the International Space Station (ISS) at Lockheed Martin Space Systems Company of Sunnyvale, California [3]. **d)** Solar panels on the roof of Toyota Motor Corp.'s new Prius plug-in hybrid at the National Museum of Emerging Science & Innovation in Tokyo [4].

Clean Energy Isn't Just the Future - It's the Present

Brian Eckhouse, Bloomberg

According to Bloombergs New Energy Finance (BNEF) renewable energy accounted for 55% of all new electrical capacity last year, where photovoltaics (PVs) makes up 68% of that. This means last year over 1/3 of all installed electrical capacity was solar. Solar energy is already the cheapest source of energy in some regions and BNEF predicts a further 36% price reduction by 2025 [5]. Today silicon based PVs accounts for over 90% of the total module production, however, the production of silicon PVs is capital intensive, requiring about 100 μm thick layers due to its low solar light absorption[6].

Thin film solar cells can with time become a more cost efficient alternative due to its low material demand (down to a few μm) and more energy efficient production [7]. Steinmann, Brandt and Buonassisi [6] say that the scale of PVs introduces new challenges and constraints on suitable materials for future of solar energy. The materials should have high efficiency, low material use, high reliability, be scalable and non-toxic. Todays leading thin film PV materials such as cadmium telluride (CdTe) and copper indium gallium selenide (CIGS) solar cells has achieved high efficiencies of 21.5% and 21.7% respectively, but their potential is diminished due to concerns of scarcity and toxicity of the materials involved. High efficiencies have also been achieved in pervoskite PVs

along with high defect tolerance and possibly low manufacturing costs, which has led to a lot of attention lately. However, pervoskite based PVs suffer from short life time due to degradation which must be resolved before commercialization [8]. Therefore, much effort is focused on finding other suitable candidate materials for PV applications.

One of the emerging materials with promising potential is Cuprous Oxide (Cu_2O), which is an abundant, low cost and non toxic semiconductor. Further, it is a direct band gap material with high absorption and a band gap of $\simeq 2.1$ [9]. Its band gap makes it a suitable partner with conventional Si solar cells in a tandem structure [10].

Considerable amount of work has been made to understand and control the physical properties of Cu_2O. In the past few years this has yielded significant results with a jump in conversion efficiency from $\sim 2\%$ to over 8 % in a Cu_2O/ZnO heterojunction structure [6, 11]. However, the high efficiencies have been achieved in thick oxidized copper sheets. It would be favorable to reach higher efficiencies also in thin film Cu_2O based solar cells which could be incorporated in tandem structures, by thin film technologies like sputtering and electrodeposition [12]. Unfortunately, low carrier mobilities seems to be a challenge in thin film Cu_2O compared to the oxidized sheets. Cuprous oxide show spontanious p-type conductivity, however by thin film deposition methods the carrier concentration varies, tends to be low and is hard to control. Doping is a possible route to achieve higher carrier concentrations and a reduced resistivity, which is desirable for emitter and contact layers in a solar cell.

Nitrogen doping of Cu_2O has received growing attention. Reports show reduced resistivity and preserved optical qualities in doped Cu_2O thin films [13, 14]. Nitrogen is expected to substitute for oxygen with a high solubility due to their similar ionic radii [15]. Additionally, low-resistivity ohmic contacts can be achieved by highly N doped Cu_2O regions effectively forming tunneling junction back contacts [13]. Altogether, making it a promising candidate for p and p^+ doping of Cu_2O.

2 | Theory

2.1 Crystalline Materials

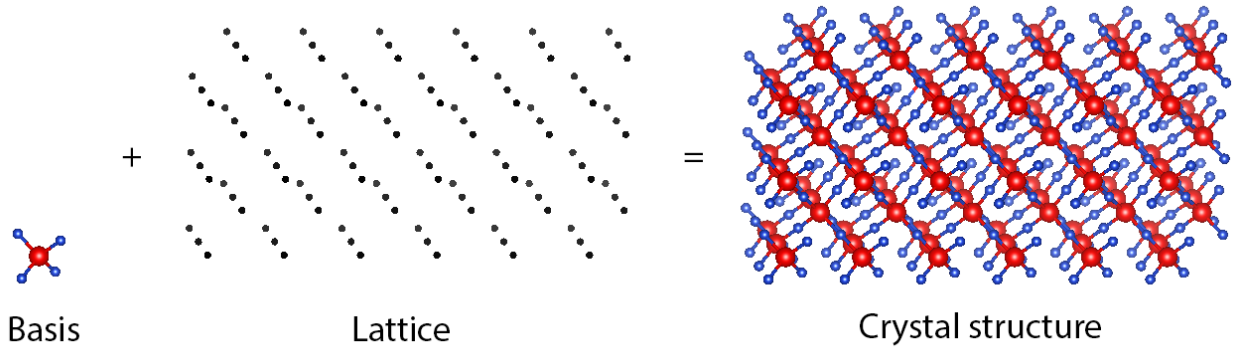

Figure 2.1: When the basis occupies all points in the mathematical lattice the final structure forms. Exemplified by the Cu_2O crystal structure.

This section is based on the books by Kittel [16], Streetman [17] and Tilley [18].

In a solid, atoms and molecules are bound together by strong bonds, such as covalent-, ionic- or metallic bonds. If the arrangement of atoms in a solid is periodic, it is said to have a crystal structure. Solids can be made up of one single crystal (crystalline solids), by many small crystallites grouped together (polycrystalline solids) or have no periodicity at all (amorphous solids). Crystallography describes the way atoms are arranged in solids and is an essential tool to understand and predict materials properties.

An ideal crystal is constructed by repeating an identical atom or group of atoms known as the basis in a periodic fashion at points which are geometrically identical throughout the crystal, called the lattice. Combining the basis and lattice make up the final crystal structure, as illustrated in Figure 2.1. The lattice is a mathematical concept, if any lattice point is taken as the origin, all other lattice point at position **P** can be found from:

$$\mathbf{P}_{uvw} = u\mathbf{a} + v\mathbf{b} + w\mathbf{c} \tag{2.1}$$

where **a**, **b** and **c** are the basis vectors, and u, v and w integers. The smallest unit to describe the total crystal geometry spanned by this parallelepiped is called the primitive unit cell. In many cases,

the crystal structure is easier visualized by larger unit cell than the primitive unit cell, but keeping the underlying symmetry.

All 3-dimensional lattices are represented by seven different unit cell types which depends on the angles and length ratio between the basis vectors. From these seven, by adding additional points on the faces (face centered) or to the center (body-centered), it can be made a total of 14 different lattices, called the Bravais lattices. By placing a basis on the lattice points in one of the Bravais lattices all crystal structures can be created.

Crystal planes are planes in the crystal which have the same geometrical arrangement throughout the crystal structure. The notation used for specific planes are called Miller indices labeled (hkl), where h,k and l are a set of integers found from where the plane intercept the axes in term of the lattice constants a, b and c. By taking the reciprocal of those numbers and reducing it to the smallest three integers h, k and l having the same ratio we get the Miller indices as (hkl).

The crystallographic data are fundamental to understand the mechanical, optical and electrical nature of crystalline materials.

2.2 Crystal Defects

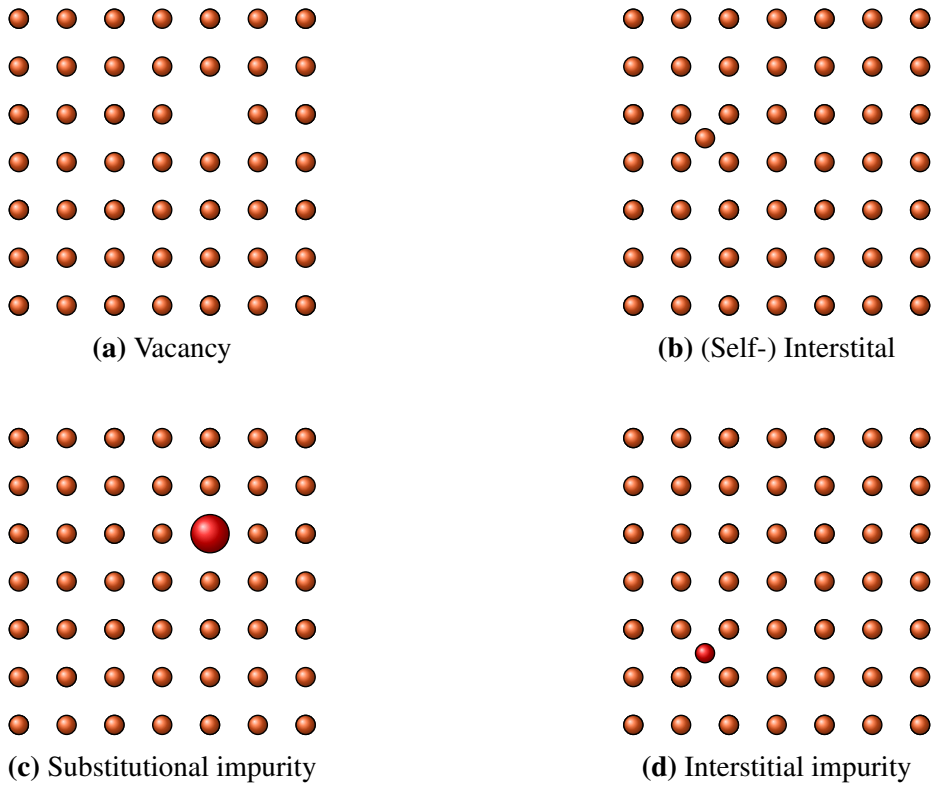

(a) Vacancy

(b) (Self-) Interstital

(c) Substitutional impurity

(d) Interstitial impurity

Figure 2.2: Illustrations of various defects

This section is based on the works by Tilley [18], Norby [19] and Campbell [20].

Many if not all who work with semiconductors need to pay close attention to defects and impurities in their materials to get optimal performance. There are four main types of impurities and imperfections; point defects, line defects, plane defects and volume defects, which extend in 0, 1, 2 and 3 dimensions, respectively. Each type is important and may affect different areas of fabrication or properties of the materials. Defects and impurities are in many cases unwanted but they can also be tailored so that they work to our advantage. The defects considered here are point defects which are associated with a single point in the lattice.

2.2.1 Intrinsic defects

There are two types of defects in a pure crystal, one where atoms can be absent from a normally occupied position, or an atom can take up a position in the crystal which is usually empty. These type defects are known as vacancies and self-interstitials, respectively (Figure 2.2a and 2.2b). Vacancies and self-interstitials are present in an otherwise perfect and stoichiometric crystal due to thermodynamic considerations. These kind of defects are also called intrinsic defects. For example in $NaCl$ a Na vacancy, $v_{Na}^{/}$, is accompanied by a Cl vacancy, $v_{Cl}^{\bullet}$, thus maintaining stochiometry and charge neutrality. This kind of paired vacancy is called a Schottky defect. Alternatively, the vacancy is balanced by an interstitial of the same species, i.e., $v_{Na}^{/}$ compensated by $Na_i^{\bullet}$ at an interstitial site, this is known as a Frenkel defect.

2.2.2 Nonstoichiometry

In most compounds, the charges are to some degree related to the species, especially so in ionic compounds. In non-stoichiometric compounds, there are either deficit or excess of one constituent. If the associated defects are charged, electronic defects follow to preserve electrical neutrality. E.g., in Cu_2O, oxygen has an effective charge of -2 and each Cu atom has +1, therefore when removing a copper atom the resulting copper vacancy $V_{Cu}^{/}$ has an effective charge of -1. This can be balanced by i.e a hole through [21]:

$$1/4O_2(g) = 1/2O_O^0 + V_{Cu}^{/} + h^{\bullet} \tag{2.2}$$

2.2.3 Extrinsic defects

No material is completely pure, there will always be some extrinsic point defects, foreign atoms present in the material as impurities. A substitutional impurity defect occupies a crystal site normally occupied by the host atom (Figure 2.2c). It may also occupy interstitial sites as interstitial impurities (Figure 2.2d). Foreign atoms in semiconductors may act as dopants. If an impurity has a valence different than the host atom it can effectively contribute to the carrier density in the material. Doping is a common way of altering the materials properties and especially in semiconductors to control electrical properties, such as carrier type and concentration.

2.3 Electronic Characteristics

This section is based on the works by Kittel [16], Streetman [17] and Nelson [22].

The electric conductivity of semiconductors is between those of metals and insulators. Additionally, the conductivity of semiconductors can be altered over many orders of magnitude due to changes in temperature, optical excitations or impurity defects. This enables intriguing properties and possible applications like solar cells, sensors, and transistors to mention some. To understand the source of these properties, we must understand the allowed energy levels for electrons in crystals.

2.3.1 Energy Bands

When atoms are brought together the atomic orbitals combine to form molecular orbitals. The combination results in pairs of molecular orbitals with an antibonding orbital with higher energy and a bonding orbital with lower energy compared to the initial energy levels. When many atoms are combined, the levels are split into many levels such that they can be considered a continuum, a band. These bands can be separated by forbidden intervals, called the band gaps (E_g), where there are no allowed energy levels. The highest occupied energy band is called the valence band (VB), and the first unoccupied band is called the conduction band (CB). The occupation of the bands is important and available states near the highest occupied energy level determine if the material is a metal, semiconductor or an insulator.

To determine the energy levels of electrons in atoms isolated or molecules, we must solve the Schrödinger equation. In solids, we need to do the same, but now one must account for the potential of all neighboring atoms. Due to the crystalline structure of most metals and semiconductors, we can take advantage of the symmetry of the lattice and impose this order on the wave functions assuming a perfect lattice. The Bloch theorem states that the wave function of an electron in a periodic environment may be expressed as

$$\Psi_{\mathbf{K}}(\mathbf{r}) = u_{\mathbf{k}}(\mathbf{r})exp(i\mathbf{k}\cdot\mathbf{r}) \tag{2.3}$$

where $u_{i\mathbf{k}}(\mathbf{r})$ is a periodic part related to the periodicity of the lattice with the condition that $u_{i\mathbf{k}}(\mathbf{r}) = \mathbf{u_{ik}}(\mathbf{r}+\mathbf{T})$, where T is the translation vector of the lattice. $\mathbf{k}$ is the wavevector and $e^{i\mathbf{kr}}$ is a plane wave. Solving the Schrödinger equation for these conditions gives solutions for its eigenenergies $E_n(\mathbf{k})$, where n is the band index (n = 1,2,3,...). There exists discrete E_n that vary for a given $\mathbf{k}$. Mapping energies E_n versus the wave vector $\mathbf{k}$ results in a band diagram as the one illustrated in figure 2.3 which describes the available energy states which electrons can occupy.

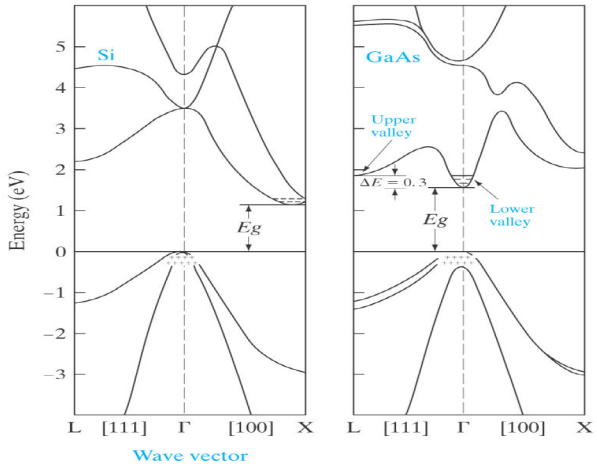

Figure 2.3: (E,k) relationship in Si and GaAs showing the conduction and valence bands along the [111] and [100] crystal directions. Where the first figure illustrates an indirect band gap and the second one a direct band gap. From Streetman [17]

When considering a crystal made up of exactly N primitive unit cells each unit cell contribute one independent value of k to each energy band. When taking spin into account this results in 2N independent states for electrons in each energy band. If there is one valence electron per atom per unit cell, the valence band is half filled. If there are two valence electron per atom per cell or two atoms with a valence electron per unit cell, the valence band will be filled. If the valence band is partially filled or overlaps in energy with the conduction band, there are many available states with similar energies making it easy for electrons to scatter and be transported. This is the case in metals resulting in a high conduction of current and heat (2.4). In semiconductors the valence band is full and separated from the conduction band by E_g. Electrons must overcome E_g to contribute to the conduction through optical or thermal excitation. The difference between insulators and semiconductors is the magnitude of the band gap, typically semiconductors are attributed to materials with a E_g in the range 0.5 to 4 eV. Above that, it is usually considered as an insulator since hardly any carrier are excited across E_g at room temperature.

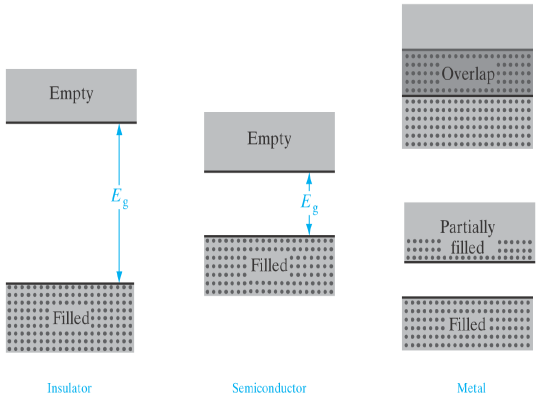

Figure 2.4: Typical band structure for insulator, semiconductor and metal at 0K. In an insulator the band gap separates the available states to such a degree that negligible carriers exist in the conduction band. In semiconductors the band gap is small and charge carriers can be generated through optical and thermal excitation. For metals there are many overlapping states and charge carriers can easily flow. Adapted from Streetman [17]

If the minimum and maximum band energies occurs at the same value of $\mathbf{k}$ the material is considered a direct band gap material, illustrated in Figure 2.5 a). On the other hand if the minimum and maximum occur at different $\mathbf{k}$, a momentum change $\Delta\mathbf{p} = \hbar(\mathbf{k_1} - \mathbf{k_2})$ is required for an excitation to take place. In optical excitations, since the photons have very little momentum, the change in momentum must be provided from elsewhere. Usually it is provided from phonons (lattice vibrations) with the right wave vector. Semiconductors with this excitation route are called indirect band gap material (Figure 2.5 b)) . Excitations are less likely to occur in indirect band gap materials resulting in lower absorption coefficients. Silicon is an indirect material and requires a thick absorption layer in solar cells, typically a few hundred microns thick in contrast to direct band gap solar cell where a few microns usually is sufficient.

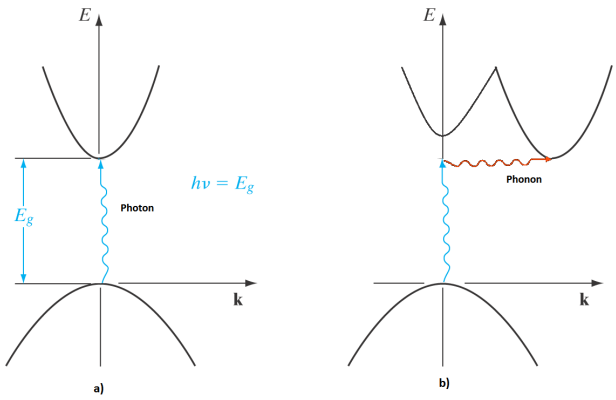

Figure 2.5: Direct and indirect electron excitations in smeiconductors. a) Direct bandgap. b) Indirect bandgap. Adapted from Streetman [17]

Excited electrons can be described similarly to free electrons, but interaction with the periodic potential of the lattice must be considered. Their wave-particle motion is approximated by the energy-wavevector relation of a free electron $\epsilon = \frac{\hbar^2}{2m}k^2$, but by altering the mass we can account for most of the influence from the lattice. This new mass is termed effective mass and is found by accounting for the curvature of the energy bands in three dimensions. Effective mass of an electron or hole with a given energy-wavevector relation can be found in a band as

$$m^*_{n,h} = \frac{\hbar^2}{d^2E/d\mathbf{k}^2} \tag{2.4}$$

2.3.2 Charge Carriers

In metals, there is an electron "sea" indicating a population of relatively free electrons which can easily flow in the material. For a perfect and un-doped semiconductor crystal at 0 K, the VB is filled, and no carriers are present in the CB. A qualitative way to illustrate this is the breaking of covalent bonds in the crystal, at 0K all electrons are participating in bonding. When the temperature increases electrons will overcome the band gap due to the thermal energy kT and be excited into the CB. Thereby, they break free from the bound state and effectively contribute to the current. When an electron is excited, it leaves behind an empty site in the otherwise full valence band. This hole, as it is called, behaves just like an electron except as if it had a positive charge. When a valence electron moves into the available empty state (hole), the hole "moves" in the opposite direction effectively contributing to the net current. If an electron and hole are created by the excitation of a valence band electron leaving behind a hole they are called an electron-hole pair (EHP). In intrinsic semiconductors all charge carriers present are EHP's, the concentration of holes p (holes per cm^3) equals the concentration of electrons n (electrons per cm^3) and thus equals the intrinsic carrier concentration n_i

$$n_i = n = p \tag{2.5}$$

Certain impurities and defects will drastically influence the electrical properties of a semiconductor, especially doping the material with either donors or acceptors. Donors are atoms with more valence electrons than the host atoms and thus can donate an electron to the CB. Acceptors have less valance electrons and accept electrons from the VB, resulting in holes. When impurities or defects are present in a semiconductor crystal additional levels are created in the band structure, also within the band gap. For donors, these levels preferably occur close to the CB, and thus little energy is necessary to excite an electron into the CB. Similarly, for acceptors the energy level occurs close to the VB, requiring little energy for a valence electron to be excited up to the acceptor level, leaving behind a hole in the VB. The number of dopants is often large compared to the intrinsic carrier concentration at room temperature. When the dopant is a donor in excess of the intrinsic concentration it is termed *n*-type doping, if the dopant is an acceptor it is called *p*-type doping.

2.3.3 Carrier concentrations

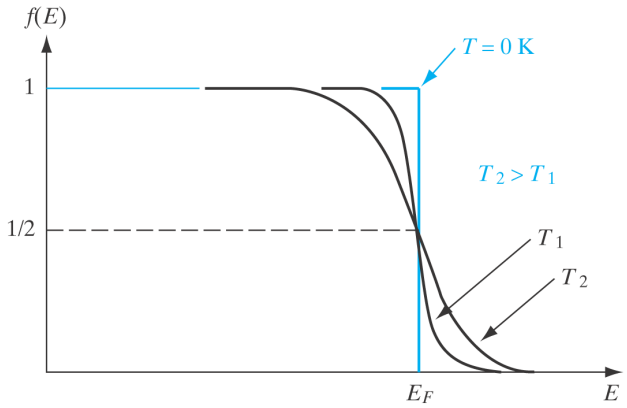

Figure 2.6: The Fermi-Dirac distribution function for T = 0 and $T < T_1 < T_2$. From Streetman [17]

To determine the energy distribution of electrons one must consider their indistinguishability, wave nature and the Pauli exclusion principle. The resulting probability distribution is known as the Fermi-Dirac distribution function

$$f(E) = \frac{1}{1 + e^{E - E_F/kT}} \tag{2.6}$$

where E is the energy, k is Boltzmann constant, T is the absolute temperature, and E_F is the Fermi energy or the Fermi level. The Fermi level is the energy at which occupation probability is 50%. The function f(E) gives the probability that an energy state at E will be occupied at a given temperature T. At 0 K the function is step-like where there is zero probability of occupancy above E_F and one for states below E_F. When the temperature increases there is increasing probability that states above the E_F are filled (figure 2.6). Correspondingly the probability for an empty state below E_F is found from [1-f(E)]. In the case of semiconductors, this is the probability that an electron is occupying a state in the conduction band or [1-f(E)] a hole in the valence band. In an intrinsic semiconductor, the Fermi level lies in the middle of the band gap while for *n*-type semiconductors it shifts towards the conduction band and for *p*-type towards the valence band (figure 2.7).

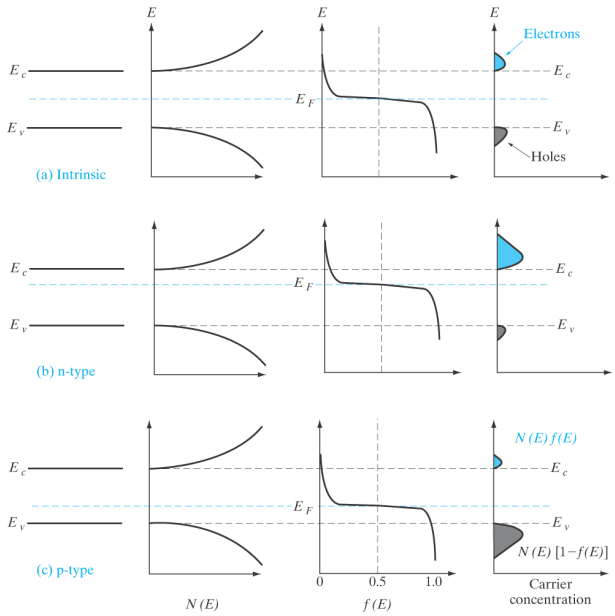

Figure 2.7: Illustrated band diagram, density of states, Fermi-Dirac distribution and the carrier consentrations for a) intrinsic , b) *n*-type and c) *p*-type semiconductors, at thermal equilibrium. From Streetman [17]

By combining the Fermi-Dirac distribution with the available density of states N(E) in the material one can calculate the concentration of electrons and holes (commonly in cm^-3). For electrons in the conduction band it is found by integrating over all available energies,

$$n = \int_{E_c}^{\infty} f(E)N(E)dE \tag{2.7}$$

and for holes in the valence band

$$p = \int_{-\infty}^{E_v} (1 - f(E))N(E)dE \tag{2.8}$$

where E_c is the conduction band edge, E_v the valence band edge and N(E)dE is the density of states (cm^-3) in the energy range dE. The Fermi-Dirac distribution decreases rapidly for large energies; hence, very few electrons occupy states far from the conduction band edge. The result of eq. 2.7 is the same if the density of states is expressed by an effective density of states N_c with all states located at the conduction band edge E_c.

$$N_c = 2\left(\frac{2\pi m_n^* kT}{h^2}\right)^{3/2} \tag{2.9}$$

where m_n^* is the effective mass of electrons at the conduction band edge, k Boltzmann's constant, and h is Planck's constant. The same is true for the effective density of states in the valence band N_v only with the factor m_p^* in stead of m_n^*.

If the Fermi level lies at least several kT away from the band edges, f(E) can be simplified as

$$f(E_c) = \frac{1}{1 + e^{(E_c - E_F)/kT}} \simeq e^{-(E_c - E_F)/kT} \tag{2.10}$$

which further simplifies the electron and hole concentrations to

$$n = N_c f(E_c) = N_c e^{-(E_c - E_F)/kT} \tag{2.11}$$

$$p = N_v(1 - f(E_v)) = N_v e^{-(E_F - E_v)/kT} \tag{2.12}$$

In an intrinsic semiconductor the hole density equals the electron density as in eq. 2.5, now by combining this with equation 2.11 and 2.12 we get that

$$np = n_i^2 = N_c N_v e^{-(E_c - E_v)/kT} = N_c N_v e^{-E_g/kT} \tag{2.13}$$

The product of n and p is constant for a given temperature T in a material (with a given band gap and density of states). It is also valid for doped materials since it is independent of the Fermi level position. At room temperature the intrinsic carrier concentration in silicon is about $n_i = 1.5x10^{10} cm^{-3}$, while in doped semiconductors, the carrier concentrations can be as high as 10^{20}.

In highly doped *p*-type semiconductors the hole concentration can be simplified as

$$N_a^- \simeq p \tag{2.14}$$

where N_a^- is the number of ionized acceptor atoms, in other words the number of holes created by acceptor atoms and N_a is the number of doping atoms per volume. By combining equation 2.13 and 2.14 we find the electron concentration in highly doped materials as

$$n = \frac{n_i^2}{N_a^-} \tag{2.15}$$

similarly the relations also applies to *n*-type semiconductors with a donor doping concentration N_d,

$$N_d^+ \simeq n \tag{2.16}$$

$$p = \frac{n_i^2}{N_d^+} \tag{2.17}$$

where N_d^+ is the number of ionized donor atoms and N_d is the number of donor atoms per volume. If all donor or acceptors are ionized $N_d^+ = N_d$ and $N_a^- = N_a$.

2.3.4 Compensation

Since the product of the electron and hole concentrations is a constant at a given temperature, one must decrease one if the other is increased. In the above case we assumed an excess of one type of carrier, e.g. $N_a^- >> N_d^+$, such that $p \simeq N_a^-$. However, one can have both donors and acceptors in the material effectively reducing the other, in this case the hole concentration $p = N_a^- - N_d^+$. This kind of charge carrier reduction is called compensation. This way it is possible to invert a *p*-type semiconductor into a *n*-type semiconductor by introducing a sufficient amount of donors.

By adding donors you can get to the point where $N_d = N_a$ and all acceptor states are compensated, filled by the donor electrons, so that the material regains its intrinsic character, $n_i = n = p$. By further donor doping the material becomes n-type with an electron concentration of $N_d^+ - N_a^-$.

The relationship between electron, hole, donor and acceptor concentrations can be obtained by considering the requirement for space charge neutrality:

$$p + N_d^+ = n + N_a^- \tag{2.18}$$

2.3.5 Temperature effects on carrier concentrations

In semiconductors the creation of mobile electrons and holes is a dynamic process. There are continuously electrons excited into the conduction band and falling back down into the valence band recombining with holes. At elevated temperature this activity is increased. Combining eq 2.13 and 2.9 we get an intrinsic carrier concentration temperature dependency as

$$n_i(T) = \left(\frac{2\pi kT}{h^2}\right)^{3/2} (m_n^* m_p^*)^{3/4} e^{-E_g/kT} \tag{2.19}$$

The temperature dependency is dominated by the exponential term. When plotting $ln(\frac{n_i}{T^{3/2}})$ vs. $1000/T$ we get a linear relation with the slope as $-E_g/kT$.

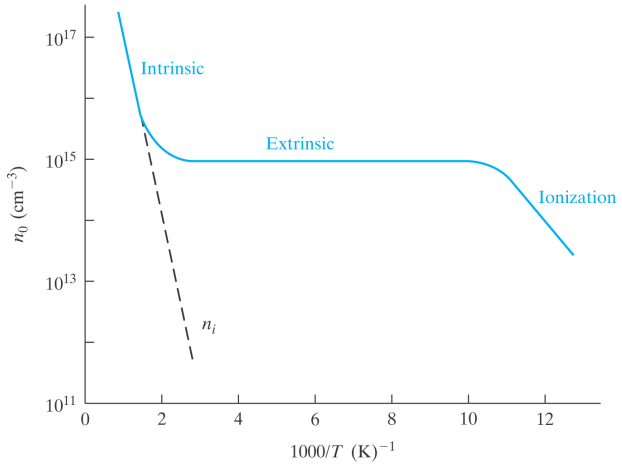

Figure 2.8: Log scale carrier concentration vs. inverse temperature for doped Si with a donor concentration of $10^{15} cm^{-3}$. From Streetman [17]

In extrinsic semiconductors the dopants introduce shallow donor or acceptor states in E_g which are easily ionized and contribute to the carrier concentration. In the case of a *n*-type material at very low temperatures carriers are "frozen out". The thermal energy is less than the ionization energies of the donor levels and the carrier concentration is low. In figure 2.8 we see that we get an ionization region where slope is proportional to the ionization energy of the donors. At intermediate temperatures where all donor atoms are ionized we get the extrinsic region with concentrations $\sim N_d$. At elevated temperature the intrinsic carrier concentration eventually surpasses the dopant concentration in the intrinsic region (Figure 2.8).

In similar fashion as the intrinsic carrier concentration versus temperature can be used to find the band gap, one can estimate the extrinsic carrier activation energy in the ionization regime by a semi-log of the carrier concentration versus the inverse temperature.

2.3.6 Carrier transport

In semiconductors the conductivity is expressed through the contribution of both holes and electrons:

$$\sigma = (ne\mu_e + pe\mu_p) \tag{2.20}$$

n and p are the electron and hole concentrations and μ_h and μ_e the hole and electron mobility. The mobility describes how easily the electrons and holes drift in the material, where:

$$\mu_{h,e} \equiv \frac{q\bar{t}}{m^*_{h,e}} \tag{2.21}$$

with $\bar{t}$ as the mean time between scattering events. There are two basic mechanisms that influence the hole and electron mobility, impurity scattering and lattice scattering. Impurity scattering is due to impurities in the crystal, such as charged impurities and grain boundaries. Large impurity concentrations or small grains give low mobility due to more scattering events taking place. At higher temperatures the thermal velocity of the carriers is higher and therefore the interaction time with the impurities reduces the scattering impact. On the other hand, lattice scattering due to phonon vibration of the lattice increases at higher temperatures. Thereby, at lower temperatures the mobility is dominated by impurity scattering while at higher temperature the lattice scattering is the dominating effect. The temperature dependencies on mobility due to the two mechanisms can be approximated as $T^{3/2}$ for impurity scattering and $T^{-3/2}$ for lattice scattering.

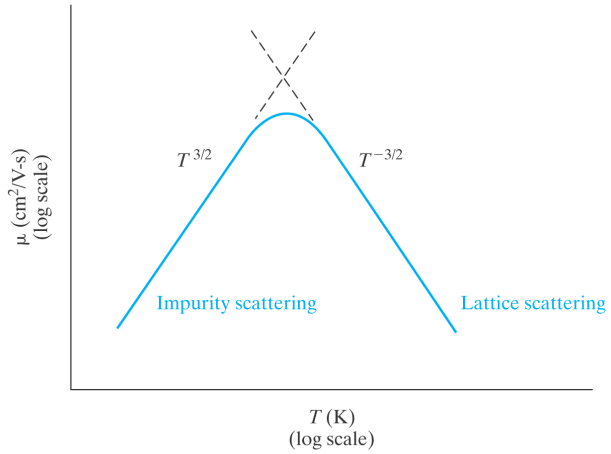

Figure 2.9: Temperature dependency of mobility with impurity and lattice scattering. From Streetman [17]

2.4 Solar Cells

This section is based on the study by Nelson [22].

A solar cell is a device which generates electricity from light. The photovoltaic effect was first documented by Edmund Becquerel in 1839, as he observed that illuminating an electrochemical cell generated voltage between the electrodes. The first solid-state system demonstrating the photovoltaic effect was discovered 40 years later by William Adams and Richard Day in 1876. They found that a photocurrent was generated spontaneously when Selenium was illuminated by light. Later Charles Fritts made the first large area solar cell by pressing a layer of selenium between gold and another metal. In the next fifty years there were little progress in terms of efficiency, and conversion efficiencies above 1% eluded the scientist. The breakthrough came with the discovery of Silicon quality processing in the 1950s allowing p-n homojunctions which showed much better rectifying action than the Schottky barriers which had been used previously.

The most common solar cell today is still the silicon p-n homojunction in monocrystalline, multi (poly)crystalline and thin film amourphous silicon. Today these cells show module efficiencies of about 24%, 20% and 11 % respectively, approaching the theoretical maximum efficiency of about 29.1 %. In fact, the lab record was recently broken with a photoconversion efficiency of 26 % [23]. Other major technologies are CdTe and CIGS, which both are heterojunction thinfilm solar cells with module efficiencies of about 19% and 18 % respectively [24].

The solar cell operates through three fundamental mechanics. Firstly, the material must absorb the light and generate EHP's, secondly, the excited carriers must be separated and finally they must be extracted to an external circuit. From this we have some material requirements in order to achieve high efficiencies. The material should have high absorbance for photon energies above the band gap. The reflectivity of the surface R(E) should be low for relevant photon energies. This is usually further enhanced by employing an antireflective coating on top of the solar cell . Further, there must be some built in asymmetry which separates excited EHP's before they recombine, this can be an electric field or a gradient in electron density. As stated earlier, this asymmetry is achieved by a p-n junction effectively creating an electric field which drives the electron and holes in opposite directions, towards n and p side of the cell respectively. There, they are finally collected at the contacts by diffusion. Therefore, the material must be a good electronic conductor such that optimally no carriers recombine with defects or impurities before collection at the contacts. There should be no resistive loss at the contacts (low series resistance), i.e good Ohmic contacts and no current leakage (high shunt resistance). A common way to achieve low contact resistance is through heavy doping near the contact, which creates tunneling contacts with Ohmic characteristics. Another effect of this doping is a back surface field, the gradient in carrier concentration towards the back contacts creates an electric field driving the carriers towards the contacts.

2.4.1 Tandem solar cells

The absorption of light in semiconductors depend on the E_g of the material. When light is incident on a solar cell one out of three things can take place.

First some fraction of the light, R, will be reflected off the surface. Secondly, light with energies below E_g passes through the semiconductor, in both these cases the light will not contribute to pho-

togeneration. Finally, light with energies above E_g is absorbed and excite EHP's. Thus, effectively contribute to the photocurrent, however the excess energy above E_g is lost due to thermalization. Thermal relaxation down to the CB band edge happens on the timescale of nanoseconds and thus the energy is lost before extraction at the contacts. Hence, much of the light incident on the solar cell won't contribute to the total current, but is lost to heat, transmission and reflection.

A way to use more of the energy provided in the solar spectrum is to stack multiple p-n junctions with different band gaps in order to absorb a different energy part of the light at different junctions. The stacks must be designed such that the largest band gap is on top. This way the radiation with high energy will be absorbed here giving up most of its energy, reducing thermalization losses. Further the light with less energy passes through to the next junction and is extracted there. These kind of stacks are called tandem solar cells. Theoretically an infinite stack is calculated to have a maximum of 68 % conversion efficiency [25]. A two layered stack with optimal band gap values has a theoretical maximum of 42%, a substantial improvement compared to 30% of a single junction solar cell [25].

2.5 Cuprous Oxide

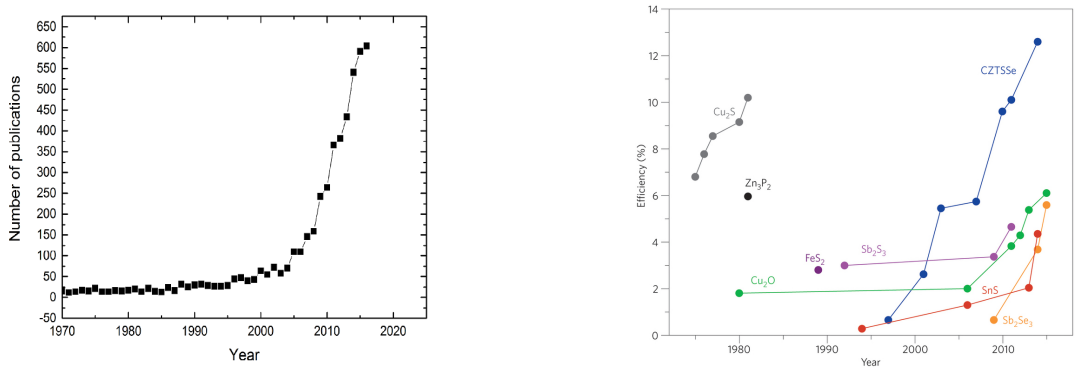

(a) **(b)**

Figure 2.10: a) Evolution of number of publications containing the search word "Cu_2O" and/or Cuprous Oxide in the title [26]. **b)** Efficiency improvements over time for various eart-abundant thin-film photovoltaic technologies, with Cu_2O in green [6].

This section and subsections are based on the works by Biccari [21] and Meyer [27].

Cuprous oxide (Cu_2O) is one of three stable copper oxides together with Cupric oxide (CuO) and Paramelaconite (Cu_4O_3). Historically, Cu_2O was one of the first materials recognized as a semiconductor beside selenium. As early as 1924 rectifiers were used industrially, and much of the early theory on rectifiers and semiconductor was based on these early Cu_2O devices [28]. A problem with the research during this period was the quality of the materials recognized as semiconductors, they were compounds with poor control of impurities and stoichiometry. Semiconductor research therefore remained more like art than science at the time [29]. When doping and high quality processing of silicon (99.999 percent pure) and germanium were discovered in the 1950s, they took over as the leading semiconductor materials.

The first solar cell based on Cu_2O was made in the late 1920s, however, before the rise of space travel and focus on photovoltaic (PV) energy production, solar cells were just a curiosity and the interest diminished. In the 1970s as a possible energy solution following the oil crisis, interest in Cu_2O was rejuvenated as a candidate material for low cost solar cell production. The focus then was on Schottky junction PV devices, however efficiencies never exceeded 1%. Reduction of the Cu_2O surface to Cu made all the cells essentially a $Cu/Cu2O$ junction, regardless of which contact metal that was used [30].

Another area of interest regarding Cu_2O is studies on fundamental physical phenomena. Besides CdS it was the first substrate in which excitons were observed. Nowadays fundamental studies are done in the search of the Bose-Einstein condensation of excitons. It is also an important material in studies of polaritrons and phonoritons.

Recently the interest in Cu_2O has again increased and the conversion efficiency has started to rise (Figure 2.10a and 2.10b). Additionally, it is fueled by the success of similar materials systems [6] and by new approaches to achieve high efficiency in solar cells, such as the Intermediate Band (IB) and multi-junction (Tandem) solar cells. IB solar cells are made of absorber layers with a

continuum of states in the band gap allowing multiple excitations routes facilitating for an increased photo-currents.

2.5.1 Materials Properties

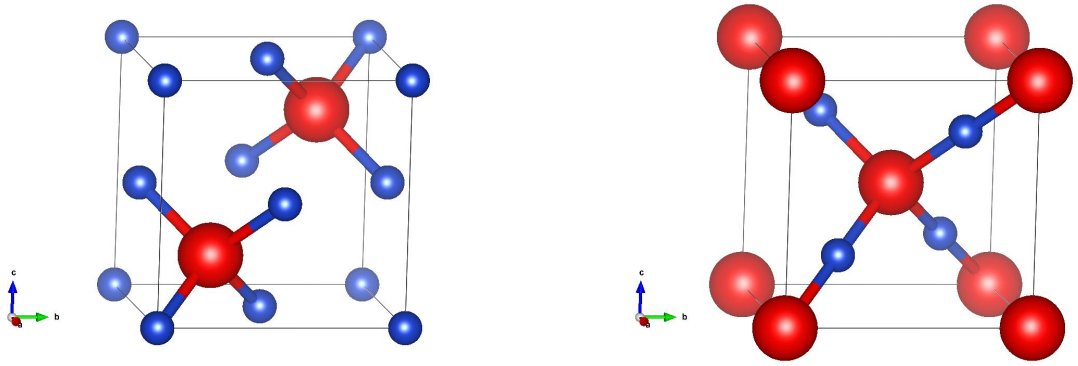

(a) Origin on a copper site.

(b) Origin on a oxygen site

Figure 2.11: Illustration of the cuprite structure unit cell. These structures contains two Cu_2O formula per unit cell. Oxygen atoms are illustrated by red spheres and copper by blue. The illustration was made using VESTA software [31].

Cu_2O crystallizes in the cuprite structure, a simple cubic Bravais lattice with the symmetry of space group 224 (Pn-3m). As shown in Figure 2.11 its unit cell contain six atoms; four copper atoms in an fcc lattice (blue spheres) and two oxygen atoms in tetrahedral sites forming a bcc sub lattice (red spheres) shifted a(1/4, 1/4, 1/4) relative to the fcc lattice. This way it can be represented in two ways, with either an Oxygen or Copper atom in origo. The lattice constant is measured to be a = 4.2696 Å [32]. Lattice constant and crystal structure have been measured by X-ray diffraction (XRD) and are reported in table 2.1.

Table 2.1: XRD pattern for Cu_2O at room temperature under atmospheric pressure as reported in International Centre for Diffraction Data (ICDD) pattern: 01-071-3645.

2θ	Int	h	k	l
29.579	9	1	1	0
36.450	100	1	1	1
42.334	37	2	0	0
52.501	1	2	1	1
61.400	27	2	2	0
69.635	1	3	1	0
73.597	17	3	1	1
77.400	4	2	2	2
92.480	2	4	0	0
103.882	4	3	3	1
107.688	3	4	2	0
124.402	3	4	2	2
139.541	3	5	1	1

Cu_2O has a direct band gap of about 2.1 eV at room temperature. It shows "naturally" *p*-type conductivity and has proven difficult (if not impossible) to dope *n*-type. Many of Cu_2O's properties are determined by the small deviations from stoichiometry that can arise in this material. However, the full picture of these relations is still somewhat unclear.

There is a delicate balance between defects in Cu_2O, which to a large extent is ruled by the dependence on temperature and oxygen partial pressure. Some of the intrinsic defects in Cu_2O are vacancies (V_{Cu} and V_O), interstitials (O_i and Cu_i), Frenkel defects (V_{Cu} + Cu_i and $V_O + O_i$) and Schottky defects ($2V_{Cu}+V_O$). In addition, there is possible deficiency or excess of either constituent and the incorporation of impurities. Hence, the properties obtained in cuprous oxide requires close control of fabrication parameters and is strongly dependent on the method of synthesis.

The p-type conductivities nature is fortunately more clear, it is believed to originate from cation deficiency, copper vacancies(V_{Cu}) as it was predicted by Brattain in 1951 [33]:

> *Copper oxide is a defect semiconductor. The carriers are missing electrons, or holes, in the filled band. The main impurity centers, acceptors in this case, are probably vacant copper ion lattice sites.*
>
> Walter H. Brattain

This has been further confirmed through high temperature experiments and theoretical ab-initio calculations. Additionally, Cu_2O is likely to be a compensated material where the ratio of N_D/N_A is only slightly under 1 in most cases.

2.5.2 Doping

n-type doping would provide the possibility of homo-junctions which is preferred to avoid band offsets, lattice mismatch and limit the formation of interface defects. However, in Cu_2O the formation energy of copper vacancies approaches zero when the Fermi level is in the upper half of the

band gap, hence copper vacancies form readily, effectively acting as a self-compensating defect for *n*-type conductivity. This is a general accepted interpretation of why *n*-type doping is for now deemed impossible.

Among possible extrinsic acceptors there are many candidates, sodium [34], magnesium, silicon and chlorine to mention some, additionally many transition metals have been tried as dopants with varying success. Finally, promising results are shown for nitrogen doping, where nitrogen act as a substitutional acceptor replacing oxygen. More on the effect of nitrogen doping can be found in section 2.6.

Unless the bands of a semiconductor-metal junction coincide, a barrier for the carriers is present. For Cu_2O metals with a larger work function than 5 eV is required to avoid this barrier. Few metals exhibit this and those who do (i.e gold and platinium) are scarce and expencive. A way around this problem is extensive doping which will result in a drastically reduced space charge region and lead to what is known as a tunnel junction, allowing low resistive Ohmic-like contacts.

2.5.3 Cu_2O as Solar Cell Material

Cu_2O meets all the requirements proposed by Steinmann, Brandt and Buonassisi [6] as a candidate material to face the design criteria for the next generation solar cells. Low manufacturing cost, low material use (high absorbance), reliability (good cell stability), it must be scalable (abundant materials) and non-toxicity. Finally, high conversion efficiency is essential and in the recent years the progress has started to show for Cu_2O. With a band gap of 2.1 eV, Cu_2O has the potential to reach conversion efficiencies of $\sim 20\%$ according to the Shockley-Queisser limit.

Because of the inability of *n*-type doping the focus has mainly been on heterojunction solar cell devices with a ZnO based *n*-type emitter layer. Before 2011 no cells were reported with higher efficiency than 2%, however since then improved interface quality and the introduction of buffer layers which modify the band structure has led to significant improvements in the last years[11, 35, 36]. The currently highest conversion efficiency is 8.1% for a ZnO/Cu_2O heterojunction cell ($MgF_2/Al - dopedZnO/Zn_{0.38}Ge_{0.62} - O/Cu_2O : Na$) [11]. These results are achieved on thermally oxidized copper sheets (0.2 mm thick) which generally show higher efficiencies due to improved quality over those deposited with thin film techniques[37]. The sheets have a high hole mobility of approximately $100cm^2/Vs$, which is higher than reported values for thin films. This indicates poorer crystal quality in Cu_2O thin films which is of special importance at the interfaces and overall performance of the cells [36].

Thin films are preferred over thick wafers, not only due to practical considerations, but thin film would also enable tandem solar cells with ZnO/Cu_2O as the top cell. A theorized design of a ZnO/Cu_2O subcell on top of a silicon based bottom cell is illustrated in figure 2.12. Alone silicon has maximum theoretical efficiency of 29.8% [38], and Cu_2O as stated $\simeq 20\%$, combined in a tandem structure the efficiency could reach $\simeq 41\%$ [36].

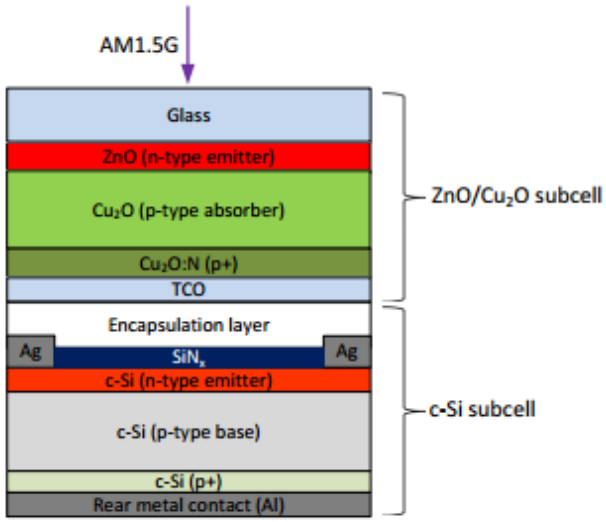

Figure 2.12: Illustration of a four-terminal tandem heterojunction solar cell with a conventional crystalline silicon bottom subcell and a ZnO/Cu_2O top subcell. From Nordseth *et al.* [39].

2.6 Nitrogen doping of Cu_2O

Nitrogen is a non-toxic, low-cost and abundant material which can be active as an acceptor in Cu_2O if incorporated into the oxygen lattice site [40].

$$O_O^x \xrightarrow{N} N_O^{/} + h^{\bullet} + \frac{1}{2}O_2 \tag{2.22}$$

Ishizuka *et al.* [40] is to the best of my knowledge the first to report on nitrogen doping in thin film Cu_2O. They reported that the nitrogen did indeed act as an acceptor with acceptor energy level of 0.14 eV above VB. The film resistivity was reduced down to $15.2\Omega cm$ with a carrier concentration of about $10^{17}cm^{-3}$. Other reports also show successful nitrogen doping by reactive magnetron sputtering. Lai et al. [14] and Lee et.al [15] both reported decreased resistivity to $1.2\times10^{-1}\Omega cm$ and $1.9\times10^{-1}\Omega cm$ and doping concentration of $5.7\times10^{18}cm^{-3}$ and $1.1\times10^{19}cm^{-3}$ at 300 K, respectively. Further Lee *et al.* [15] investigated the role of a N doped layer as a hole transporting layer in thin-film solar cells. They reported that the introduction of a 20 nm-thick $Cu_2O:N$ layer between a silver back contact and a Cu_2O light-absorption layer enhances fill-factor and power conversion efficiency of the solar cells due to improved back contact properties.

Siah et al. [13] studied the effect of nitrogen doping on contact resistivity of metals. In the paper they find that for high doping levels (p > $10^{19}cm^{-3}$) they achieve low resistive Ohmic contacts with earth abundant metals like Cu and Ni. Additionally, the conduction mechanism was investigated and with doping the conduction mechanism changes from thermionic emission to be increasingly dominated by tunneling (field emission) at elevated doping levels. Again this is supported by the findings of Lee *et al.* [15].

In all of the above studies reactive sputtering was used to introduce the nitrogen dopant, Sberna *et al.* [41] is the only report found utilizing ion implantation. The implantation was done on

sputtered Cu_2O thin films.

They achieved a carrier concentrations of $4.75 \times 10^{17} cm^{-3}$ for the highest doped sample (dose of $1.9 \times 10^{16} cm^{-2}$, 2.5N %); up from $3.1 \times 10^{16} cm^{-3}$ for the undoped sample, with a resistivity of $7\Omega cm$; down from $62\Omega cm$ and mobility of $1.3 cm^2/Vs$; down from $4 cm^2/Vs$.

3 | Experimental Methods

3.1 Sputtering

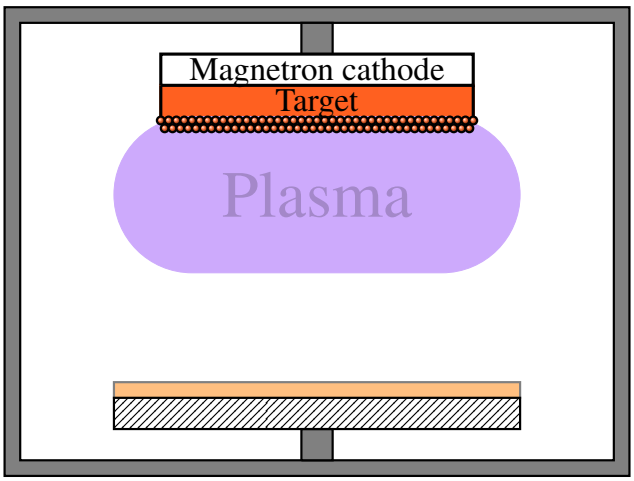

Figure 3.1: Simple schematics of a sputtering chamber

This section is based of the studies by Campbell [20] and Frey & Hamid [42].

Sputtering was discovered in 1852 and developed by Langmuir as a thin film deposition method in the 1920s. The word sputtering comes from the German word "sputteren" which means to spit or an uncontrolled ejection of small particles of saliva when talking. In sputtering deposition, an ionized gas, preferably inert, is accelerated by an electric field bombarding the desired target material. In the process, the target material physically dislodge, 'spit', atoms and clusters out into the chamber and when they reach the substrate they are deposited such that a thin film may form.

There are two main modes of sputtering operations: Direct current (DC) and radio-frequency (RF). In DC sputtering, the cathode electrode is the target material and the substrate is placed on the anode (substrate holder). The target material in a DC setup must be electrically conductive, if not a surface charge will build up which retards and ultimately stops the ion bombardment of the target surface. When sputtering insulating materials, RF sputtering must be used as it utilized alternating current which prevents charge build up. DC sputtering features a larger deposition rate as compared to RF sputtering.

Glow Discharge

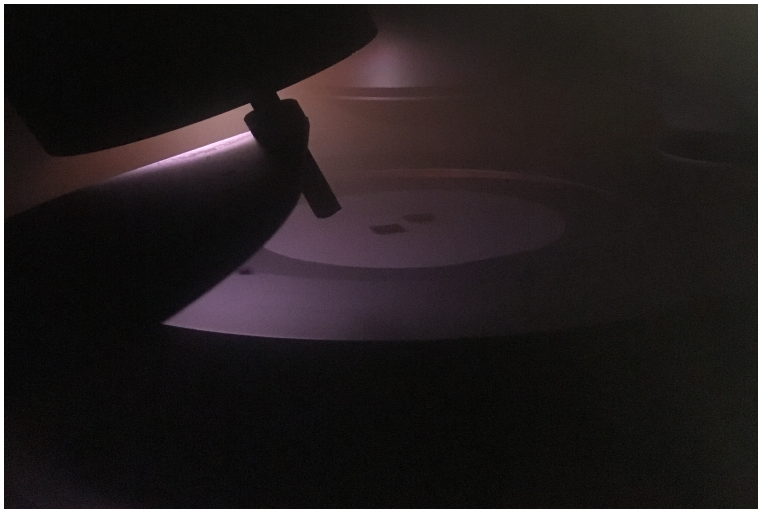

Figure 3.2: Glow discharge below the target in an active sputtering chamber

Plasma is often referred to as the fourth state of matter, it is a partially ionized gas consisting of positively and negative charged particles, ionized atoms or molecules and electrons, respectively. The plasma in our process is often called glow discharge. This comes from luminescence of atoms not fully ionized but excited, and as they relax into the ground state they emit photons which gives the characteristic glow as seen in Figure 3.2.

In a typical sputter set up as illustrated in Figure 3.1 two parallel plates are connected to a dc supply in a vacuum chamber. The typical pressure is 1-5 mTorr. The gas is initially insulating, when either a large voltage is applied to overcome the break down field of the gas or a filament can be used to inject electrons and ignite the plasma. Once the plasma is ignited, free electrons and ionized gas atoms are accelerated in opposite directions between the two electrodes. The breakdown voltage is given by Paschen's law

$$V_{bd} \propto \frac{P \times L}{logP \times L + b} \tag{3.1}$$

where P is the chamber pressure, L is the electrode spacing and b a constant related to the gas.

The electrons will be accelerated towards the anode and the positive ions towards the negatively charged cathode. When they finally reach and hit the cathode they will release a cloud of secondary electrons from the cathode target material, these electron will then be accelerated back towards the anode. If accelerated to high enough energies they will by inelastic collisions ionize new gas atoms and thus maintain the plasma.

When the ions reach the target surface several interactions may occur, ions with low energy ($< 10eV$) can be scattered from the surface conserving energy or absorb on it and deposit energy to phonons (heat). At higher energies upwards to some keV's most of the energy transfer is done within the first few atomic layers in the target. Some energy goes to heat transfer and the remainder goes to physical rearrangement, defects or electronic excitation. When this happens target atoms

and clusters are ejected from the surface with energies of 10 to 50 eV. This is about 100 times more energy than evaporated atoms ($\sim 0.2eV$) and thus the surface mobility is higher for sputter deposition, resulting in better step coverage . About 95% of the sputtered/ejected material is atomic, the rest is mostly diatomic molecules. At higher energies exceeding 5 keV the ions are implanted deeper in the target substrate where the energy is transfered as heat and physical rearrangement within the substrate.

Magnetron Sputtering

Magnetron Sputtering is a High Density Plasma (HDP) method, which refers to systems where the density of ions in the plasma is high. In normal sputtering systems the ion density is 0.001%, while in magnetron systems it can be as high as 0.03%. The increased ion density increases the bombardment of the target increasing the overall sputtering yield.

When a magnetic field is present in the plasma charged particles will be deflected perpendicular to the direction of motion following the Lorentz force

$$\mathbf{F} = \mathbf{q}(\mathbf{v} \times \mathbf{B}) \tag{3.2}$$

Where v is the ion velocity, q is the charge of the ion and B the magnetic field strength. Because of their large mass the ions will travel through the field practically unaffected. The electrons will however be affected and enter an orbital motion following

$$r = \frac{mv}{qB} \tag{3.3}$$

Where m is the ion mass and r the radius of curvature. If the field is large enough and aligned properly we can get what is known as a *Magnetron*, which confines the ejected secondary electrons in loops above the target cathode, effectively increasing the sputter deposition rate.

3.2 Ion implantation

This section is based on the works by Campbell [20] and Mayer [43].

Ion implantation is a process designed to introduce foreign impurity atoms in a target wafer. The ions are accelerated by an electric field leading to bombardment of the target wafer. Thus, by varying the energy and the dose of the impurity atoms, one can design the desired impurity concentration profile in the wafer.

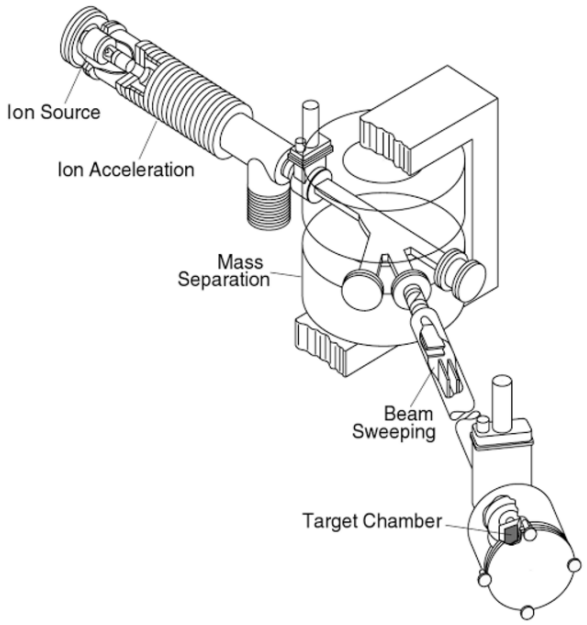

Figure 3.3: Schematic drawing of an ion implantion system. A mass-separating magnet is used to select the ion species of interest. Beam-scanning facilities are required for large area uniform implantation. Retrieved from [43]

The implantation system can be divided into four main components, Ion source and acceleration, mass spectrometer, beam scanning/lens apparatus and finally the sample holder. The ion source is commonly either a gas feed or a vapor from a solid source. The gas or vapor is brought into a plasma which cracks and ionize a fraction of the injected species. A magnetic field can be applied to increase the plasma density for improved ionization efficiency. The ions are then accelerated further through the apparatus by an applied voltage, this can be done both before and after the analyzing magnet. The beam can now consist of several species depending on the source, and the desired ions need to be selected. This is done with an analyzing magnet, the beam is bent in a magnetic field only allowing the ions with the right mass, velocity and charge through a slit at a specific angle following.

$$\frac{mv^2}{r} = qvB \tag{3.4}$$

The beam is focused into a spot by using a set of electrostatic lenses. Most implantation systems then have a set of horizontal and/or vertical plate deflectors which by applying a voltage can scan the beam to write uniformly across the wafer.

When an energetic ion enters the target it will interact with both the atoms nucleus and electrons, hence lose energy and eventually stop. The stopping power from electron interactions, S_e and nuclear interactions S_n dominate at different energies of the incident ion. The electrons have very low mass and thus for each individual interaction little momentum is lost. However, hundreds of thousands of these interaction occur and collectively they contribute to a drag force and can be approximated by a continuum mechanism. A viscosity can be assigned to the crystal media and the energy loss per unit length due to electric stopping follows

$$S_e = k_e\sqrt{E} \tag{3.5}$$

where E is the energy of the incident ion and k_e is a constant that depends on the ion and target species. From this we see that the stopping power increases with energy and electronic stopping dominates at high energies. This relation is valid for most energies practical for ion implantation, but at very high energies the viscous model is no longer valid. At really high energies the stopping power reaches a maximum before decreasing for even higher energies.

The nuclear stopping is due to elastic collisions, it can be qualitatively explained by screened Coloumb scattering events. Nuclear interactions can not be considered a continuum but rather as individual scattering events dependent on the angle of incident ion, impact parameter and on the masses and relative position of the colliding species. The energy loss is proportional to the incident energy and scattering angles which again depend on the ion masses and the impact parameter. Further, energy loss is a function of the ratio of the mass of the incident ion and target nucleus, the smaller the ratio is the larger the energy loss will be. At low implantation energies, the collisions will displace less target atoms, therefore the stopping power is expected to decrease for low energies. At higher energies it will reach a maximum and then decrease. This is because at high energy the ion velocity is high, and the interaction time between the ion and nucleus becomes short with little change of the momentum.

As a first approximation, a Gaussian distribution can be used to model the range of depths N(x) which a ion might reach in the target material. This is given by:

$$N(x) = \frac{\phi}{\sqrt{2\pi}\Delta R_p} e^{-(x-R_p)^2\Delta R_p^2} \tag{3.6}$$

where R_p is the projected range of the ion, ΔR_p is the standard deviation of the projected range (straggling) and ϕ is the dose. The equation is normalized such that the integral from 0 to ∞ gives the dose.

The projected range and standard deviations can be obtained from tables or Monte Carlo simulations. A common program is SRIM which uses the Monte Carlo technique to simulate multiple ion trajectories to develop implantation statistics. It is widely used and claimed to have an overall accuracy of 85% (the data agree within 10% of experimental data) [44]. From the SRIM calculations one can find the dose required for a desired dopant concentration. The possibility to tailor implantation profiles from simulations and its reproducibility is a great resource and one of the main advantages of ion implantation.

Ion implantation has some drawbacks that must be considered for certain applications. Very shallow or deep profiles can be difficult to realize. The ion bombardment damages the crystal structure which limits the performance of many devices. The crystal structure can in many cases be restored via annealing, but has proven difficult for others.

3.3 X-Ray Diffraction

This section is based on the studies by Birkholz [45] and Leng [46]

X-ray diffraction (XRD) is a powerful tool to determine the structure of crystalline materials. X-rays are photons with an energy of 125 eV - 125 keV ($\lambda \sim 0.01 - 10nm$). The wavelength of x-rays corresponds well with the interatomic distances in crystals and molecules ~ 0.15 - $0.4nm$. Diffraction effects can be observed, more specifically constructive and destructive interference is observed when x-rays interact with crystalline structures.

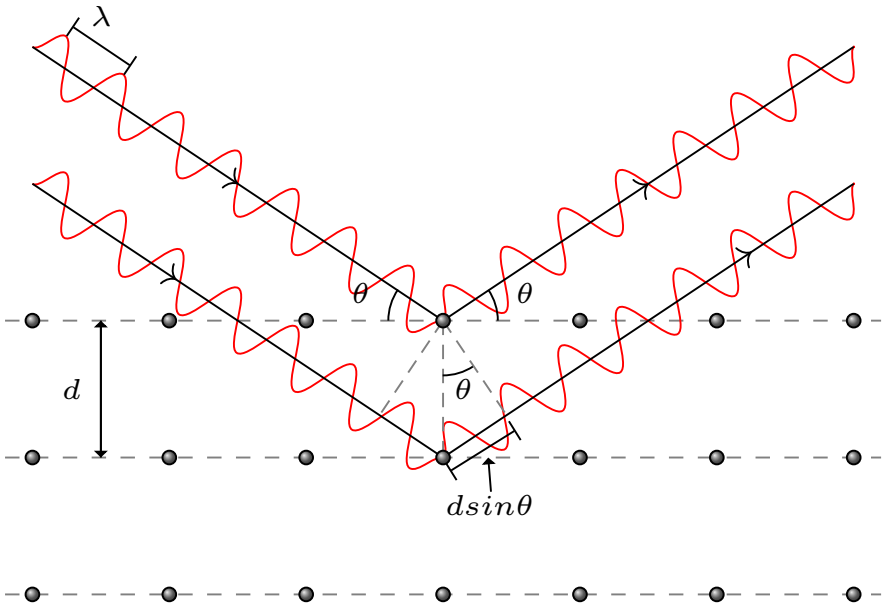

Figure 3.4: Visualization of the bragg condition, constructive interference when the incident angle θ and plane separation d satisfy the Bragg condition $n\lambda = 2dsin(\theta)$.

When x-rays are incident on a solid several interactions with the atoms may occur. Three interactions are relevant for the energies at hand, Compton scattering, photoionization and Thompson scattering. Compton scattering is an inelastic scattering of the incident photon, resulting in a shift to lower energies for the emitted photon. The energy difference is transferred to the scattering electron. Photoionization is another inelastic scattering mechanism where the incident photon transfers energy and momentum which liberates a bound electron into a "free" photoelectron. Finally, the photons may scatter elastically in Thompson scattering. In this case the incident x-rays are scattered elastically by collective oscillations by the electrons at the same frequency as the incoming x-rays. The oscillating electrons behave as a Hertz dipole and become a source of dipole radiation. In

Thompson scattering the wavelength of the incoming radiation is conserved and it is this emission which is used in x-ray diffraction. The scattering intensity scales inversely with the square of the oscillating particles mass which results in a negligible contribution from nuclei.

The incoming radiation can be described by a wave vector $\mathbf{K_0}$ and the scattered wave vector $\mathbf{K}$. The difference between the incoming and scattering wave vector is called the scattering vector $\mathbf{Q}$;

$$\mathbf{Q} = \mathbf{K} - \mathbf{K_0} \tag{3.7}$$

$\mathbf{Q}$ can be understood as an analogy to mechanical momentum transfer and is therefore also called the vector of momentum transfer. In kinetic theory of gas molecules with momentum $\mathbf{p_0}$ before collision and $\mathbf{p}$ after with a difference $\mathbf{p} - \mathbf{p_0}$ is the analogy to $\mathbf{K} - \mathbf{K_0}$ for the scattered photon. M. von Laue described the relation between lattice vectors $\mathbf{r_{n_1 n_2 n_3}}$ and scattering vector $\mathbf{Q}$ at which constructive inteference and intensity maximum is obtained. The Laue conditions for cubic crystals are

$$\begin{aligned} a\mathbf{Q}\mathbf{c_1} &= 2\pi h \\ a\mathbf{Q}\mathbf{c_2} &= 2\pi k \\ a\mathbf{Q}\mathbf{c_3} &= 2\pi l \end{aligned} \tag{3.8}$$

where *a* is the lattice constant, $\mathbf{c_{1,2,3}}$ are the lattice vectors and h,k,l are miller indices of the planes contributing to the scattering. The magnitude of $\mathbf{Q}$ can be found from the absolute value of the sum from the three crystal directions in equation 3.8.

This gives us the condition for maximum intensity as

$$\frac{|\mathbf{Q}|}{2\pi} = \frac{\sqrt{h^2 + k^2 + l^2}}{a} \tag{3.9}$$

From the geometry in figure 3.5 this can be rewritten as

$$\lambda = \frac{a}{h^2 + k^2 + l^2}\, sin\theta \tag{3.10}$$

where λ is the wavelength of the incident radiation.The interplanar distanse between two adjacent planes is given by $d_{h,k,l}$ for the plane with corresponding miller indices h,k and l. For a cubic crystal with lattice constant *a* this distance can be found as

$$d_{h,k,l} = \frac{a}{h^2 + k^2 + l^2} \tag{3.11}$$

This together with eq 3.9 leads us to the final equation

$$d_{h,k,l} sin\theta_B = \lambda \tag{3.12}$$

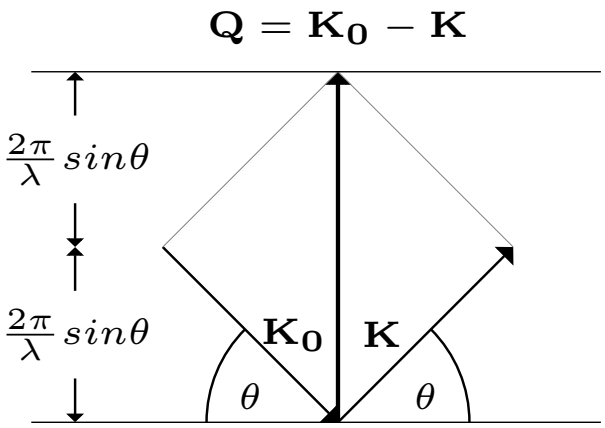

Figure 3.5: Geometry of scattering vector $\mathbf{Q}$ and visualization of its magnitude $|\mathbf{Q}|$

where θ_B is the Bragg angle, which is the angle at which maximum reflection is detected. Equation 3.12 is the Bragg equation which is well known and frequently used in XRD analysis. It connects the angle of observed maximum and the interplanar distances $d_{h,k,l}$. The Bragg equation may also be obtained geometrically as shown in Figure 3.4. This is done by calculating the path difference for two incoming beams which is reflected from adjacent planes, to stay in phase their path difference 2d sinθ must be equal to or a multiple of their wavelength, $n\lambda$. Bragg's law can be used to find the inter-planar distances for all crystal structures and by Equation 3.11 determine the lattice constant of a simple cubic system. Equation 3.11 is simple for the cubic crystal system but similar more complex expressions are derived in literature for other crystal systems.

θ/2θ scan

In θ/2θ scan the reflected intensities are measured as a function of the angle between the incoming and diffracted beam 2θ. This is typically done by moving the x-ray source and/or the detector around the circumference of the sample stage. This way we get a diffractogram which can be used as a materials "fingerprint". The International Centre for Difraction Data (ICDD) has determined and published the relationship between deflection angle and planes for most crystalline materials, given λ. Diffractograms of the measured material can easily be used to determine and detect different phases by comparing it to the ICDD standards.

3.4 Four-point probe measurements

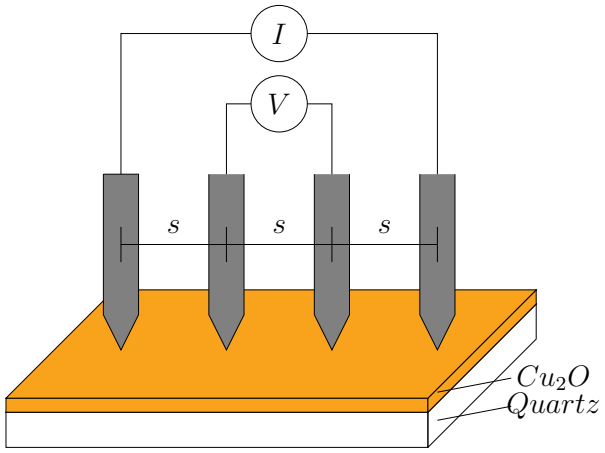

Figure 3.6: Illustration of the four point-probe set up.

This section is based on the studies by Smits [47] and Valdes [48].

The four-point probe technique is a convenient way to measure resistivity and sheet resistance R_s. It is set up by four equidistant probes that make contact with the sample at a straight line. A current I is passed between the outer pair while the floating potential is measured over the inner pair. The setup is illustrated in figure 3.6. For a semi-infinite slice of finite thickness t, the resistivity can be found from the relation:

$$\rho = R_s t = \frac{\pi t}{ln2}\frac{V}{I}F(\frac{t}{s}) \tag{3.13}$$

where F is a geometrical correction factor which depends on the ratio between the probe spacing s and sample thickness t, F approaches unity as t approaches zero. If the ratio is less than 0.4 the correction factor is no more than 0.9995 and is therefore considered negligible for thin samples. In this case the resistivity is found as

$$\rho = \frac{\pi t}{ln2}\frac{V}{I} = 4.532t\frac{V}{I} \tag{3.14}$$

3.5 Hall Effect Measurements

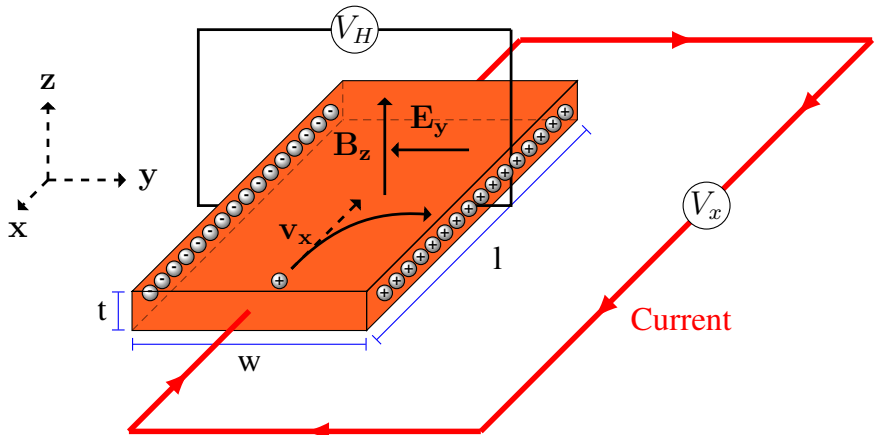

Figure 3.7: Illustration of the hall effect in a p-type semiconductor.

This section is based on the books by Streetman [17] and Kittel [16].

Hall effect measurements is a powerful method giving information about a samples electrical properties such as carrier concentration, resistivity, conductivity and mobility. When current flows through a material in the presence of a magnetic field perpendicular to the carriers flow they will be affected by the Lorentz force following the right hand rule as illustrated in figure 3.7. The total force on a single hole due to the the electric and magnetic field is

$$\mathbf{F} = \mathbf{q}(\mathbf{E} + \mathbf{v} \times \mathbf{B}) \tag{3.15}$$

where **F** is the force , q the charge, **v** the carriers drift velocity, **E** the electric field and **B** the magnetic field. To maintain steady state flow across the material an electric field is set up in the -y direction due to the shift in hole distribution, the lorentz force is now opposed and the total force F_y remains zero. The establishment of this electric field is the Hall effect and the resulting voltage $V_H = E_y w$ is known as the Hall voltage. Equation 3.15 can be rewritten as

$$E_y = v_x B_z \tag{3.16}$$

The Drift velocity can be expressed as $v_x = \frac{[J_x]}{qp}$, where J_x is the current density, q the carriers charge and p the concentration of charge carriers, in our case holes. The field now becomes

$$E_y = \frac{J_x}{qp} B_z = R_H J_x B_z, \quad R_H \equiv \frac{1}{qp} \tag{3.17}$$

where R_H is the Hall coefficient.

Now this is a handy relation, by controlling the current density and magnetic field while measuring the Hall voltage for a sample with known dimensions w, t and l you can directly find the hole concentration since

$$p = \frac{1}{qR_H} = \frac{J_x B_z wt}{qE_y wt} = \frac{I_x B_z}{qV_H t} \tag{3.18}$$

where $I_x = wtJ_x$ is the current through the sample. Further by combining the above result with a measurement of the reistance R, the samples resitivity, conductivity and mobility can be determined in accordance with the following relations.

$$\rho = \frac{Rwt}{l} = \frac{V_x wt}{I_x l} \tag{3.19}$$

Since $\sigma = \frac{1}{\rho}$ and $\sigma = q\mu_p p$, where σ is the conductivity and μ_p the hole mobility which can be found as

$$\mu_p = \frac{1}{\rho q p} = \frac{R_H}{p} \tag{3.20}$$

In the above discussion a p-type material have been used as an example, however all the above is also valid for n-type materials, as long as the sign of the charge q is changed. The sign of the measured quantity R_H is related to the type of charge carriers present, making it a quick way to determine the majority carrier type of the material.

Van der Pauw

This subsection is based on the studies by Campbell [20] and Van der Pauw [49].

The Van der pauw method is a technique to measure the Hall coefficient (R_H) and resistivity of a sample. It was discovered in 1958 by L. J. Van der Pauw. He proved that for a flat sample of arbitrary shape this method is valid if 4 conditions are met:

- The contacts are at the circumference of the sample.
- The contacts are sufficiently small.
- The sample is homogeneous in thickness.
- The surface of the sample is singly connected, i.e the sample does not have isolated areas.

The measurement is done by contacting four points along the edge of the sample, labeled 1 to 4. Current are forced between two adjacent contacts while the voltage is measured between the two others. When the four conditions above are met J. Van der Pauw proved that the following relation holds:

$$e^{-(\frac{\pi t}{\rho} R_{12,34})} + e^{-(\frac{\pi t}{\rho} R_{23,14})} = 1 \tag{3.21}$$

where t is the thickness of the sample, ρ the resistivity, $R_{12,34}$ is resistance determined by dividing the current that flows through contact 1 and 2 by the voltage measured over contact 3 and 4. $R_{23,14}$ Is defined in the same way with a different geometry. To improve accuracy the measurement can be done over all contacts combinations and reversing the current yielding 8 measurements. The two characteristic resistances R_a and R_b can be defined as:

$$R_a = \frac{1}{4}(R_{12,34} + R_{23,41} + R_{34,12} + R_{41,23}) \tag{3.22}$$

$$R_b = \frac{1}{4}(R_{32,41} + R_{23,41} + R_{14,23} + R_{41,23}) \tag{3.23}$$

The resistivity can now be found through the relation in equation 3.21 when the thickness and resistances are known as:

$$\rho = \frac{\pi t}{ln2}\frac{R_a + R_b}{2}F(Q) \tag{3.24}$$

where F(Q) is a factor which is a function of the ratio R_a/R_b. If the sample has symmetry the process is more straightforward, and for a square sample F(Q) = 1.

Temperature dependent Hall effect measurements

This subsection is based on the work by Blood $ Orton [50] and Biccari [21].

From Hall effect measurements one probes the free carrier density in the material as expressed by Equation 3.18. Additionally, it is desirable to determine the number of electrical active impurities in the sample. This is of particular interest with regard to doping, as this can give information whether the dopant is successfully incorporated as an acceptor or donor. Additionally, it can provide information if other impurities have been incorporated or created accidentally compensating the intentional dopants. This information can be analyzed by temperature dependent Hall measurements where the Hall coefficient (carrier density) and resistivity is tracked versus temperature.

The following equations are defined for a non-degenerate ($E_c - E_f \geq 3kT$) compensated p-type semiconductor containing N_a shallow acceptors and N_d compensating donors. A modified version of the space charge neutrality (2.18)

$$p + p_a = N_a - N_d \tag{3.25}$$

together with

$$p = N_V e^{-\frac{E_F - E_V}{kT}} \tag{3.26}$$

and

$$p_a = N_a \frac{1}{1 + \beta e^{-\frac{E_F - E_a}{kT}}} \tag{3.27}$$

where p_a is the density of holes provided by acceptor atoms, E_a is the acceptor energy level β is a factor which accounts for the degeneracy of the acceptor level ($\beta = 1/2$ for a single acceptor),

E_V is the energy of the valence band top and N_V is the effective density of states at the valance band edge $N_v = 2\left(\frac{2\pi m_p^* kT}{h^2}\right)^{3/2}$, where m_p is the holes effective mass. This results in the following expression

$$p^2 + p(N_d + \beta N_c e^{-\frac{E_d - E_a}{kT}}) - (N_a - N_d)\beta N_c e^{-\frac{E_d - E_V}{kT}} = 0 \tag{3.28}$$

when solving for p this can be fitted to the measured carrier densities at varying temperatures. Parameters like E_a, N_a and N_d can be found. At high temperatures where $kT >> E_d - E_V$, all the acceptors are ionized and therefore *p* approaches the acceptor concentration N_a (the extrinsic region in figure 2.8).

3.6 Transmission Measurements

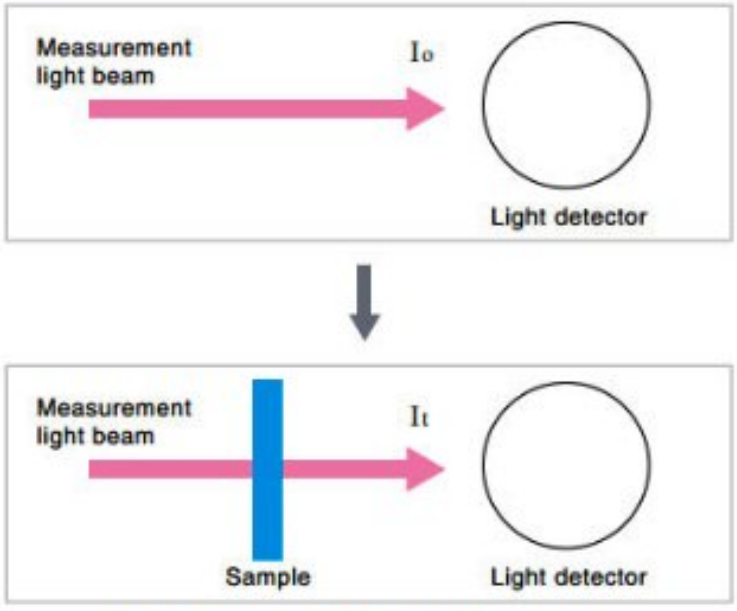

Figure 3.8: Measurement principle for solid samples. Retrieved from [51]

Based on the studies by Schroeder [52] and Streetman [17].

An important tool to determine the optical band gap of a semiconductor is the absorption of incident photons in the material.

Under transmission measurements light is incident on the sample and the transmitted light is measured as a function of the wavelength. It can be expressed in percentage by

$$T_{\%} = \frac{I_t}{I_0} \times 100 \tag{3.29}$$

where T is the transmittance, I_t the measured light intensity that made it through the sample and I_0 the incident intensity of the light.

Photons from a light source pass through a monochromator such that the transmittance can be measured for individual photon energies/wavelengths, a typical setup can be seen in figure 3.8. In order to get accurate measurements a baseline is usually obtained before the sample measurements. This is to reduce error sources and account for losses due to the experimental setup.

The absorption in a material is expected to follow *Beer Lamberts law*:

$$I_t = I_0 e^{-\alpha t} \tag{3.30}$$

where α is the absorption coefficient of the material and t is the material thickness. The transmission spectra obtained from the measurement can be recalculated into an absorption spectra through

$$\alpha = \frac{1}{t} ln(\frac{100}{T_{\%}}) \tag{3.31}$$

Since photons with energies less than the band gap of the material are expected to be transmitted and photons whit higher energy are generally absorbed in a semiconductor this method can give an accurate measurement of the materials optical band gap energy. When you have the absorption spectra one can find the optical band gap through the Tauc relation:

$$(\alpha * hv)^{1/n} = A(hv - E_g) \tag{3.32}$$

where h is Plank's constant,, v is the photon frequency and A is a proportional constant. The value of the exponent n in eq. 3.32 is determined by the nature of the transition. n = 1/2 for direct allowed transitions, n = 3/2 for direct forbidden transitions, n = 2 for indirect allowed transitions and n = 3 for indirect forbidden transitions[53]. By plotting this relation ($((\alpha * hv)^{1/n})$ versus the photon energy hv) one will get a linear region when plotting for the appropriate transition, by extrapolating this linear region to the abscissa one can find an estimate of the optical band gap energy E_g.

3.7 Secondary Ion Mass Spectrometry

Secondary ion mass spectrometry (SIMS) analyses the atomic masses of ions emitted from a surface to examine elemental purity. It is widely used both in academia and industry to determine isotopic, elemental or molecular impurities over a highly localized microscopic region near the surface of any solid. Its wide us can in part be owed to these four attributes: The ability to detect all elements in the periodic table and certain molecules. The detection limits of SIMS are in the sub parts per billion, and the ability to detect signals over a dynamic range spanning up to 5 orders of magnitude when using multiple detectors. Detailed mapping of any isotope within any solid with spatial and depth resolutions of down to $1\mu m$ or less (an ultimate limit in SIMS is $\sim 10nm$) and $\simeq 1nm$, respectively. Little or no sample preparation is required before analysis. Additionally, SIMS can monitor concentration of several species during the same run.

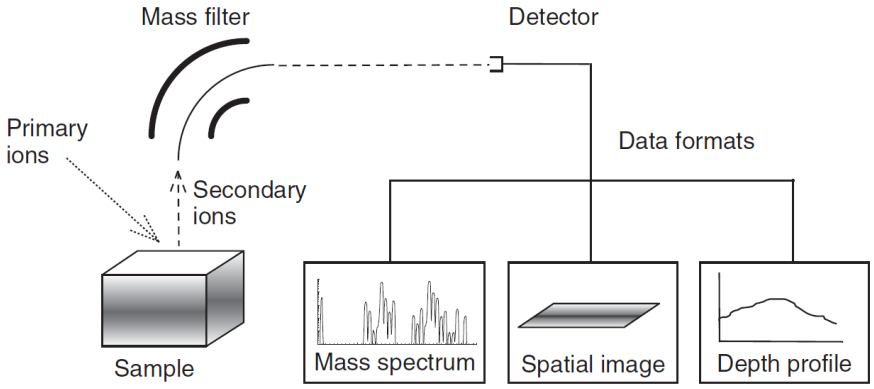

Figure 3.9: Illustration of a SIMS apparatus depicting the main components of operation and the common data output noted in Dynamic SIMS. Retrieved from [54]

Figure 3.9 shows a typical SIMS setup. The sample is put into a high vacuum chamber (around 10^{-9} torr) A focused ion beam (usually at energies $\simeq 0.1 - 50keV$) of what is referred to as the primary ions impact the target sample, in the process ions are sputtered from the target, now referred to as secondary ions. The secondary ions are then collected, focused, accelerated and passed through a mass spectrometer. SIMS has two main types of operation, the first is Static SIMS using slow erosion rates to probe the outer most monolayer of the surface. Dynamic SIMS has an increased erosion rate and is used to analyse depth distributions. By combining depth distribution mapping and spatial mapping detailed three-dimensional volumetric distributions can be generated.

A disadvantage of SIMS data is the difficulty to quantify the recorded signals. The recorded intensities can vary from day to day due to many uncertain factors such as exact sputter yield, collection efficiency, ionization efficiency and detector sensitivity. The current practice to deal with this is to run a calibration sample for each impurity immediately before or after data collection on the desired sample. Usually, calibration samples are made by ion implantation, since both concentration and depth of the profile are well known. This way the intensity counts/s can be converted into absolute concentration in $atom/cm^3$, giving quantitative analysis of desired impurities. Depth profiles can also be converted from time to depth by measuring the depth of the final crater, by i.e profilometry and assuming a constant erosion rate.

3.8 Equipment used

Laser cutting A Rofin laser cutter were utlized for cutting the samples. It was run at 50 kHz, 32 A with a speed of 400 mm/s and execution count of 300 scribes.
Sputtering The Cu_2O films were deposited in a Semicore TriAxis magnetron sputtering system. The target used was a circular copper plate with dimensions of 3 inch in diameter and 0.25" in thickness, the target-substrate distance was 10 cm.
XRD characterization X-Ray Diffraction characterization was performed by x-ray diffraction (Bruker AXS D8 Discover) with a Cu $K\alpha$ radiation ($\lambda = 1.5406$) scanned over the angles 20^o to 80^o 2θ.
Transmission Measurements UV-VIS. spectrophotometer (Shimadzu SolidSpe-3700 DUV) was employed in the spectral range 400-1400 nm in an integrating sphere setup to determine transmittance and optical band gap estimations by the Tauc-method.
Hall Effect Measurements Room temperature Hall measurements and temperature dependent Hall measurements (LakeShore 7604) using Van-der Pauw configuration were conducted to determine film carrier mobility μ, carrier density N and resistivity ρ in the temperature range 140-320 K. Contacts were made by soldering Ag wires onto the corners of the samples by In contacts.
Four-point Probe 4-pp measurements were obtained using Jandel KM3-AR setup with a current range of 10nA-99mA.
SIMS SIMS measurements were done by Alexander Azarov at University of Oslo using a Cameca IMS7f microanalyzer.
Ion Implantation Ion implantation were done at the Ion Technology Centre in collaboration with Uppsala University. The implantations were conducted with three implantation energies of 130, 65 and 20 keV, with doses of 2.4×10^{15}, 1.3×10^{15} and $5.4 \times 10^{14} cm^{-2}$ respectively.
Elipsometry Film Thickness measurements were done utilizing a Woolam Alpha SE ellipsometer by measuring the reflectance at three incident angles [52]. The mathematical model used was defined by Kristin Bergum at University of Oslo for Cu_2O thin films on Si substrate.
Scanning electron microscope Scanning electron microscope images were taken at FERMiO, University of Oslo by Andreas Løken. A FEI Quanta 200 FEG-ESEM system was used.
Sample preparation Double-sided polished 500 μ m thick quartz wafer and silicon wafers have been used as substrates for the Cu_2O films deposited. Si was used only in order to get thickness measurements from ellipsometry. The 3 inch wafers were cut by laser ablation into $1x1cm^2$ squares. The quartz substrates was cleaned In RCA1 and RCA3 steps followed by 10 min in a piranha solution. The Silicon samples were cleaned with the RCA cleaning process. Subsequently, the samples were rinsed and dried in N_2 flow.

3.9 Errors/Accuracy Considerations of Recorded Data

Hall Effect Measurements

Hall effect measurements were done to determine film carrier mobility, carrier density and resistivity. For each sample a variable field strength measurement was employed. The first error source is the discrepancy between the measurements at varying field strengths 4-10 KT. Further, the Van der

Pauw geometry has an instrumental error whenever the contacts are larger than point contacts. The resistivity error scales as $\frac{d}{t}^2$, where d is the length of the sample and t is the contact size. The contact diameter varies in the range of 0.8-1.3 mm and an average contact size is approximated to be 1mm in diameter. With this a maximum error margin for resistivity of 1% for the 1x1 cm samples and 4% for the 5x5mm samples. For the carrier concentration and mobility the error scales as $\frac{d}{t}$, here the maximum error margin is 10% and 20% for the 1x1 cm and 5x5mm samples respectively.

4 Point-Probe

To obtain better statistics when measuring the resistivity using the 4-point-probe, each sample was probed in three different locations. The final resistivity is given by finding the average of the three, additionally the standard error was determined from the three measurements and is illustrated by error bars.

Ellipsometry

The thickness of the films was determined by ellipsometry with a theoretical model designed for Cu_2O thin films on a Si substrate. The error of the measurements is given by the calculated errors of the fitted curves.

4 | Experimental Results and Discussion

In this chapter the experimental results will be presented and discussed. The main focus of this work has been to study the effect of nitrogen doping of Cu_2O thin films by ion implantation, with the expectation of achieving films with low resistivity. One section is dedicated to the sputter deposition of pure Cu_2O films. As a new metallic copper target was installed just prior to the depositions, it was necessary to re-optimize conditions for phase-pure Cu_2O. The optimization was conducted with an emphasis on achieving high mobility, low resistivity and high transmittance of the films, which are important properties for applications as absorber layer and possibly part of a tandem solar cell structure. Further, Rapid Thermal Annealing (RTA) has been employed to further increase the crystallinity and and mobility in the films prior to implantation. Finally, samples both treated with and without a post-deposition RTA were implanted with nitrogen. The effect of post implantation annealing has been investigated at a wide range of both temperature and duration.

4.1 Cu_2O sputter deposition

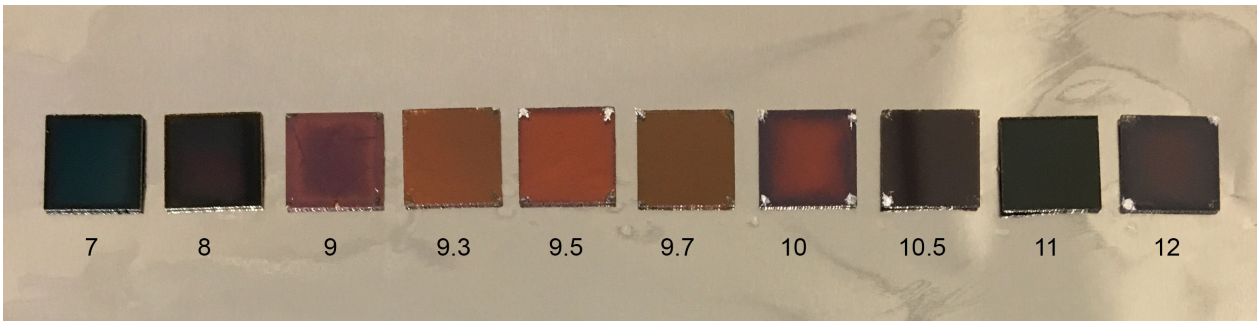

Figure 4.1: Optical image of the samples deposited on quartz substrates with varying O_2 flows in the range $7 - 12\,sccm$.

An important parameter to deposit high quality Cu_2O films has proven to be the O_2 partial pressure during deposition. This is controlled by regulating the gas flow, J_{O_2}, into the chamber during deposition. Prior investigations have shown that a substrate temperature of $400\,^{\circ}\mathrm{C}$, base pressure below 1×10^{-6} Torr and target power of 100W yield good film properties[55]. The oxygen flow, J_{O_2}, was varied in the $5 - 12\,sccm$ range while argon was varied accordingly, to maintain a total flow of $50sccm$. During deposition, the chamber pressure was $7.0\,mTorr$ and the substrate stage

was rotated with a speed of $12\,rpm$. A pre-sputter period of at least 15 min and until the voltage supply had stabilized at $\pm 0.5\,V/min$ was carried out with a closed shutter to ensure a stable sputter deposition condition.

A total of 14 thin films in the range of $5 - 12\,sccm\ J_{O_2}$ were deposited, 10 of these (Figure 4.1) were further investigated by XRD, Hall effect- and transmission measurements to compare structural, optical and electrical properties. From Figure 4.1 one can see that the samples made in the range $9 - 10\,sccm\ J_{O_2}$ have a distinct transparent and brownish/orange appearance customary to Cu_2O thin films [56, 53].

4.1.1 Thickness Measurements

For each deposition, a $1x1\,cm^2$ Si substrate was deposited to deduce the thickness with an ellipsometer [52]. The results of the measurements are displayed in Table 4.1.

Table 4.1: Thin film thickness calculated from ellipsometry measurements on Si substrate.

O_2 flow [Sccm]	Thickness [nm]
9	700 ± 100
9.3	860 ± 50
9.5	815 ± 40
9.7	830 ± 50
10	740 ± 80
10.5	700 ± 70
11	700 ± 60

4.1.2 XRD Result

XRD was employed to ensure phase purity of the deposited films. The following XRD data acquired in this chapter were measured with 2θ angles ranging from 20 to 80^o. The XRD patterns were matched with XRD reference spectra from the bruker data base for Cu_2O, CuO, and metallic copper, Cu.

The XRD results of the films deposited with different J_{O_2} are shown in Figure 4.2. All the 10 films in the range $7 - 12\,sccm\ J_{O_2}$ shows clear Cu_2O peaks, where either the (111) or (200) peaks are present in all samples. Only the samples deposited at the lowest ($7\,sccm$) and highest ($12\,Sccm$) oxygen flow have features suggesting the presence of other phases. The sample prepared at $7sccm$ has a Cu phase presents, while the sample prepared at $12\,sccm$ shows signs of the CuO phase where the Cu_2O(111) and Cu_2O(220) are shifted towards the CuO(-111) and CuO(202) peak positions.

There is a shift in preferred growth orientation with increasing J_{O_2}, for low flows the Cu_2O (111) orientation is dominant over (200), however in the intermediate range $9 - 9.7sccm$ the (200) orientation is dominant before the (111) increases and prevails at higher flows.

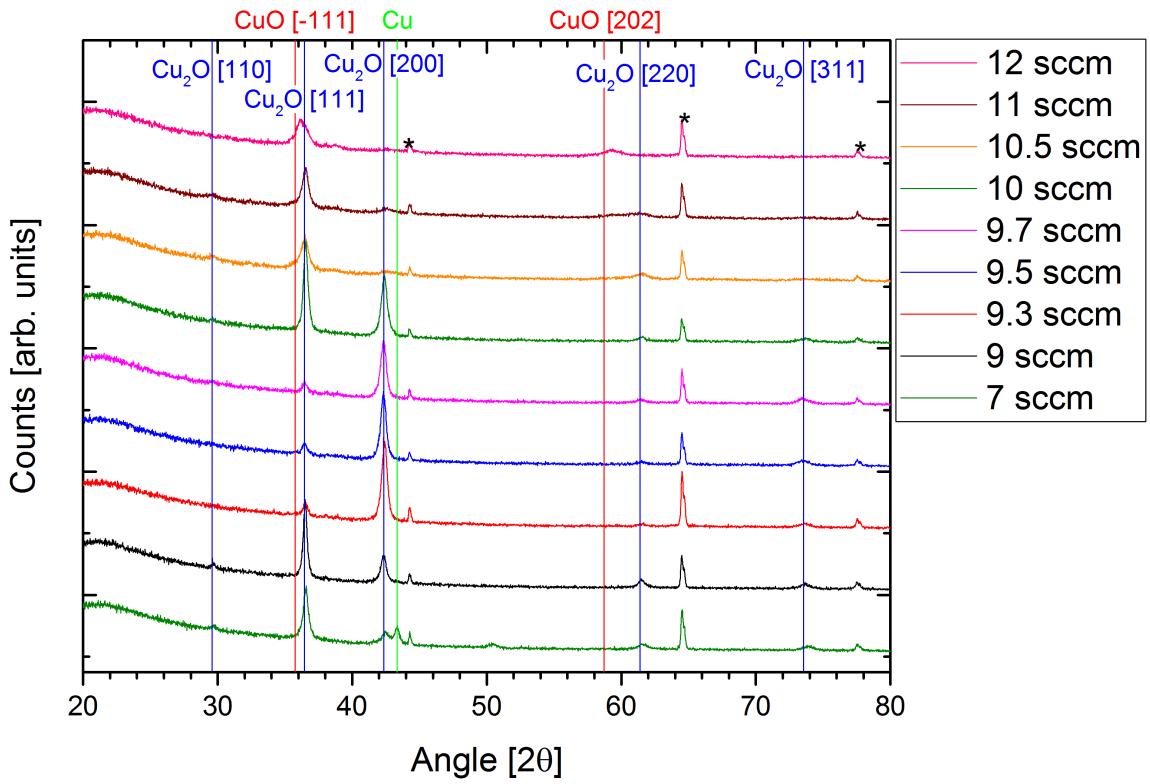

Figure 4.2: XRD results for the Cu_2O films sputtered on quartz substrate with different J_{O_2}. Background peaks are indicated with an asterisk (*).

4.1.3 Hall Effect Measurement Results

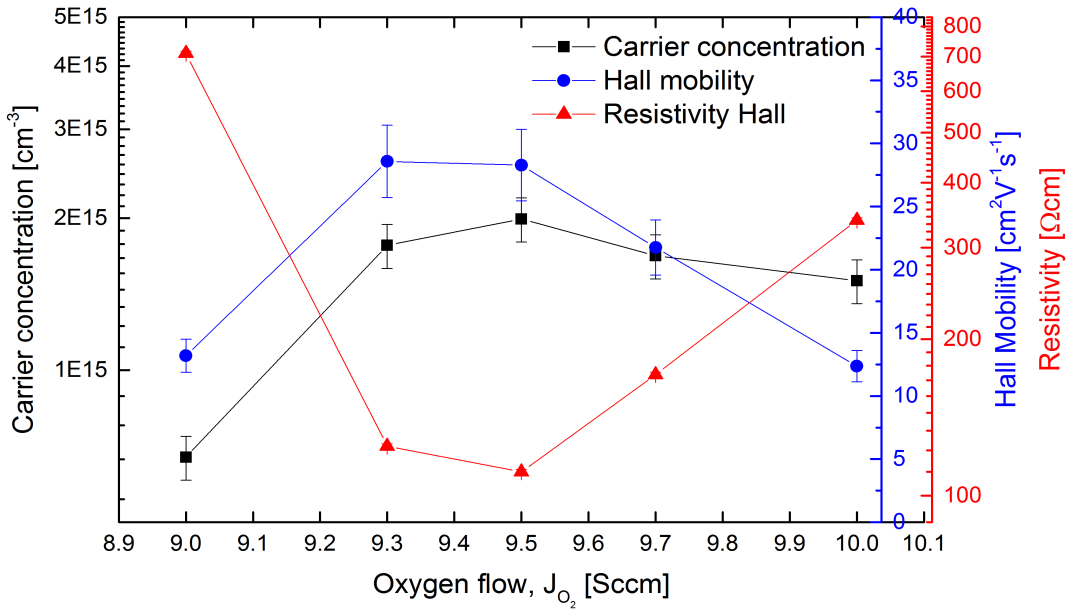

Figure 4.3: Hall measurement data displaying Hall mobility, resistivity and carrier concentration of Cu_2O films deposited on quartz substrates with varying oxygen flow rate J_{O_2} in the range $9 - 10\,sccm$.

The electrical properties (Hall mobility, resistivity and carrier concentration) of the films were found with Hall effect measurements. The thickness of the films used for these measurements was obtained using ellipsometry (Table 4.1). In Figure 4.3 the Hall mobility, resistivity and carrier concentration are plotted as a function of oxygen flow. Only samples with $9 - 10\,sccm$ could be measured, as the remainder of the samples were to resistive to get consistent measurements and were therefore excluded.

There is a clear trend in the measured data where the resistivity reaches a minimum at $9.5\,sccm$ before increasing. Accordingly, the mobility reaches a maximum at 9.3 and $9.5\,sccm$ before there is a reduction at higher oxygen flows. A peak mobility of $28 \pm 3\,cm^2V^{-1}s^{-1}$ is achieved for both the sample prepared at 9.3 and at $9.5\,sccm$. The sample prepared at $9.5\,sccm$ has the lowest resistivity of $111 \pm 1\,\Omega cm$, a little lower than the sample prepared at $9.3\,sccm$ ($125 \pm 1\,\Omega cm$) due to a slightly higher carrier concentration.

4.1.4 Transmission Measurements Results

The transmittance was measured to ensure good optical quality and investigate the trend in transmission; the results can be seen in Figure 4.4. The film deposited at $10\,sccm$ J_{O_2} has a lower transmittance compared to the other films and drops off significantly for wavelengths below $1100\,nm$. CuO has a band gap around $1.2\,eV$ [57] (corresponds to a photon wavelength of $\simeq 1000\,nm$), which would explain the increased absorption in this range. Such a reduction in transmittance

could be an indication of CuO presence in the film not detected by XRD. The highest transmittance is obtained for the films deposited at 9.3, 9.5 and 9.7 $sccm$ which all have peak transmittances above 85 %.

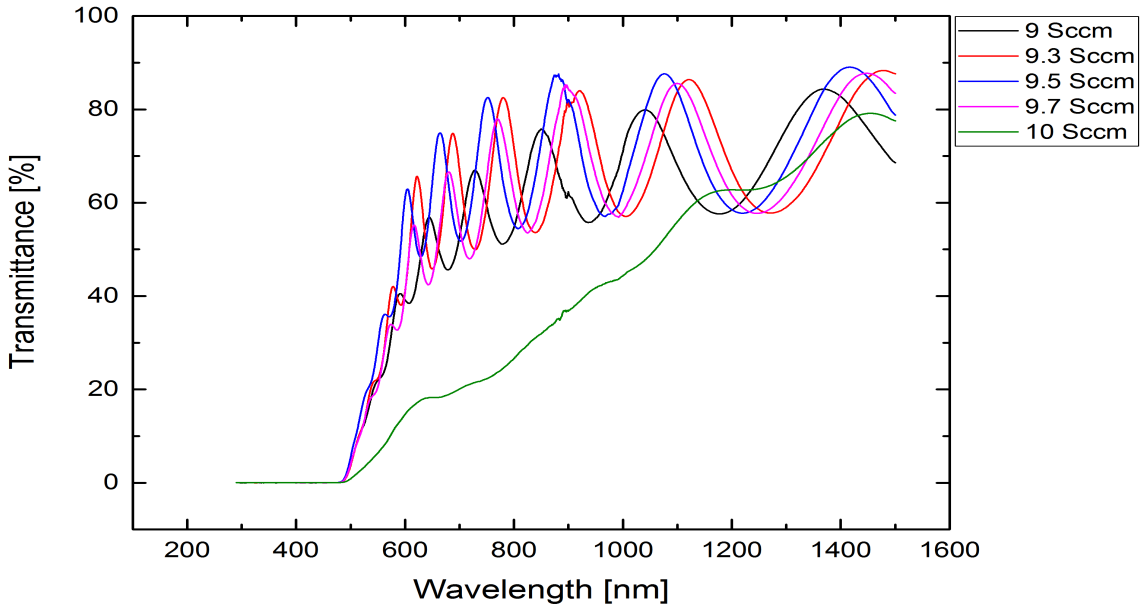

Figure 4.4: Optical transmittance of Cu_2O films deposited on quartz substrates with different J_{O_2}.

4.1.5 Summary and Discussion

In order for Cu_2O to achieve higher efficiencies in solar cells the bulk Cu_2O must be optimized with regard to resistivity, low resisivity is vital in order to conduct mobile carriers to the junction for collection. Additionally for tandem cell application the films should exhibit a high transmission for wavelengths above the band gap.

The optical image shows a clear trend where the samples appearance changes with varying j_{O_2}. This is further confirmed by the XRD data, indicating a shift in phase from $Cu \rightarrow Cu_2O \rightarrow CuO$ with increasing oxygen flows. This agrees well with theory and previous reports, and a close control of oxygen partial pressure during deposition is crucial for good film quality of the desired oxidation state [57]. Further, there is a correlation between the results obtained from the different techniques where the films deposited in the range $9.3 - 9.7\,sccm$ J_{O_2} exhibit the best mobility, lowest resistivity and high transmittance. The high mobility in the samples of $28 \pm 3\,cm^2V^{-1}s^{-1}$ is amongst the highest reported mobilities from sputter deposited Cu_2O thin films, where most reports are in the range $1-10\,cm^2V^{-1}s^{-1}$, with only few reports of films with mobilities $\sim 30\,cm^2V^{-1}s^{-1}$ or above [58, 59, 60, 61, 55].

Sample overview

For the deposition of samples for nitrogen implantation, an oxygen flow of $9.5\,sccm$ was utilized. Four batches were made under these conditions which were used in the following sections. The samples in batches 1-4 were all deposited consecutively. Additionally, a new batch was needed, and thus a fifth batch was made at a later point. The deposition conditions had changed, and instructions suggested samples prepared with same conditions except with an oxygen flow of $7,5\,sccm$ should give similar quality Cu_2O thin films. The characteristics of batch 1 and 5 are compared in the next sections. The process route for the different samples are portrayed in a flowchart presented in Figure 4.5. All samples investigated in the following sections are deposited on quartz substrates.

In the next section follows the effects of post-deposition annealing by RTA. Further, the simulations of implantation profiles are presented followed by the results of three different implanted sample series where the effects on N dopant activation by annealing temperature and time were investigates. Finally, the effect of post deposition annealing on subsequent implantation and dopant activation at the same condition as for the first isothermal series is studied. An overview of the process flow for the different batches follows in Figure 4.5.

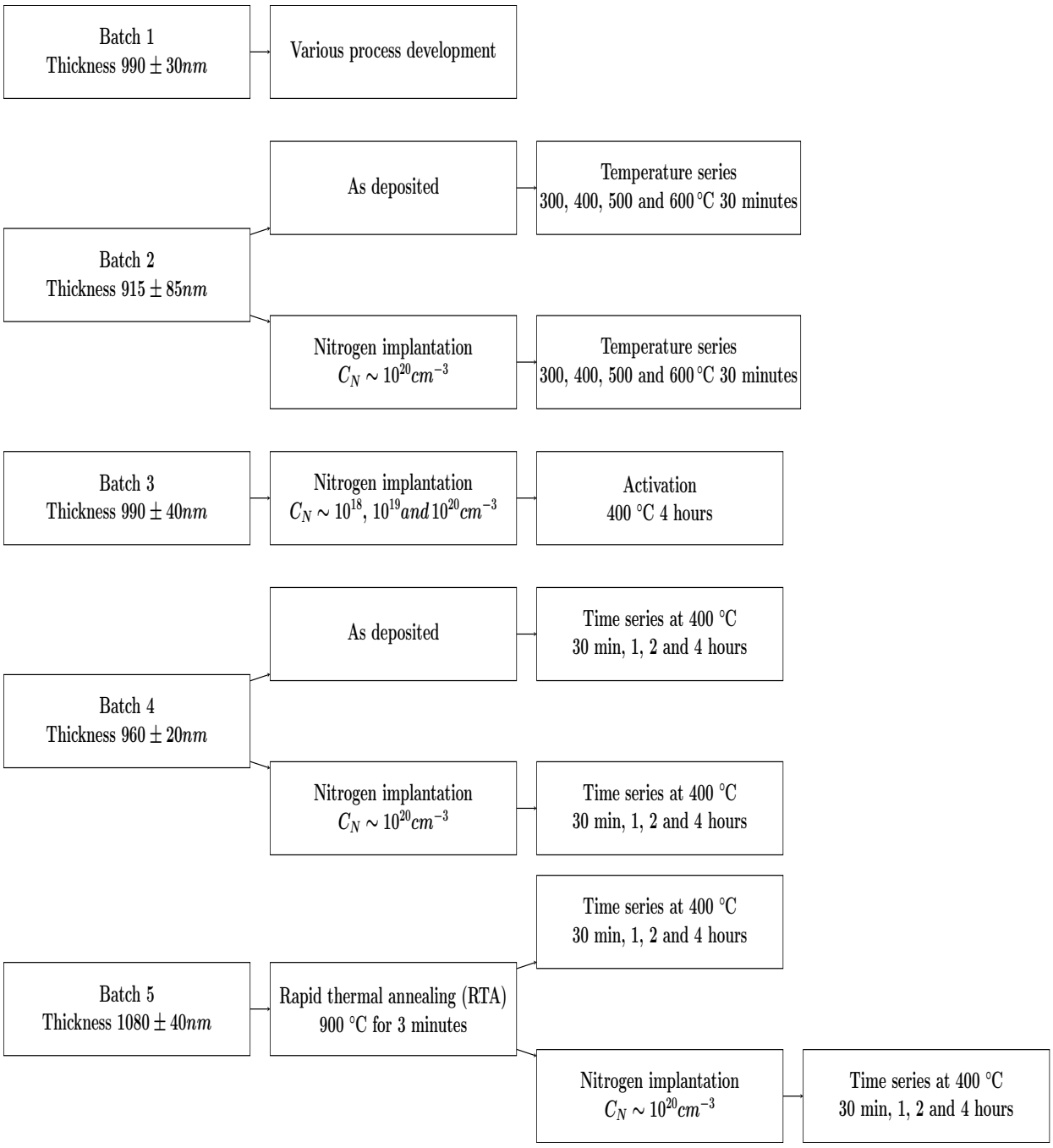

Figure 4.5: Process route of the five Cu_2O thin film batches. After treatment all samples have been characterized with XRD, Hall effect- and transmission measurements.

4.2 Post Deposition Annealing

Post-deposition annealing has proven to significantly increase film crystallinity and carrier mobility [60]. Post-deposition annealing was carried out on selected films to investigate how this interplays with implantation. These films were heat treated using RTA at 900 °C for 3 minutes. The films were investigated by XRD, Hall effect measurements, transmission measurements, and SEM imaging.

One sample from batch 1 were used to test the annealing process, which was later utilized on nearly all samples in batch 5.

4.2.1 XRD Results

In Figure 4.6 one can see that the annealed films have remained phase pure, only diffraction peaks associated with Cu_2O is observed. Further, XRD data show a drastic increase in peak intensity compared to the as-deposited film indicating increased grain size and crystalline quality in the annealed films. Note the different orientation of the two annealed samples, these were both deposited in the same batch and annealed under identical conditions. However, they have an increased intensity in different orientations, where sample 51 is entirely dominated by the (111) peak, while sample 52 has an increased peak intensity in both (111) and (200), where the latter is most dominant. To determine the cause of this evolution is outside the scope of this thesis, and will not be further discussed.

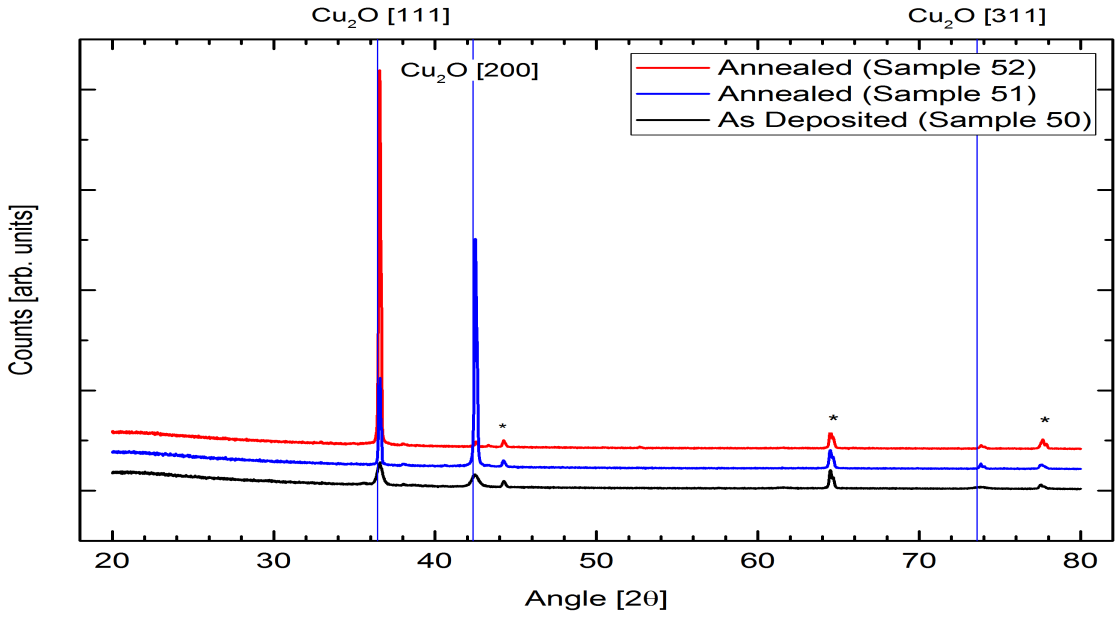

Figure 4.6: XRD results for an as deposited film and films annealed for 5min at 900 °C by RTA (Batch 5). Background peaks are indicated with an asterisk (*).

4.2.2 Hall Effect Measurements

The main goal by post-deposition annealing is to increase the hole mobility of the samples.

The effect of annealing on electrical properties was investigated by Hall effect measurements. The results are presented in Table 4.2. The Hall mobilities increase for both the batch 1 and 5 samples after the annealing process. Additionally, a decrease in carrier density is observed for both samples after annealing. As a result, the overall conductivity is practically unchanged in the samples from batch 1. The as-deposited sample from batch 5 had lower mobility and conductivity compared to batch 1. However, after RTA the mobility is increased up to almost the same value as that in the annealed sample from batch 1.

Table 4.2: Hall measurement data showing resistivity and carrier density and Hall mobility of Cu_2O films from batch 1 and 5 for both as deposited and annealed samples.

Sample	Resisitivty $[\Omega cm]$	Carrier density $[10^{15} cm^{-3}]$	Mobility $[cm^2 V^{-1} s^{-1}]$
Batch 1 - As Dep	167 ± 2	1.2 ± 0.1	32 ± 3
Batch 1 - Annealed	166 ± 2	0.7 ± 0.1	58 ± 6
Batch 5 - As Dep	535 ± 5	0.8 ± 0.1	15 ± 2
Batch 5 - Annealed	316 ± 3	0.4 ± 0.1	53 ± 5

4.2.3 SEM Results

SEM images of the as-deposited and annealed samples are presented in Figure 4.7a and 4.7b. These show that the morphology of the Cu_2O films changes drastically during the RTA process. Extensive grain growth is observed, by the line intersection method an estimated grain size of $\simeq 1 - 2$ micrometer is obtained in the annealed sample, compared to $\simeq$ 50-200 nanometer in the as-deposited sample.

4.2.4 Summary and Discussion

Both the XRD and SEM data indicate that extensive grain growth takes place during the RTA process. In polycrystalline materials, the carrier mobility is limited by crystalline defects and grain boundaries in addition to ionized impurity scattering and lattice vibrations. The increased mobility observed in these samples are likely to be associated with the increased grain size, which reduces grain boundary scattering. Also, scattering centers within the grains may be annealed out as well as reduced ionized impurity scattering due to reduced carrier density. Additionally, a band gap widening and sharpened drop in transmittance near the band gap edge is observed in the transmittance data in Figure 4.18a. Han *et al.* [62] report on reduced hole trapping/de-trapping events, due to a decreased valence band tail (donor-like states) with increasing annealing temperature (500-700 °C), resulting in increased mobility.

The reduced carrier concentrations observed for the RTA-treated samples can probably be attributed to changes in the defect concentrations. Changes in the oxygen stoichiometry as a function

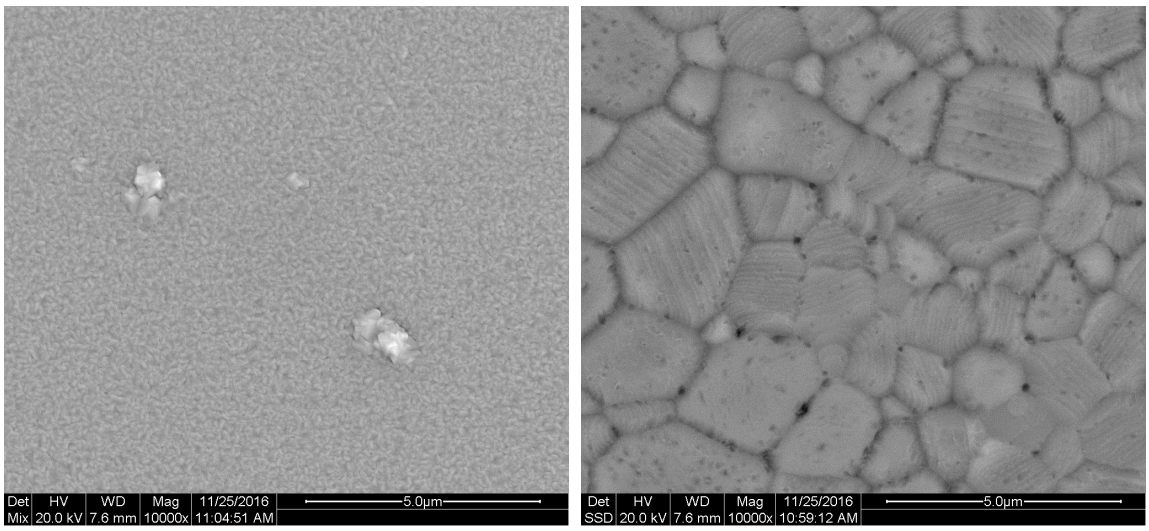

(a) As deposited sample surface. **(b)** RTA treated sample surface.

Figure 4.7: Scanning electron microscopy image of; **a)** an as deposited sample surface and **b)** RTA treated sample surface.

of temperature and O_2 partial pressure during the anneal will promote either V_O or V_{Cu} which will influence carrier concentration. In this case, the stoichiometry is likely to have been shifted in favor of V_O (oxygen deficient) compared to the as-deposited samples, consistent with a reduced net concentration of holes. Finally, Biccari [21] reports that the formation energy of copper vacancies is lower at the grain boundaries in Cu_2O, this could also be a contributing factor to a reduced carrier concentration with increased grain sizes.

4.3 Nitrogen Implantation Simulations

The concentration versus depth distributions of implanted nitrogen ions in Cu_2O are simulated using the SRIM software [44]. To achieve an even distribution of nitrogen in a $\simeq 350nm$ thick layer, a box implant was constructed by simulating three different implantation energies, 20, 65 and $130keV$. In the simulations nitrogen was implanted in a $500nm$ layer of Cu_2O with a density of $6.0g/cm^3$. In Figure 4.8a, the simulated normalized ion distribution are plotted together with the total distribution for the three energies combined. Further, the calculated distributions were weighted with different implantation doses to achieve a uniform nitrogen concentration throughout the desired range; these results are plotted in Figure 4.8b. The estimated doses to achieve this distribution with an average nitrogen concentration of $\simeq 10^{20}cm^{-3}$ were found to be $\phi_{130keV} = 5,4 \times 10^{15}\, cm^{-2}$, $\phi_{65keV} = 1,3 \times 10^{15}\, cm^{-2}$ and $\phi_{20keV} = 2,4 \times 10^{14}\, cm^{-2}$.

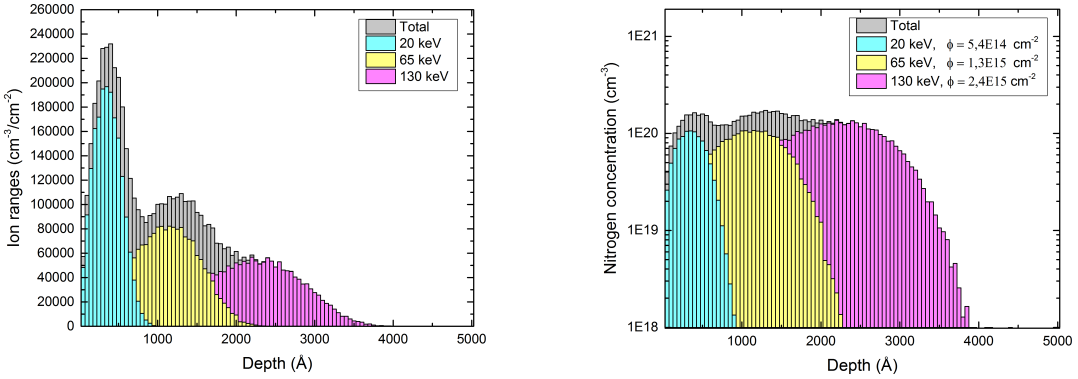

(a) **(b)**

Figure 4.8: **a)** Normalized concentration versus depth distribution for nitrogen implanted in Cu_2O at $135keV$, $65keV$, $20keV$ and total distribution obtained from SRIM Monte Carlo simulations. **b)** The calculated nitrogen concentration versus depth after implantation at 130, 65, $20keV$ and total concentration with doses $\phi_{130keV} = 5,4 \times 10^{15}\, cm^{-2}$, $\phi_{65keV} = 1,3 \times 10^{15}\, cm^{-2}$ and $\phi_{20keV} = 2,4 \times 10^{14}\, cm^{-2}$.

4.4 Isochronal Post-Implant Annealing

After implantation there generally is a high concentration of defects and dislocations due to implantation-induced damage. To remove this damage such that the structural integrity of Cu_2O is restored, post-implantation annealing was employed. Additionally, by increasing the temperature diffusion of nitrogen will increase and it can more easily occupy energetically favorable positions in the lattice. In particular, if nitrogen substitutes oxygen, it will behave as an acceptor, thus contribute to the hole concentration in the Cu_2O films.

The annealing was performed in a Semicore TriAxis magnetron sputtering chamber where the heating system is limited to $600\,^{\circ}\mathrm{C}$. In this first approach, a temperature series was employed where the samples were annealed under a base pressure of $2 \times 10^{-6} Torr$ for 30 minutes. The results of samples annealed at 300, 400, 500 and $600\,^{\circ}\mathrm{C}$ were investigated. Initially, a sample was annealed at $200\,^{\circ}\mathrm{C}$, however, no change was detected by XRD or four point probe measurement. Therefore, the same sample was annealed further at $300\,^{\circ}\mathrm{C}$ to expand the temperature range.

Annealing was attempted at higher temperatures in the RTA system, however all attempts resulted in samples with metallic copper phase present. The vacuum pump used for the RTA system could only reduce the pressure to the order of 10^{-1} Torr, which works well for higher temperatures, such as $900\,^{\circ}\mathrm{C}$ used in a previous section. However, for the temperatures of $600 - 800\,^{\circ}\mathrm{C}$ this would result in CuO phases in the films. Therefore, a high-capacity pump was installed, but this resulted in a too low pressure on the order of 10^{-3} Torr, giving rise to metallic copper phase in the samples. The XRD results of undoped samples annealed at 600, 700 and $800\,^{\circ}\mathrm{C}$ at a pressure of $\sim 10^{-3} Torr$ is included in Appendix A.

The samples in this section are referred to as N20_(Anneal temperature), e.g., N20_300 for the implanted samples and simply annealing temperature, e.g., 300, for the undoped samples.

4.4.1 XRD

The full spectra in this and following sections all show phase pure Cu_2O. To obtain a detailed look at the peaks which are of prime interest, the data are plotted for the 2θ angles in the range $35 - 44^o$. Both the $Cu_2O(111)$ and $Cu_2O(200)$ peak are present in this region.

The XRD results of the isochronal series are presented in Figure 4.9. The as-implanted samples have a reduced peak intensity for both the $Cu_2O(111)$ and $Cu_2O(200)$ peaks compared to the as-deposited samples, likely due to the damage sustained during implantation. A clear trend is observed that with increased annealing temperature, the implanted samples crystalline integrity is restored until eventually they approximately coincide with the undoped samples at the higher temperatures of 500 and $600\,°\mathrm{C}$. Finally, a shift towards lower 2θ is observed for the (200) peak of sample N20_400.

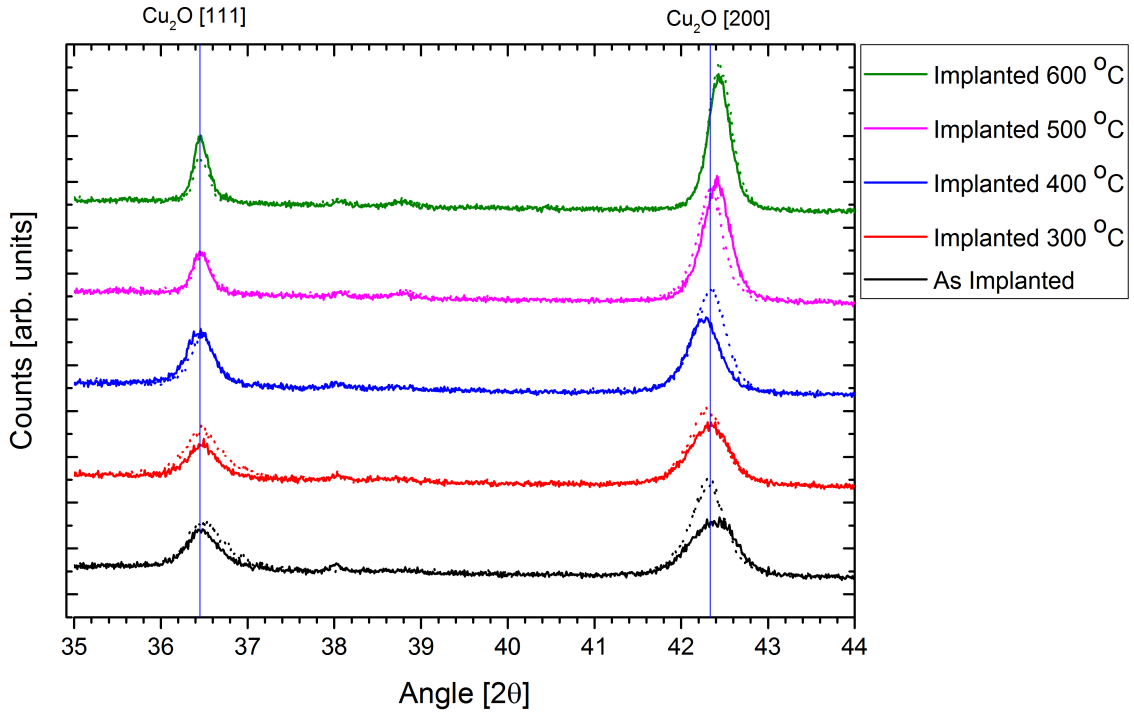

Figure 4.9: XRD results for Cu_2O and $Cu_2O:N$ films. The solid lines are $Cu_2O:N$ films and the dotted lines are undoped Cu_2O films, both annealed for 0.5h at the given temperatures.

4.4.2 Hall Effect Measurement Results

Hall effect measurements have been performed to investigate the effect of annealing temperature on carrier concentration, mobility, and resistivity. Additionally, measurements have also been done on undoped films to distinguish between the effects of the heat treatment in itself and the presence of nitrogen in the samples.

The full thickness of the samples are used both for the undoped and implanted sample. Despite the fact that if the implanted layer has much a lower resistivity compared to the bulk, the majority of the current will flow in this layer. Therefore, by using the full thickness the values extracted from the implanted samples might be shifted according to the implanted layer width. Anyhow, the trends retrieved by the full film width should still be valid.

In Figure 4.10a, the result for the undoped samples are presented, it appears that the mobility in the samples increases with increasing annealing temperature. The carrier concentration seems to be more or less unchanged throughout the series. In the implanted sample little change is observed for sample N20_300. However, for samples N20_400 and N20_500 the carrier concentration increases and for sample N20_600, it decreases. Figure 4.10c shows the difference in carrier concentration versus annealing temperature for the undoped and implanted samples, an increase is clearly observed for samples N20_400, N20_500, and N20_600, with a maximum in sample N20_500.

4.4.3 Transmission Results

The transmission measurement spectra show a general trend where higher annealing temperature results in increased transmittance for both the implanted and undoped films, corroborating an improved crystalline quality. Additionally, an optical band gap widening with increasing temperature up to 2.52 eV are observed for both the undoped and implanted samples.

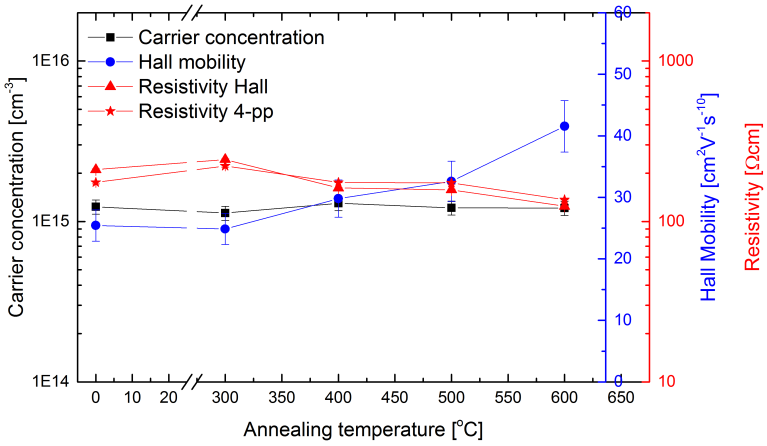

(a) Undoped samples

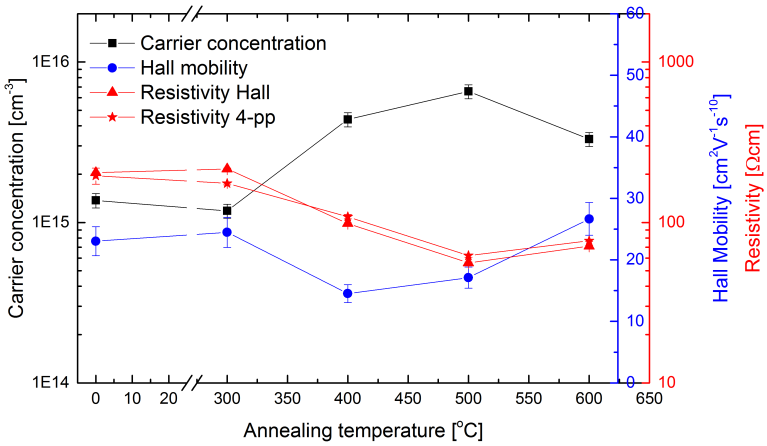

(b) Implanted samples

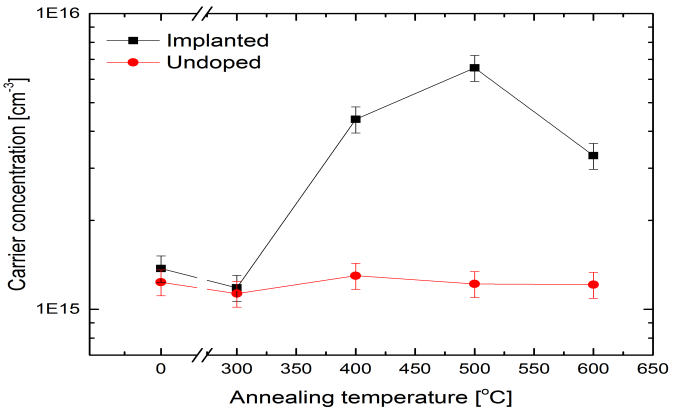

(c) Comparison of carrier concentration for implanted and undoped samples.

Figure 4.10: Resistivity measured with both Four-point probe and Van der Pauw, together with carrier concentration and Hall mobility from Hall effect measurements, plotted as a function of annealing temperature.

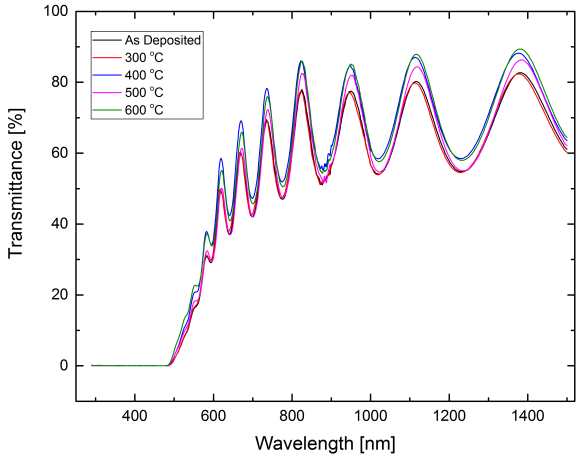

(a) Transmittance of undoped samples

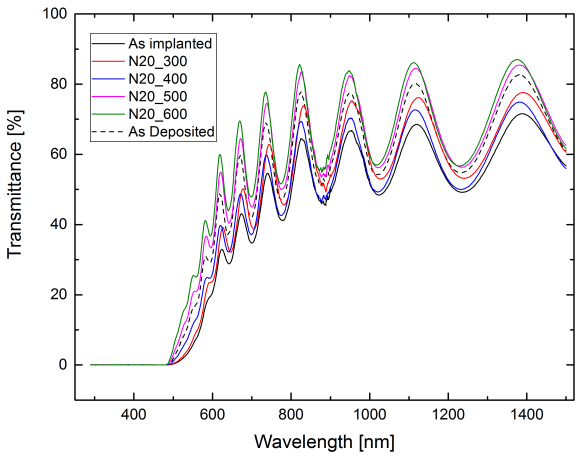

(b) Transmittance of implanted samples

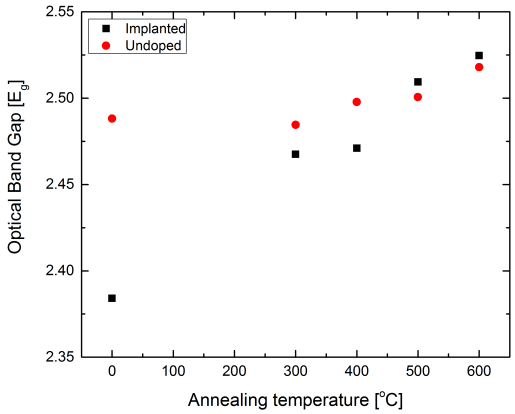

(c) Comparisson of Eg extracted from tauc plots for implanted and undoped samples.

Figure 4.11: a) Optical transmittance of implanted Cu_2O samples annealed for 0.5h at the given temperatures. **b)** Tauc plots and the extrapolated optical band gap energies.

4.4.4 SIMS Results

SIMS was employed to investigate the nitrogen content in the samples after implantation and subsequent annealing. The SIMS data exhibit good agreement with the simulations exercised in Section 4.3 and show that the implantation was successful. Further, the nitrogen content in the samples N20_300 and N20_400 seems to remain unchanged. At $600\,°C$, a slight reduction and signs of out-diffusion are observed. Aforementioned is in agreement with Li *et al.* [59] who report on out-diffusion of nitrogen at temperatures of 650, 750 and $800\,°C$ after only 10 minutes. A slight shift is also observed in sample N20_500.

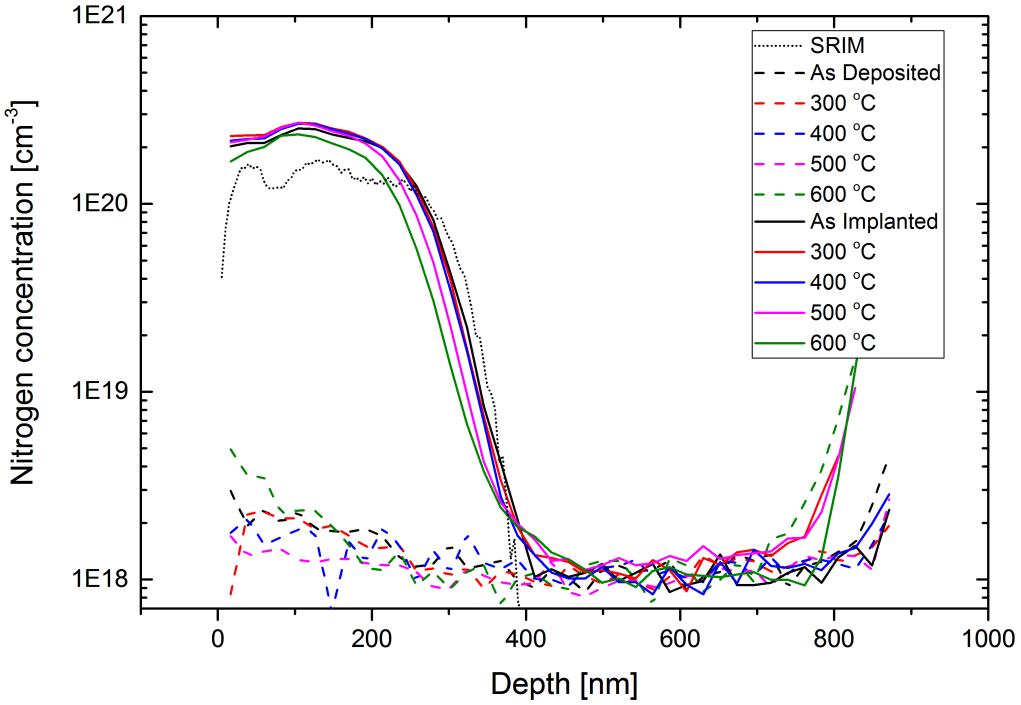

Figure 4.12: SIMS results for undoped Cu_2O and implanted $Cu_2O:N$ films ($N \simeq 10^{20} cm^{-3}$). The solid lines are $Cu_2O:N$ films and the dashed lines are undoped Cu_2O films, both annealed for 30 min at the given temperatures. The dotted line is the nitrogen concentration as predicted by SRIM calculations.

4.4.5 Summary and Discussion

The isochronal annealing series reveals that the crystallinity of the films improves with annealing temperature. As a result, the mobility also increases, in agreement with the results from Section 4.2. Further, there is a clear difference between the undoped and doped samples regarding carrier concentrations, transmission, and SIMS results. The implanted samples have some initial reduction in transmission and XRD intensities compared to the undoped film. This difference is likely a consequence of the damage sustained during implantation. With increasing annealing temperature

much of the differences disappears, and for the temperature of 500 and $600\,^{\circ}\mathrm{C}$ both XRD and transmission data coincide with that of the undoped films.

Hall effect measurements show an increased carrier concentration in the implanted samples compared to the undoped ones. An indication is obtained that nitrogen successfully has been incorporated as an active acceptor in the Cu_2O films annealed at $400\,^{\circ}\mathrm{C}$ and above (Figure 4.10c). A peak concentration of about $2 \times 10^{20} cm^{-3}$ is detected by SIMS. Further, an increased carrier concentration of $\sim 1 \times 10^{16} cm^{-3}$ is observed in the implanted films. Possible raewsons for the poor degree of electrical activation of the implanted N ions will be discussed in Section 4.9.

The SIMS results and the findings by Li *et al.* [59] suggest that nitrogen diffuse out of the samples at elevated temperatures. This makes RTA processes at high temperatures like $900\,^{\circ}\mathrm{C}$ destructive with the respect of achieving high carrier concentrations through nitrogen doping. However, by implantation, doping can be incorporated after RTA treatment and thus benefit from the increased crystal quality and carrier mobility. With this in mind, the annealing temperature of $400\,^{\circ}\mathrm{C}$ is chosen for the next series where the effect of isothermal annealing are investigated. At $400\,^{\circ}\mathrm{C}$ an increased XRD intensity occurs, in addition to a shift towards higher inter-planar distances, which could be an indication of nitrogen in the crystal lattice (nitrogen has a larger atomic radii than oxygen). As well as the improved transmittance compared to the as-implanted sample, in addition to an increased carrier concentration. Finally, no signs of out-diffusion are detected, which may suggest that no nitrogen will be lost at longer annealing times. The structural, optical and electrical data suggest that a temperature of $400\,^{\circ}\mathrm{C}$ is sufficient to anneal out the majority of implantation-induced damage, and possibly electrically activate nitrogen as an acceptor in the films.

4.5 Isothermal Post-Implant Annealing

In this section, the effect of annealing time is studied. The same conditions as in the temperature series were utilized, except that the temperature was kept at $400\,^{\circ}\mathrm{C}$ while different annealing durations of 0.5h, 1h, 2h and 4h were employed.

The samples in this section are referred to as N20_(Anneal time), e.g., N20_0.5h for the implanted samples and simply annealing time, e.g., 0.5h, for the undoped samples.

4.5.1 XRD

The XRD results show that despite the increased annealing time, no traces of CuO or Cu are present. From the pattern presented in Figure 4.13 it is observed that sample N20 (as implanted) has a reduced peak intensity due to the implantation-induced damage. However, after 0.5h at $400\,^{\circ}\mathrm{C}$ the intensity increases, indicating an improved crystal structure. At $400\,^{\circ}\mathrm{C}$ the crystallinity of the films does not increase further after the initial 30 minutes, as neither the implanted or deposited films show any significant changes in XRD spectra with increasing annealing times beyond 0.5h.

The deviation of the spectrum in sample 0.5h is believed to be an individual non-representative feature and is not considered in further detail. This is also based on the data from the sample annealed at $400\,^{\circ}\mathrm{C}$ in the isochronal series which had the same treatment and does not show the same reduction in peak intensity.

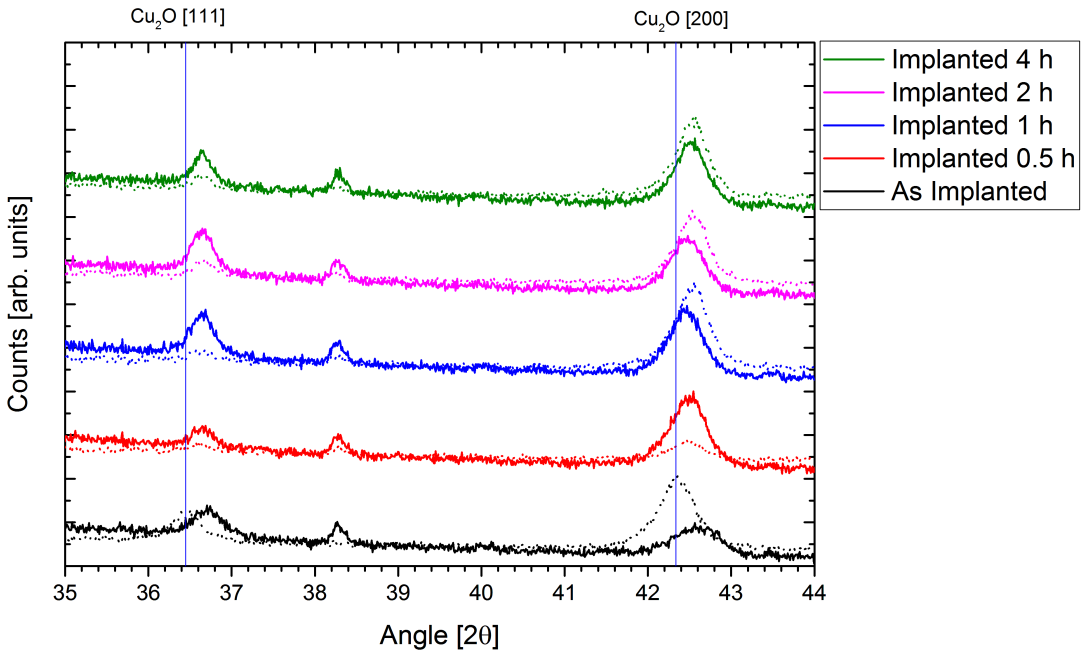

Figure 4.13: XRD results for Cu_2O and $Cu_2O : N$ films. The solid lines are $Cu_2O : N$ films and the dotted lines are Cu_2O with the same treatment for reference. All samples were annealed at $400\,°\mathrm{C}$ for the duration stated in the legend.

4.5.2 Hall Effect Measurement Results

Hall effect measurements have been conducted to investigate how the electrical properties are affected by the increased annealing times. In Figure 4.14 the samples resistivity, Hall mobility, and carrier concentration are plotted versus the annealing time. A comparison between the carrier concentrations of the implanted and undoped samples are given in Figure 4.14c. The results from the XRD analysis are reflected by the unchanged mobility, indicating little change in the structure of the sample at this temperature. However, a clear picture is seen regarding carrier concentration, an increase is observed throughout the whole series for the implanted samples. It seems to reach a saturation after 2 h where only a slight increase is seen after 4h. The undoped samples remain more or less unchanged throughout the series. Also for this series the comparison of the implanted and undoped films indicate an increased ionized acceptor concentration.

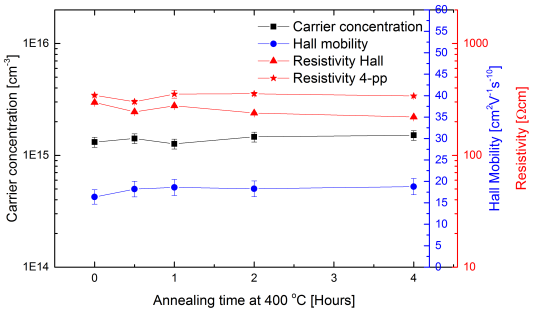

(a) Undoped samples

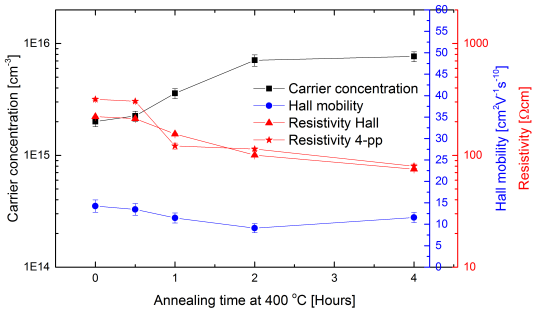

(b) Implanted samples

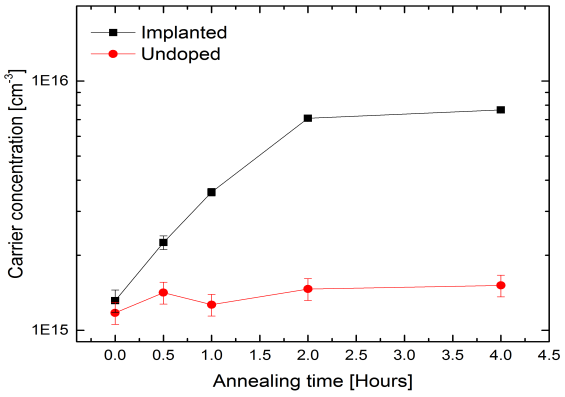

(c) Comparisson of carrier concentration for implanted and undoped samples.

Figure 4.14: Resisitivity measured with both Four-point probe and Hall Effect, carrier concentration and Hall mobility plotted as a function of annealing time.

4.5.3 Transmission Results

The transmission results in Figure 4.15 show a similar picture as obtained from the XRD analysis; the samples exhibit similar transmittance spectra after the initial 0.5h anneal compared to the as-implanted sample. Initially, some transmittance is lost due to implantation-induced damage, but some of this is restored after 30 minutes annealing and does not improve further with longer annealing times. The undoped films spectra more or less overlap for all anneal times.

The Tauc plot analysis does, however, show a different story. There appears to be an optical band gap narrowing by the implantation, followed by widening with increasing annealing time, going from 2.40 eV up to 2.49 eV for the sample annealed for 4 hours. The undoped samples are scattered without any apparent trend around an optical band gap of 2.5 eV.

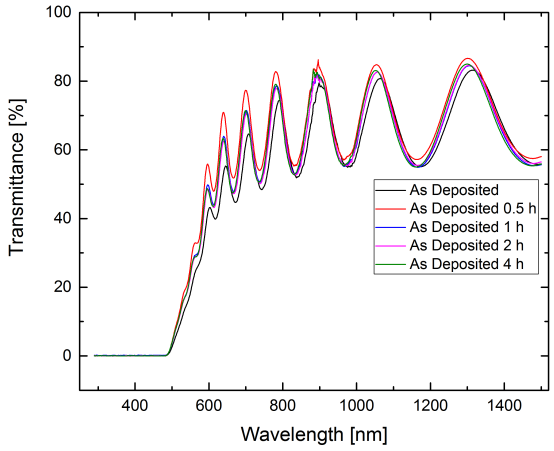

(a) Transmittance of the undoped samples.

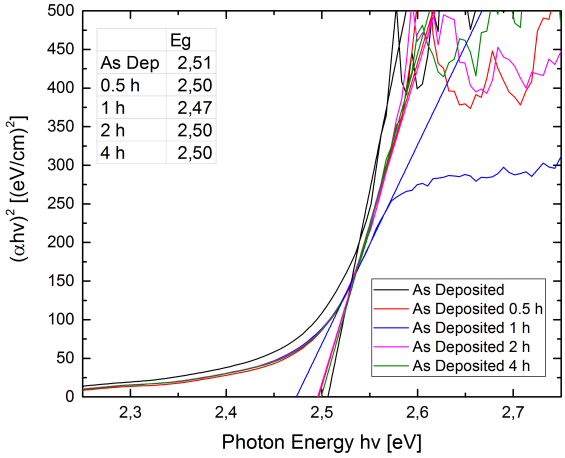

(b) Tauc plot for undoped samples.

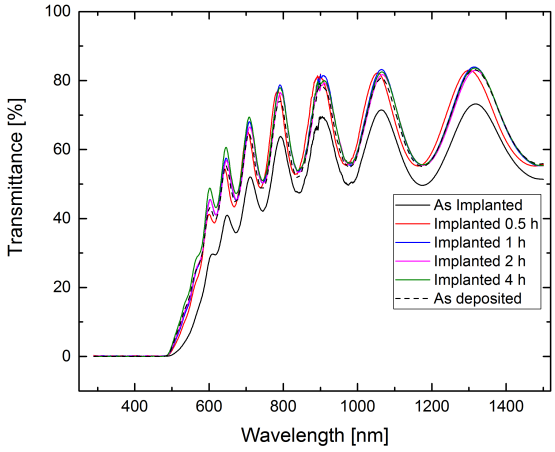

(c) Transmittance of the implanted samples.

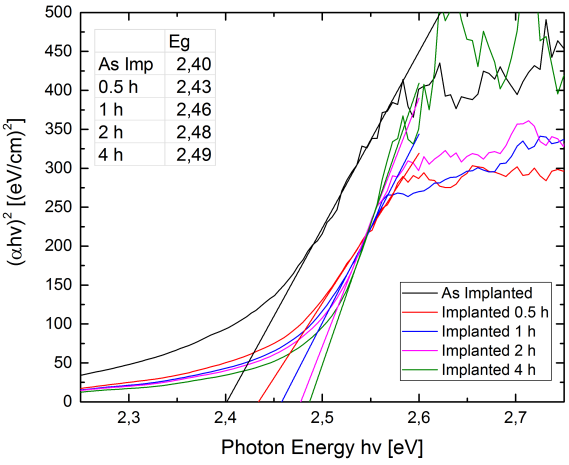

(d) Tauc plot of the implanted samples.

Figure 4.15: Transmittance and Tauc plots of the isothermal annealed samples.

4.5.4 Summary

The above results show that annealing at $400\,^{\circ}\mathrm{C}$ does reduce some of the implantation-induced damage. After 0.5h much of the structural damage is annealed out which is evidenced both through improved XRD and transmission spectra. Further, the electrical activation of nitrogen seems to increase throughout the series. However, a saturation occurs after 2 hours, with a slight further increase at extended annealing times.

To make sure proper activation and proper anneal conditions had been found two additional anneals were performed. First, to conclude that the saturation after 2h anneal is valid an additional set of samples was annealed overnight for 16 hours as a control. Four point probe measurements of these samples revealed a higher resistivity compared to those annealed at 2-4 hours, presumably due to out-diffusion (loss) of N. Finally, to make sure the temperature is high enough for proper activation another annealing was done at $500\,^{\circ}\mathrm{C}$ for 2 hours, and indeed, here similar resistivity as for the samples annealed at $400\,^{\circ}\mathrm{C}$ for 2-4 hours was found by four-point probe measurements. The results are given in Appendix C.

4.6 Concentration Series

A series of samples were prepared and implanted with three different doses aiming for nitrogen concentrations of $\sim 10^{18}cm^{-3}$, $\sim 10^{19}cm^{-3}$ and $\sim 10^{20}cm^{-3}$. Three samples were characterized as implanted and three samples were annealed at $400\,^{\circ}\mathrm{C}$ for 4 hours which has proven effective in the previous section. The characterization methods utilized where XRD, transmission and Hall effect measurements. The XRD patterns of the samples give an indication that higher implantation doses results in a more damaged crystal. After annealing the crystallinity seems to be restored, the same trend is observed in the transmission data. However, from the Hall effect measurement no clear indication of any change is observed.

The sample which had been doped with the highest dose of $\sim 10^{20}cm^{-3}$ and subsequently annealed at $400\,^{\circ}\mathrm{C}$ for 4 hours were measured with SIMS. When comparing this sample to the other implanted samples it seems clear that something failed. No traces of nitrogen from the implantation is detected. Therefore the results and discussion of this sample series has been excluded from the thesis. However, the data from XRD, Hall, transmission and SIMS measurements are presented in Appendix B. It can be speculated that some other light element than N was implanted but this remains to be confirmed.

4.7 Post Deposition Annealed Series

The final series investigated are samples which after deposition were treated by RTA at $900\,^{\circ}\mathrm{C}$ for 3 minutes before implantation. The effect of the RTA process is discussed in Section 4.2. In this section, the effect of implantation is reported for post-implantation annealing at $400\,^{\circ}\mathrm{C}$ with durations of 0.5, 1, 2 and 4 hours. To clarify, all samples in this section was treated by RTA prior to implantation. However, when referring to annealing in this section, it is to the post-implantation annealing and not the post-deposition RTA treatment of the samples.

The samples in this sections are labeled RTA_N20_(time) for the implanted samples and RTA_(time) for the undoped samples.

4.7.1 XRD

Under the course of collection of XRD spectra from the sample series, maintenance was performed on the XRD system, with a realignment of the detector. Therefore, the data collected after maintenance give a much stronger signal. All undoped samples (dotted lines) were measured before the maintenance and the implanted samples (lines) after. The data plotted in Figure 4.16 are normalized within each dataset for comparison at the same scale, mind that this makes the relative intensities within each dataset comparable but not between the two.

The XRD data in this section have a much stronger peak intensity due to the increased crystalline quality after RTA. As a result, the shift in peak positions is more clear, a shift to lower 2θ values is observed for all the implanted samples after annealing at the time intervals investigated. The same inconsistency between preferred orientation is observed here as for the annealed samples in section 4.2, where two samples show mixed orientation and two have a clear preference in the (111) direction. Finally, an annealing time of 30 minutes causes the diffraction peaks to sharpen, indicating restoration of the crystal structure and annealing of the implantation-induced damage.

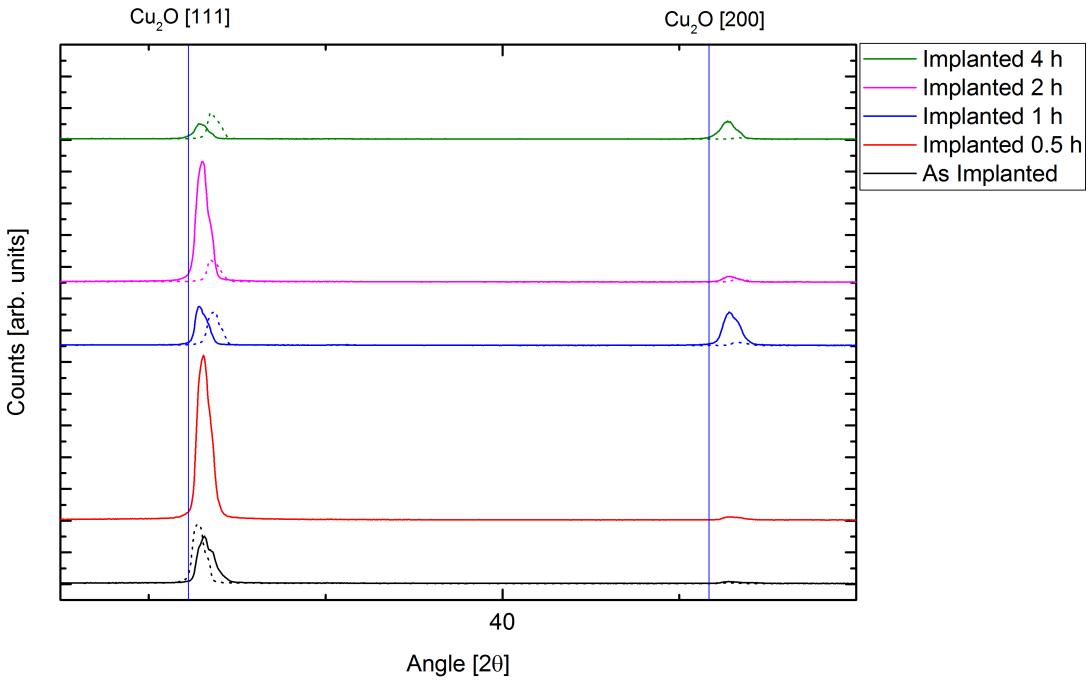

Figure 4.16: XRD results for Cu_2O and $Cu_2O : N$ films. The solid lines are $Cu_2O : N$ films and the dotted lines are Cu_2O with the same treatment for reference. All samples are annealed at $400\,°\mathrm{C}$ for the duration stated in the legend.

4.7.2 Hall Effect Measurement Results

The as-implanted sample exhibits strongly reduced hole mobility compared to the undoped sample, down from $53 \pm 5\,cm^2V^{-1}s^{-1}$ to only $4 \pm 1\,cm^2V^{-1}s^{-1}$ after implantation. An interesting trend in the carrier concentration is observed compared to the time series in the previous section. Here, there is initially a decline in the carrier concentration, before it starts to increase after 2 hours. The mobility increases with time before at 4 hours a big increase in the carrier concentration is achieved followed by a slightly lower mobility. In the undoped samples the carrier concentration once again remains nearly unchanged, however, a decrease is observed for the mobility at these annealing conditions.

The comparison between carrier concentrations in Figure 4.17c shows that an increased carrier concentration occurs after 4 hours annealing or more at $400\,°\mathrm{C}$ for the implanted sample. However, it remains unchanged in the undoped samples and is about a factor of 35 lower than in the implanted sample annealed at $400\,°\mathrm{C}$ for 4h. Additionally, a decrease is observed for the mobility in the undoped samples after annealing at all time intervals.

The result for the films annealed for 4 hours show the best qualities in this study, its high mobility of $29 \pm 3\,cm^2V^{-1}s^{-1}$ compared to the previous series and carrier concentration of $8 \pm 1 \times 10^{15}cm^{-3}$ sets it apart with a resistivity of $29 \pm 1\Omega cm$.

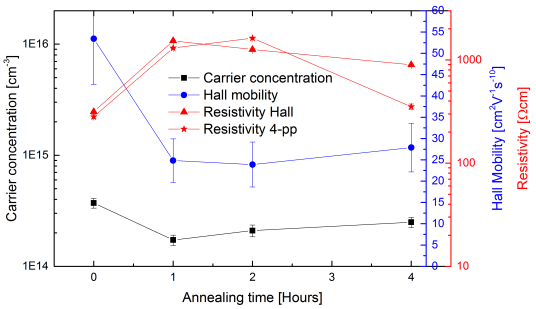

(a) Undoped samples

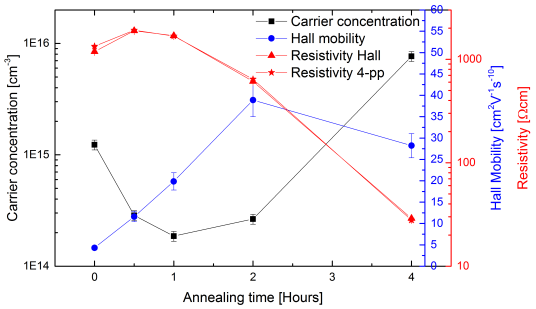

(b) Implanted samples

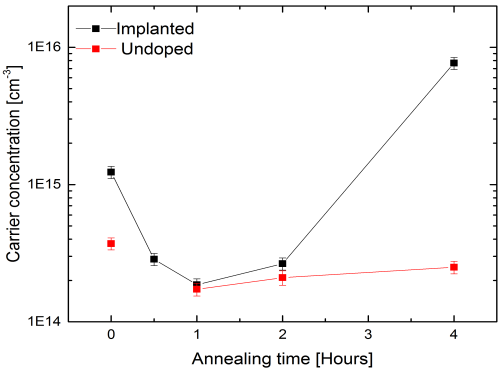

(c) Comparisson of carrier concentration for implanted and undoped samples.

Figure 4.17: Resisitivity measured with both Four-point probe and Hall Effect, carrier concentration and Hall mobility plotted as a function of annealing time at 400 °C. All samples here are treated with RTA process at 900 °C for 3 minutes prior to annealing or implantation plus annealing.

4.7.3 Transmission Results

The transmission measurements show that the transmission increases with increasing annealing time in the implanted samples, unlike the undoped samples which show similar spectra for all annealing times; Figure 4.18. Additionally, an increased band gap is observed for the implanted samples with time. Also, the band gap remains unchanged in the undoped samples.

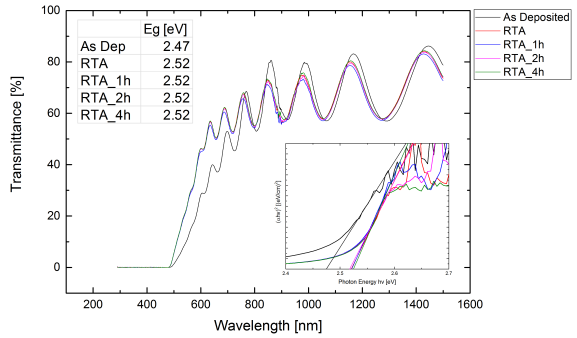

(a) Undoped samples

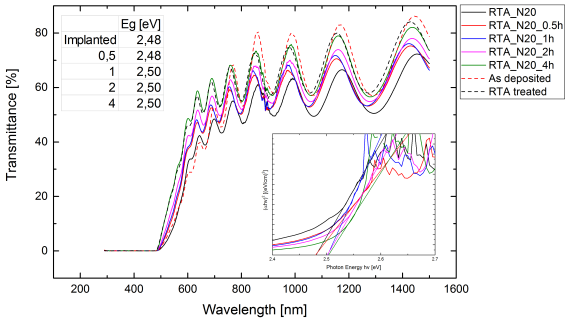

(b) Implanted samples

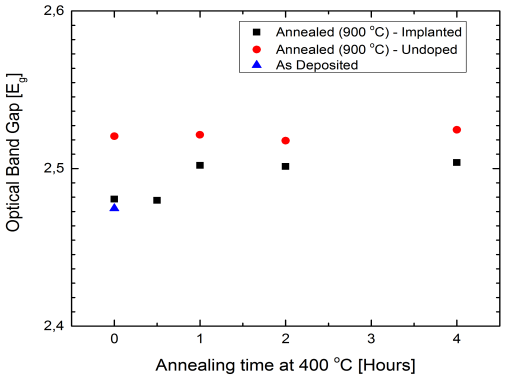

(c) Comparisson of Eg for Implanted and undoped samples.

Figure 4.18: Transmittance and with inserted Tauc plots of the isothermal annealed samples which has. All samples here are treated with RTA process at 900 °C for 3 minutes prior to annealing or implantation plus annealing at 400 °C.

4.7.4 SIMS Results

The SIMS results in Figure 4.19 show that annealing at 400 °C does not promote substantial out-diffuission or re-distribution for annealing times up to 4 hours.

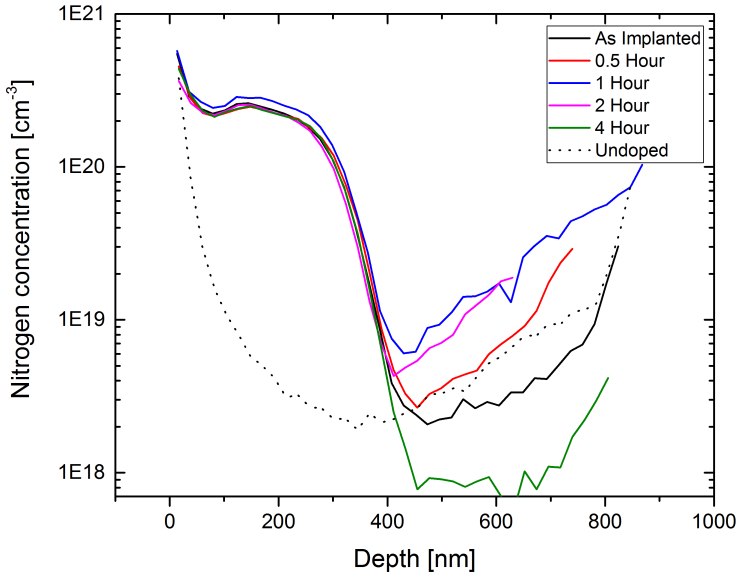

Figure 4.19: SIMS results for post-implantation annealed samples for 0.5, 1, 2 and 4 hours at $400\,^{\circ}\mathrm{C}$. The dashed line are the result of an undoped Cu_2O film annealed for 4 hours.

4.7.5 Summary and Discussion

By combining the information from the XRD, Hall- and transmission measurements, it appears that the N implantation gives rise to crystal damage and defects reducing the hole concentration, which require extended annealing duration at $400\,^{\circ}\mathrm{C}$ before the influence disappears. The decrease in hole concentration (reverse annealing) until 1h of annealing implies that thermally activated evolution of defects takes place, leading to compensation and/or passivation of the dominant shallow acceptors in the films (presumably V_Cu and N_O). The continuous increase in mobility combined with the increased transmission corroborate the improved crystallinity with time and possibly also gradual activation of N as a shallow acceptor (N_O) in the Cu_2O films.

4.8 Temperature Dependent Hall Effect Measurements

Temperature dependent Hall (TDH) measurements have been conducted on the samples asdep_4, N20_4h, RTP_4h and RTP_N20_4h. RTP_N20_4h and N20_4h are the samples with lowest resistivity of the ones prepared, with and without RTP treatment respectively.

The hole mobility in the samples treated with RTA and those without have different characteristics. The samples which have undergone RTA have a continuous reduction in mobility with higher measurement temperatures. This could be a result of the increased crystallinity and grain size, hence impurity scattering is non-dominant in the temperature interval probed. Sample asdep_4h and N20_4h show mobility data that resemble a textbook example, Figure 4.20, indicating that two or more scattering mechanism dominate at their respective temperature intervals. Because

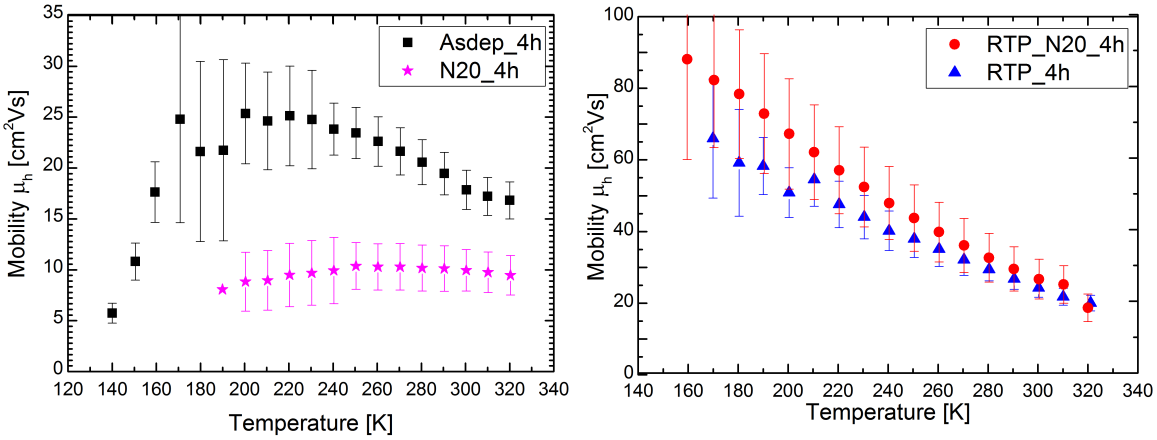

Figure 4.20: Temperature dependence of the Hall mobility determined by temperature dependent hall measurements.

of this difference between the two sample sets, it is tempting to attribute the dominating scattering mechanism to grain boundary scattering at lower temperatures and lattice scattering at higher temperatures in these samples.

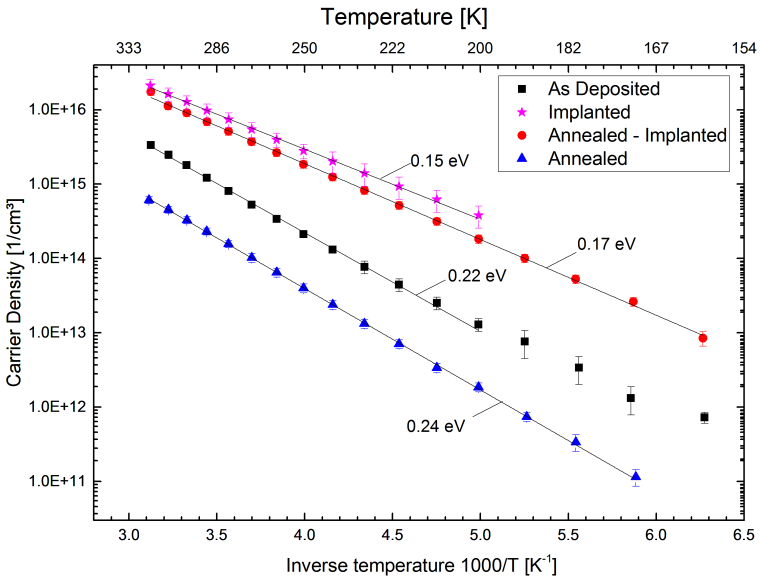

Figure 4.21: Temperature dependence of hole density determined by temperature dependent hall measurements. Activation energies E_A is estimated from the slope indicated by a black line.

The activation energy of dominant acceptors is deduced for the four samples. A decrease in activation energy is observed for both the implanted samples compared with the undoped ones. The activation energy is found to be 240 meV in sample RTP_4h and 170 meV for RTP_N20_4h. A similar reduction in activation energy is observed for other samples with 220 meV in asdep_4h and 150 meV in N20_4h. The activation energies in the implanted samples are lower than those reported for the intrinsic V_Cu defect where experimental and theoretical estimates are in the range of 180-300 meV [32, 21, 15]. Our values of 170 and 150 meV are somewhat higher than those in previous reports for N_O, around 120 meV [59, 15]. However, they are clearly distinguishable from the values in the undoped samples, with a significant drop of about 70 meV in both the implanted samples compared to the undoped. This is a clear indication that nitrogen successfully has been incorporated with an acceptor level shallower than that of the V_Cu.

The measured data in Figure 4.21 only reveal one clear acceptor level (one slope) in the different samples and no signs of the "extrinsic" region as portrayed in Figure 2.8 was detected. Therefore, the acceptor concentration N_a cannot be firmly established. However, an estimation of a theoretical lower limit of the acceptor concentration which still are in agreement with the experimental data may be extracted. The results of the fit and extrapolated "extrinsic" region are displayed in Figure 4.22. The extracted concentrations of sample RTA_N20_4h and RTA_4h are found to be $\sim 10^{18}cm^{-3}$ and $\sim 10^{16}cm^{-3}$ respectively. For samples N20_4h and asdep_4h, we find $\sim 10^{19}cm^{-3}$ and $\sim 10^{18}cm^{-3}$ respectively. These results evidences that a higher acceptor concentration is present in the implanted samples compared to the undoped samples, supporting the claim of successfully increasing the acceptor concentration in the samples.

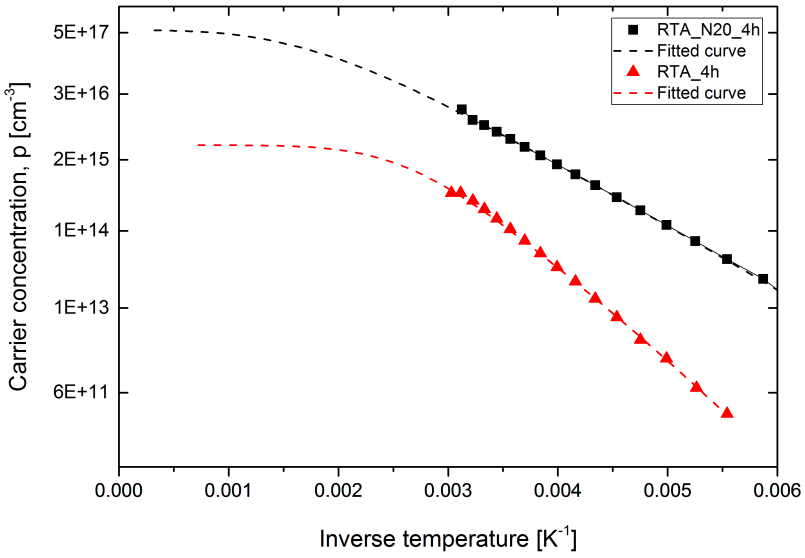

Figure 4.22: The natural logarithm versus inverse temperature is plotted for the RTA samples. The dashed line is an extrapolated estimate to determine the lower limit acceptor concentration from a theoretical "extrinsic" region which still is in agreement with the experimental results.

4.9 Discussion of Nitrogen Implantation

From the above results it seems likely that nitrogen does substitute oxygen and act as an acceptor in the films after annealing. Increased carrier concentration is obtained in all the implanted samples after annealing. This is in agreement with Li *et al.* [59] which reports on increased carrier concentrations and reduced N_i signature in photoluminescence spectroscopy with increasing annealing temperature. This is likely due to the increased nitrogen diffusivity and crystal recovery at higher temperatures, enabling N to occupy vacant substitutional oxygen sites and act as a shallow acceptor.

The recorded carrier concentration in the samples are considerably lower than that expected with a nitrogen doping concentration of $\sim 10^{20}\,cm^{-3}$ and full activation. The exact reason for this is hard to pin point with the techniques employed, however, possible contributing factors are discussed. Firstly, the Hall effect measurements are as earlier stated deduced by using the full film width. This may yield lower carrier concentrations for the implanted layer if the majority of the current flows in there. However, the implanted layers is $\sim$ 1/3 of the film width, so the resulting difference in carrier concentration in the implanted layer should not be much more than a factor of ~ 3. Figure 4.23 shows a plot of the carrier concentration (ionized N_O concentration) versus temperature for four different chemical N_O concentrations, assuming an activation energy of 170 meV. The results in Figure 4.23 are obtained from the charge neutrality equation, which is solved numerically yielding the Fermi-level position and hence the fraction of ionized N_O acceptors. The extracted activation energies in this thesis are higher than in earlier reports (170 meV versus 120 meV) resulting in a lower degree of ionization in the samples. However, as seen in Figure 4.23, an activation energy of 170 meV should result in about $\sim 10^{18} cm^{-3}$ carriers at 300 K if all the nitrogen ($\sim 10^{20}\,cm^{-3}$) was substituting for oxygen. This tells us a few things; we could be dealing with a highly compensated material, or the incorporation of nitrogen into oxygen sites (N_O) is low, or a combination of the two could both contribute to the observed lower carrier concentration.

The TDH data fitting suggest that there is a high degree of compensation in the films, ranging between 0.4-0.55 (N_d/N_a). However, the shallow acceptor level found in the implanted samples imply that there is more acceptors than compensating defects. If there were and excess of compensating defect the introduced shallow energy level would be the first to be occupied and should therefore not be detectable. Further, Li *et al.* [59] report on considerable numbers of nitrogen interstitials (N_i) in N doped Cu_2O accompanied by nitrogen substitution (N_O) and oxygen vacancies(V_O). With annealing the concentration of N_i is expected to decrease at the expense of N_O formation. Ideally all the nitrogen should contribute a hole to the carrier density (eq. 2.22), however charge neutrality might also be maintained through the likes of oxygen vacancies;

$$3O_O^x \xrightarrow{N} 2N_O^{/} + V_O^{\bullet\bullet} + \frac{3}{2}O_2 \tag{4.1}$$

$$O_O^x = V_O^{\bullet\bullet} + 2e^{/} + \frac{1}{2}O_2 \tag{4.2}$$

where V_O could act as a self-compensating deep trap reducing the hole concentration in the samples. If there is formation of oxygen vacancies this would act as a compensator, effectively reducing the free carrier concentration in the sample.

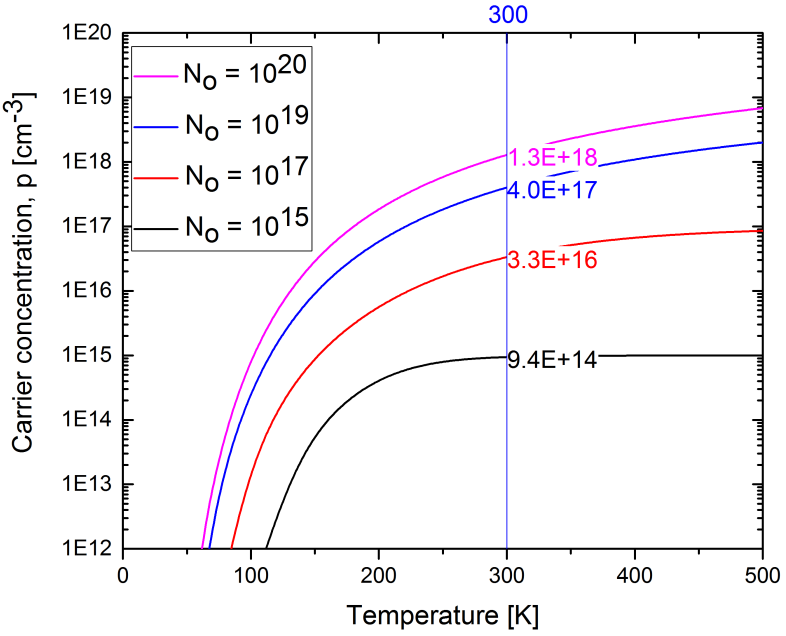

Figure 4.23: Numerical solution showing the degree of ionization of N_O in Cu_2O versus temperature. The calculations are done for four chemical doping concentrations, 10^{15}, 10^{17}, 10^{19} and $10^{20}cm^{-3}$, with an activation energy $E_a = 170meV$.

The presence of N_i in the samples before annealing agrees well with the carrier density data in this work. An increased carrier density is observed after annealing where N_O probably is more readily formed. In addition, the effect of passivation of N_O by other impurities/defects cannot be excluded as well as the possibility of N forming electrically inactive clusters.

5 | Conclusion

In this work, the effect of oxygen partial pressure during Cu_2O sputter deposition has been investigated together with the effect of post-deposition annealing by RTA. Moreover, the effect of nitrogen doping by ion implantation followed by post-implantation annealing for electrical activation has been studied.

The phase transition from $Cu \rightarrow Cu_2O \rightarrow CuO$ is demonstrated with increasing oxygen partial pressure during deposition. Phase pure Cu_2O films were achieved in an intermediate region allowing for deposition of films with high mobility and transmittance. It was concluded that a close control of the oxygen pressure during deposition is essential for optimal growth conditions, resulting in superior films concerning optical, structural and electrical properties.

The effect of RTA post-deposition annealing at $900\,^{\circ}\mathrm{C}$ was further confirmed to have a strong effect on the structural properties of the Cu_2O thin film, leading to enhanced grain size and improved hole mobility in the Cu_2O films in addition to reduced carrier concentrations.

Nitrogen doping was successfully implemented through ion implantation, and post-implantation annealing was carried out for optimum electrical activation of the nitrogen atoms. Temperatures above $400\,^{\circ}\mathrm{C}$ (0.5h) had a strong effect on the resulting carrier concentrations, clearly indicating an increased incorporation of nitrogen as N_O. Prolonged annealing was required in the samples which were RTA treated prior to implantation, where increased carrier concentration first were attained after 4 hours at $400\,^{\circ}\mathrm{C}$. A shallow acceptor level was deduced about $\sim 170meV$ above E_v in the implanted samples but not in the undoped ones. This level is ascribed to the successful incorporation of N_O in the samples. Thereby, it effectively contributes to the carrier (hole) concentration and reduces the resistivity of the films. The reduction in resistivity from nitrogen doping is promising for the realization of low-resistivity ohmic contacts on Cu_2O thin films for solar cell applications.

Suggestion for Further Work

A mroe extensive concentration series which adresses the effect of increased nitrogen concentrations would provide further insight into the nature of nitrogen incorporation in the Cu_2O films. Additionally, contact resistivity of metals on nitrogen ion implanted Cu_2O thin films should be investigated to fully confirm that doping by nitrogen implantation is a viable technique to achieve low-resistivity contacts. Further, the thickness of the implanted layer could be optimized for this purpose. Finally, the implementation of such a layer in a solar cell structure should be performed with the demonstration of reduced series resistance and thus an increased fill factor for the solar cell.

To further confirm that the shallow acceptor level of 170 meV above E_v is indeed due to nitrogen and not implantation-induced defects, the implantation of an inert species should be employed. This would rule out that the increased carrier concentration is merely a consequence of the increased defect formation from the implantation.

Finally, photoluminescence (PL) and X-Ray photon spectroscopy (XPS) of the films would contribute information of the defects in the films and how they change with implantation and successive annealing treatments.

Bibliography

[1] Akos Stiller/Bloomberg. Photovoltaic solar panels sit in an array at the 16-megawatt visonta solar power station operated by matrai eromu zrt, as the coal power station stands beyond, in visonta, hungary, on wednesday, july 27, 2016. URL https://assets.bwbx.io/images/users/iqjWHBFdfxIU/iwwM.{_}Qj0A4c/v0/1600x-1.jpg, 2017. (accessed: 21.04.2017).

[2] Dhiraj Singh/Bloomberg. Solar power geysers to heat hot water sit on the roofs of a residential shack in the alexandra township outside johannesburg, south africa, on thursday, oct. 6, 2016. URL https://assets.bwbx.io/images/users/iqjWHBFdfxIU/iMM0{_}KX5vUDg/v0/1600x-1.jpg, 2017. (accessed: 20.04.2017).

[3] Russ Underwood/Lockheed Martin Space Systems. International space station solar array blanket - a solar array blanket for the international space station (iss) is seen here fully deployed at lockheed martin space systems company of sunnyvale, calif. two blankets comprise each solar array wing. URL http://www.spacedaily.com/images/lm-iss-solar-array-blanket-bg.jpg, 2017. (accessed: 20.04.2017).

[4] Ohsumi Tomohiro/Bloomberg. Solar panels on the roof of toyota motor corp.'s new prius plug-in hybrid vehicles, at the national museum of emerging science & innovation in tokyo on wednesday, feb. 15, 2017. URL https://assets.bwbx.io/images/users/iqjWHBFdfxIU/i7iR4GYzw5XY/v0/1600x-1.jpg, 2017. (accessed: 20.04.2017).

[5] Frankfurt School for Climate and Sustainable Energy Finance and Bloomberg New Energy Finance. Global Trends in Renewable Energy. Technical report, Frankfurt School - UNEP Collaborating Centre for Climate & Sustainable Energy Finance, Frankfurt, 2017.

[6] Vera Steinmann, Riley E Brandt, and Tonio Buonassisi. Photovoltaics: Non-cubic solar cell materials. *Nat Photon*, 9(6):355–357, jun 2015. ISSN 1749-4885.

[7] Karl Philipp Hering. *Copper oxide material and device optimization for photovoltaics*. PhD thesis, Justus-Liebig-Universität, Otto-Behaghel-Str. 8, 35394 Gießbetaen, 2016.

[8] Meidan Ye, Xiaodan Hong, Fayin Zhang, and Xiangyang Liu. Recent advancements in perovskite solar cells: flexibility, stability and large scale. *J. Mater. Chem. A*, 4:6755–6771, 2016. doi:10.1039/C5TA09661H.

[9] Alberto Mittiga, Enrico Salza, Francesca Sarto, Mario Tucci, and Rajaraman Vasanthi. Heterojunction solar cell with 2% efficiency based on a cu2o substrate. *Applied Physics Letters*, 88(16):163502, 2006. doi:10.1063/1.2194315.

[10] K. Bergum, H. N. Riise, S. M. Gorantla, E. Monakhov, and B. G. Svensson. Thin film cu2o for solar cell applications. In *2016 IEEE 43rd Photovoltaic Specialists Conference (PVSC)*, pages 2770–2773, June 2016. doi:10.1109/PVSC.2016.7750156.

[11] Tadatsugu Minami, Yuki Nishi, and Toshihiro Miyata. Efficiency enhancement using a zn 1-x ge x -o thin film as an n-type window layer in cu2o-based heterojunction solar cells. *Applied Physics Express*, 9(5):052301, 2016.

[12] Kazuya Fujimoto, Takeo Oku, and Tsuyoshi Akiyama. Fabrication and characterization of zno/cu2o solar cells prepared by electrodeposition. *Applied Physics Express*, 6(8):086503, 2013.

[13] Sin Cheng Siah, Yun Seog Lee, Yaron Segal, and Tonio Buonassisi. Low contact resistivity of metals on nitrogen-doped cuprous oxide (Cu2O) thin-films. *Journal of Applied Physics*, 112 (8), 2012. ISSN 00218979. doi:10.1063/1.4758305.

[14] Guozhong Lai, Yangwei Wu, Limei Lin, Yan Qu, and Fachun Lai. Low resistivity of N-doped Cu2O thin films deposited by rf-magnetron sputtering. *Applied Surface Science*, 285(Part B): 755–758, 2013. ISSN 01694332. doi:10.1016/j.apsusc.2013.08.122.

[15] Yun Seog Lee, Jaeyeong Heo, Mark T. Winkler, Sin Cheng Siah, Sang Bok Kim, Roy G. Gordon, and Tonio Buonassisi. Nitrogen-doped cuprous oxide as a p-type hole-transporting layer in thin-film solar cells. *Journal of Materials Chemistry A*, 1(48):15416, 2013. ISSN 2050-7488. doi:10.1039/c3ta13208k.

[16] Charles Kittel. Introduction to solid state physics. *Solid State Physics*, page 703, 2005. ISSN 1079-7114.

[17] Ben G Streetman and Sanjay Banerjee. *Solid state electronic devices*. Prentice Hall series in solid state physical electronics. Pearson/Prentice-Hall, Upper Saddle River, N.J, 6th ed. edition, 2006. ISBN 013149726X.

[18] Richard J. D. Tilley. *Understanding Solids*. John Wiley & Sons, Ltd, 2005. ISBN 9780470020845. doi:10.1002/0470020849.ch5.

[19] Truls Norby and Per Kofstad. *Defects and Transport in Crystalline Materials*. University of Oslo, 2016.

[20] S.A. Campbell. *Fabrication Engineering at the Micro- and Nanoscale*. Oxford series in electrical and computer engineering. Oxford University Press, 2013. ISBN 9780199861224.

[21] Francesco Biccari. Defects and Doping in Cu2O, 2009. ISSN 0031-9015.

[22] J. Nelson. *The Physics of Solar Cells*. Series on Properties of Semiconductor Materials. Imperial College Press, 2003. ISBN 9781860943492.

[23] Kunta Yoshikawa, Hayato Kawasaki, Wataru Yoshida, Toru Irie, Katsunori Konishi, Kunihiro Nakano, Toshihiko Uto, Daisuke Adachi, Masanori Kanematsu, Hisashi Uzu, and Kenji Yamamoto. Silicon heterojunction solar cell with interdigitated back contacts for a photoconversion efficiency over 26%. *Nature Energy*, 2:17032, mar 2017.

[24] Simom Philipps, Warmuth, and Werner. Photovoltaics Reports. Technical report, Fraunhofer ISE, 2016.

[25] A De Vos. Detailed balance limit of the efficiency of tandem solar cells. *Journal of Physics D: Applied Physics*, 13(5):839, 1980.

[26] Scopus. URL `http://scopus.com`. (accessed: 10.03.2017).

[27] B. K. Meyer, A. Polity, D. Reppin, M. Becker, P. Hering, P. J. Klar, Th. Sander, C. Reindl, J. Benz, M. Eickhoff, C. Heiliger, M. Heinemann, J. Bläsing, A. Krost, S. Shokovets, C. Müller, and C. Ronning. Binary copper oxide semiconductors: From materials towards devices. *Physica Status Solidi (B)*, 249(8):1487–1509, 2012. ISSN 1521-3951. doi:10.1002/pssb.201248128.

[28] L. O. Grondahl. The copper-cuprous-oxide rectifier and photoelectric cell. *Rev. Mod. Phys.*, 5:141–168, Apr 1933. doi:10.1103/RevModPhys.5.141.

[29] Michael Riordan, Lillian Hoddeson, and Conyers Herring. The invention of the transistor. *Rev. Mod. Phys.*, 71:S336–S345, Mar 1999. doi:10.1103/RevModPhys.71.S336.

[30] L. C. Olsen, R. C. Bohara, and M. W. Urie. Explanation for low-efficiency cu2o schottky-barrier solar cells. *Applied Physics Letters*, 34(1):47–49, 1979. doi:10.1063/1.90593.

[31] Koichi Momma and Fujio Izumi. Vesta3 for three-dimensional visualization of crystal, volumetric and morphology data. *Journal of Applied Crystallography*, 44(6):1272–1276, 2011. doi:10.1107/S0021889811038970.

[32] Bruno K. Meyer, Angelika Polity, Daniel Reppin, Martin Becker, Philipp Hering, Benedikt Kramm, Peter J. Klar, Thomas Sander, Christian Reindl, Christian Heiliger, Markus Heinemann, Christian Müller, and Carsten Ronning. Chapter Six - The Physics of Copper Oxide (Cu2O). In *Semiconductors and Semimetals*, volume 88, pages 201–226. 2013. ISBN 9780123964892. doi:10.1016/B978-0-12-396489-2.00006-0.

[33] Walter H. Brattain. The copper oxide rectifier. *Rev. Mod. Phys.*, 23:203–212, Jul 1951. doi:10.1103/RevModPhys.23.203.

[34] Tadatsugu Minami, Yuki Nishi, and Toshihiro Miyata. Impact of incorporating sodium into polycrystalline p-type cu2o for heterojunction solar cell applications. *Applied Physics Letters*, 105(21):212104, 2014. doi:10.1063/1.4902879.

[35] Yun Seog Lee, Danny Chua, Riley E. Brandt, Sin Cheng Siah, Jian V. Li, Jonathan P. Mailoa, Sang Woon Lee, Roy G. Gordon, and Tonio Buonassisi. Atomic layer deposited gallium oxide buffer layer enables 1.2 v open-circuit voltage in cuprous oxide solar cells. *Advanced Materials*, 26(27):4704–4710, 2014. ISSN 1521-4095. doi:10.1002/adma.201401054.

[36] K. Bergum, H. N. Riise, S. M. Gorantla, E. Monakhov, and B. G. Svensson. Thin film cu2o for solar cell applications. In *2016 IEEE 43rd Photovoltaic Specialists Conference (PVSC)*, pages 2770–2773, June 2016. doi:10.1109/PVSC.2016.7750156.

[37] Tadatsugu Minami, Yuki Nishi, and Toshihiro Miyata. Cu2o-based solar cells using oxide semiconductors. *Journal of Semiconductors*, 37(1):014002, 2016.

[38] T. Tiedje, E. Yablonovitch, G. D. Cody, and B. G. Brooks. Limiting efficiency of silicon solar cells. *IEEE Transactions on Electron Devices*, 31(5):711–716, May 1984. ISSN 0018-9383. doi:10.1109/T-ED.1984.21594.

[39] Ørnulf Nordseth, Raj Kumar, Kristin Bergum, Laurentiu Fara, Sean Erik Foss, Halvard Haug, Florin Dragan, Dan Craciunescu, Paul Sterian, Irinela Chilibon, Cristina Vasiliu, Laurentiu Baschir, Dan Savastru, Edouard Monakhov, and Bengt Gunnar Svensson. Optical Analysis of a ZnO/Cu2O Subcell in a Silicon-Based Tandem Heterojunction Solar Cell. *Green and Sustainable Chemistry*, 07(01):57–69, 2017. ISSN 2160-6951. doi:10.4236/gsc.2017.71005.

[40] Shogo Ishizuka, Shinya Kato, Takahiro Maruyama, and Katsuhiro Akimoto. Nitrogen doping into cu2o thin films deposited by reactive radio-frequency magnetron sputtering. *Japanese Journal of Applied Physics*, 40(4S):2765. doi:10.1143/JJAP.40.2765.

[41] P.M. Sberna, I. Crupi, F. Moscatelli, V. Privitera, F. Simone, and M. Miritello. Sputtered cuprous oxide thin films and nitrogen doping by ion implantation. *Thin Solid Films*, 600: 71–75, 2016. ISSN 00406090. doi:10.1016/j.tsf.2016.01.005.

[42] Hartmut Frey and Hamid R Khan. *Handbook of Thin Film Technology*. ISBN 978-3-527-31052-4. doi:10.1007/978-3-642-05430-3.

[43] Michael Nastasi and James Mayer. *Semiconductor Material and Device Characterization*. Springer Berlin Heidelberg, Berlin, 2006. ISBN 0471739065. doi:10.1007/978-3-540-45298-0.

[44] James F. Ziegler, M.D. Ziegler, and J.P. Biersack. Srim - the stopping and range of ions in matter (2010). *Nuclear Instruments and Methods in Physics Research Section B: Beam Interactions with Materials and Atoms*, 268(11-12):1818 – 1823, 2010. ISSN 0168-583X. doi:10.1016/j.nimb.2010.02.091. 19th International Conference on Ion Beam Analysis.

[45] M. Birkholz. *Thin Film Analysis by X-Ray Scattering*. Springer Berlin Heidelberg, 2006. ISBN 3642054293.

[46] Yang Leng. *X-Ray Diffraction Methods*, pages 47–82. Wiley-VCH Verlag GmbH and Co. KGaA, 2013. ISBN 9783527670772. doi:10.1002/9783527670772.ch2.

[47] F. M. Smits. Measurement of sheet resistivities with the four-point probe. *Bell System Technical Journal*, 37(3):711–718, 1958. ISSN 1538-7305. doi:10.1002/j.1538-7305.1958.tb03883.x.

[48] L. B. Valdes. Resistivity measurements on germanium for transistors. *Proceedings of the IRE*, 42(2):420–427, Feb 1954. ISSN 0096-8390. doi:10.1109/JRPROC.1954.274680.

[49] L. J. Van der Pauw. A method of measuring specific resistivity and hall effect of discs of arbitrary shape. *Philips Reasearch Reports*, 13(1):1–9, Feb 1958.

[50] P. Blood and J.W. Orton. *The electrical characterization of semiconductors: majority carriers and electron states*. Number v. 2 in Techniques of physics. Academic Press, 1992. ISBN 9780125286275.

[51] Shimadzu. URL `http://www.shimadzu.com/an/uv/support/fundamentals/structure.html#2`. (accessed: 20.04.2017).

[52] Dieter K. Schroder. *Semiconductor Material and Device Characterization*. Wiley, Hoboken, third edit edition, 2006. ISBN 0471739065. doi:10.1002/0471749095.

[53] J. Gan, V. Venkatachalapathy, B.G. Svensson, and E.V. Monakhov. Influence of target power on properties of cuxo thin films prepared by reactive radio frequency magnetron sputtering. *Thin Solid Films*, 594, Part B:250 – 255, 2015. ISSN 0040-6090. doi:10.1016/j.tsf.2015.05.029. Transparent Conductive Materials, {TCM} Series (2014).

[54] Yang Leng. *Secondary Ion Mass Spectrometry for Surface Analysis*, pages 253–282. Wiley-VCH Verlag GmbH and Co. KGaA, 2013. ISBN 9783527670772. doi:10.1002/9783527670772.ch8.

[55] Per F. Lindberg, Martin Nyborg, Bengt G. Svensson, Edouard V. Monakhov, and Augustinas Galeckas. Controlling morphology and electronic properties of cu2o films, prepared by dc sputter deposition, by regulating o2 flow. *Manuscript in preparation.*, 2017.

[56] Yoshitaka Nakano, Shu Saeki, and Takeshi Morikawa. Optical bandgap widening of p-type Cu2O films by nitrogen doping. *Applied Physics Letters*, 94(2):2007–2010, 2009. ISSN 00036951. doi:10.1063/1.3072804.

[57] A.E. Rakhshani. Preparation, characteristics and photovoltaic properties of cuprous oxide - a review. *Solid-State Electronics*, 29(1):7 – 17, 1986. ISSN 038-1101. doi:10.1016/0038-1101(86)90191-7.

[58] Yu Sup Jung, Hyung Wook Choi, and Kyung Hwan Kim. Properties of p-type N-doped Cu2O thin films prepared by reactive sputtering. *Japanese Journal of Applied Physics*, 53:11RA10, 2014. doi:10.7567/JJAP.53.11RA10.

[59] Junqiang Li, Zengxia Mei, Lishu Liu, Huili Liang, Alexander Azarov, Andrej Kuznetsov, Yaoping Liu, Ailing Ji, Qingbo Meng, and Xiaolong Du. Probing Defects in Nitrogen-Doped Cu2O. *Scientific Reports*, 4, NOV 28 2014. ISSN 2045-2322. doi:10.1038/srep07240.

[60] Kristin Bergum, Heine N. Risse, Sandeep Gorantla, Per F. Lindberg, Anette E. GunnÃęs, Spyros Diplas, Bengt G. Svensson, and Edouard Monakhov. Improving carrier transport in cu2o thin films by rapid thermal annealing. *Manuscript in preparation.*, 2017.

[61] Yun Seog Lee, Mark T. Winkler, Sin Cheng Siah, Riley Brandt, and Tonio Buonassisi. Hall mobility of cuprous oxide thin films deposited by reactive direct-current magnetron sputtering. *Applied Physics Letters*, 98(19):192115, 2011. doi:10.1063/1.3589810.

[62] Sanggil Han, Kham M. Niang, Girish Rughoobur, and Andrew J. Flewitt. Effects of post-deposition vacuum annealing on film characteristics of p-type Cu2O and its impact on thin film transistor characteristics. *Applied Physics Letters*, 109(17), OCT 24 2016. ISSN 0003-6951. doi:10.1063/1.4965848.

Appendix A

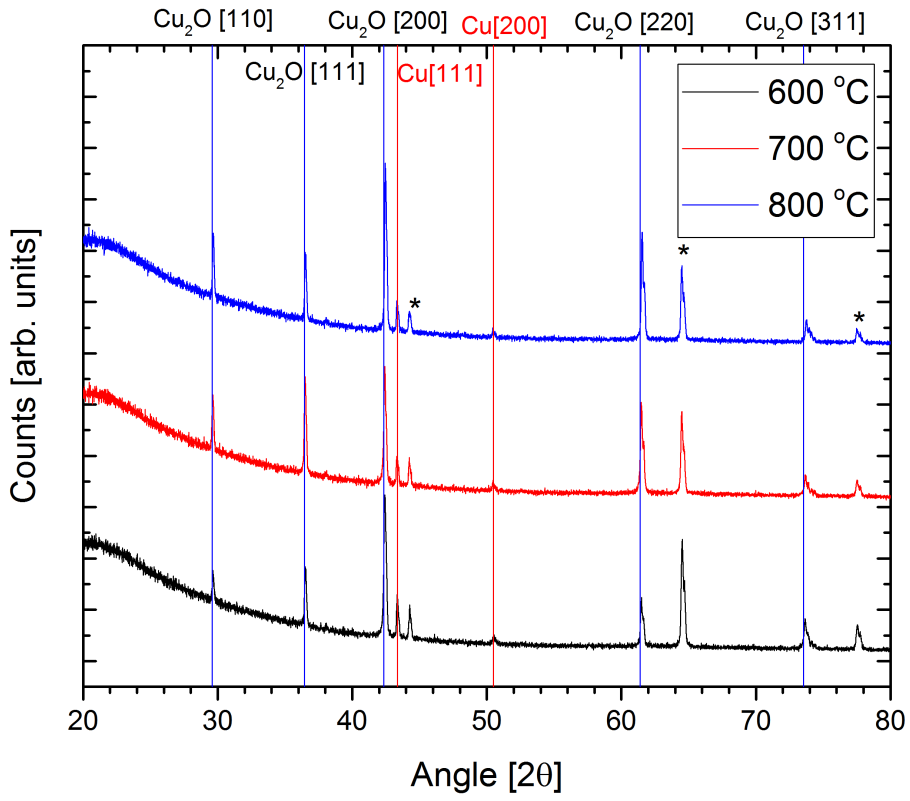

Figure 5.1: XRD results for Cu_2O annealed in the RTA system at $600, 700$ and $800\,^{\circ}\mathrm{C}$ with a base pressure of $10^{-3}Torr$.

Appendix B

XRD

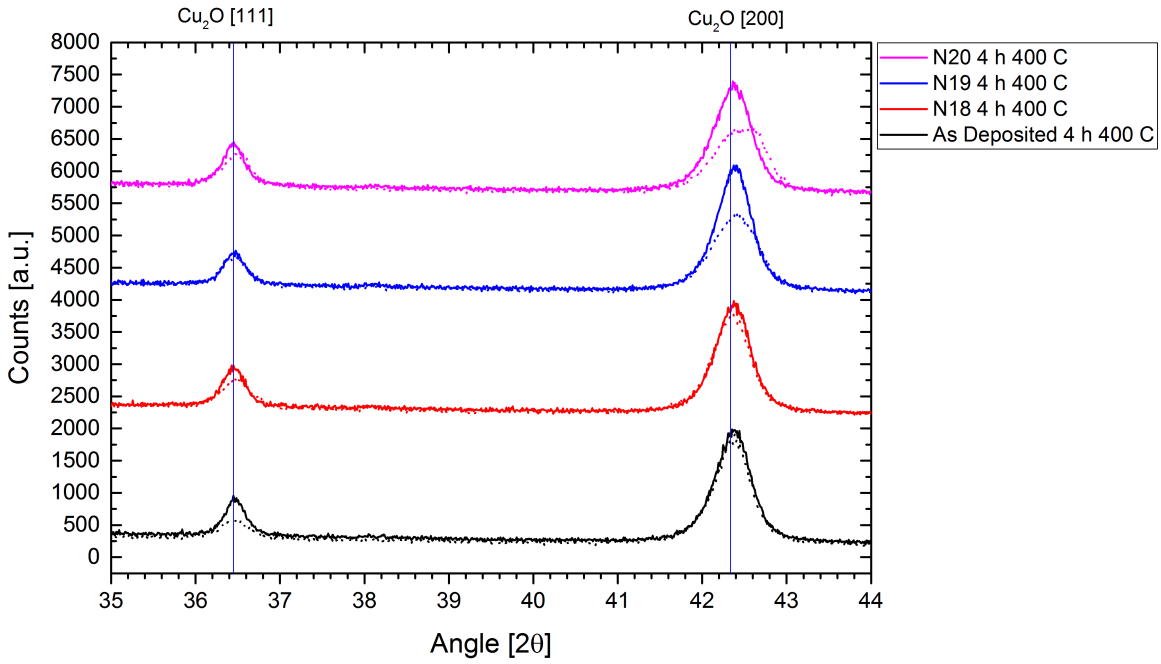

Figure 5.2: XRD results for $Cu_2O : N$ films with different implantation concentrations. The solid lines are after annealing at $400\,^{\circ}\mathrm{C}$ for 4 hours while the dotted line are as implanted.

Hall Effect Measurement Results

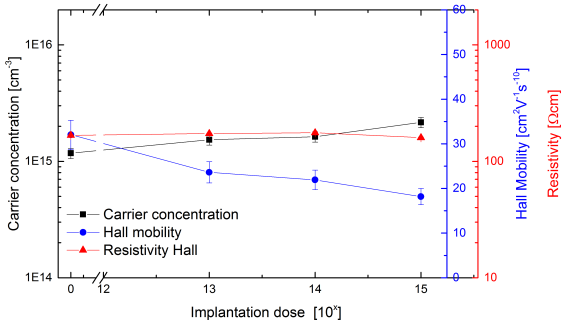

(a) As implanted

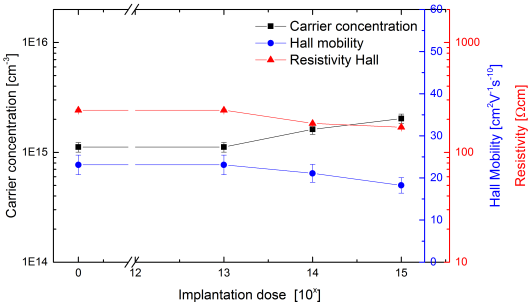

(b) After annealing at 400 °C for 4 hours.

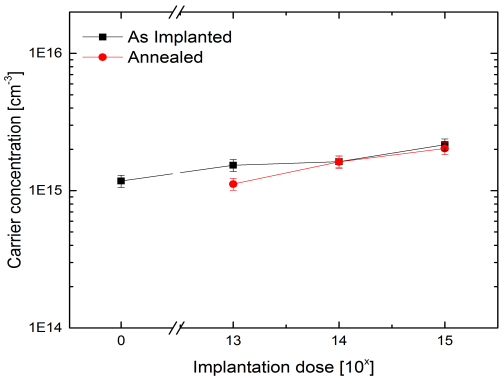

(c) Comparisson of carrier concentration for the as implanted and annealed samples for the expected nitrogen concentrations.

Figure 5.3: Resisitivity measured with both Four-point probe and Hall Effect, carrier concentration and Hall mobility plotted as a function of expected nitrogen concentration.

Transmission Results

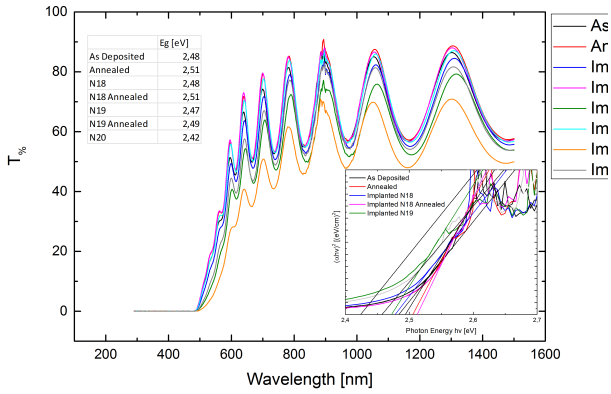

(a) Transmission measurements and tauc plot for samples doped with different concentrations of nitrogen.

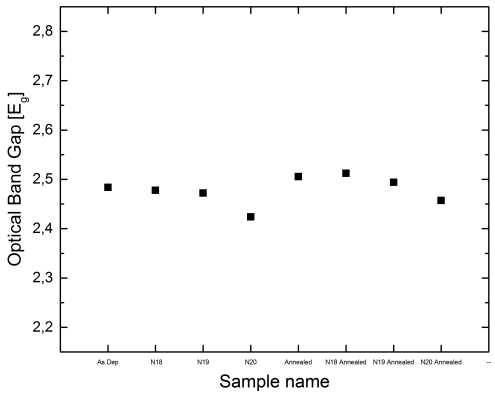

(b) optical Eg

SIMS Results

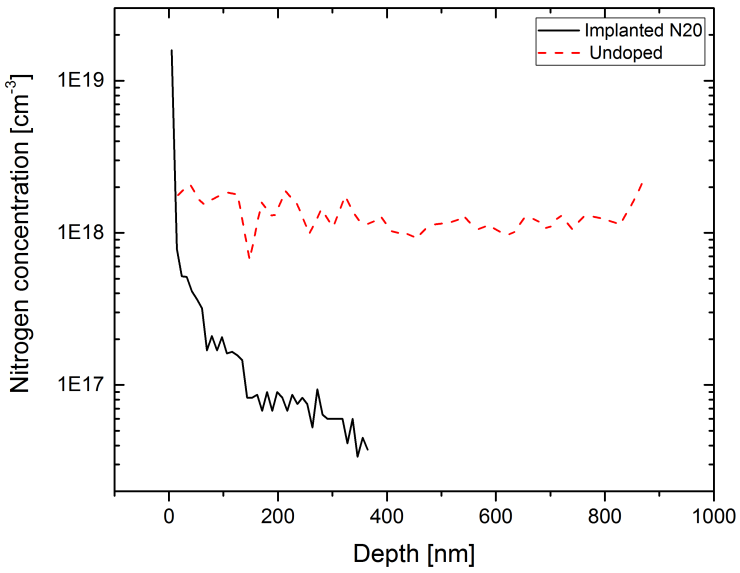

Figure 5.5: SIMS results for $Cu_2O : N$ films ($N \simeq 10^{20} cm^{-3}$) made for the concentration series.

Appendix C

Table 5.1: Resistivity measured by four point probe of nitrogen implanted samples ($N \sim 10^{20} cm^{-3}$) after various annealing conditions. RTA is done prior to implantation on the samples labeled RTA.

	Resisitivty $[\Omega cm]$
RTA - 400 °C 4 H	28 ± 1
RTA - 400 °C 16 H	96 ± 2
RTA - 500 °C 2H	33 ± 1
400 °C 4 H	80 ± 1
400 °C 16 H	148 ± 6
500 °C 2H	99 ± 1